DISS. ETH NO. 24712

Variational Approach to Lagrangian Coherent Structures in Three-Dimensional Unsteady Flows

A thesis submitted to attain the degree of

DOCTOR OF SCIENCES of ETH ZURICH

(Dr. sc. ETH Zurich)

presented by

David Öttinger

MSc ETH Physics

born on 02.05.1989
citizen of
Germany

accepted on the recommendation of
Prof. Dr. George Haller
Prof. Dr. Markus Holzner

2017

Abstract

Unsteady fluid flows, as seen e.g., in the ocean or atmosphere, are mostly turbulent and evolve on numerous time and length scales. Despite these complexities, they produce striking tracer patterns that coherently move with the flow. Well-known examples are tornadoes, fronts due to thunderstorms, or Jupier's bands.

As a mathematical representation of these phenomena, Lagrangian coherent structures (LCSs) define material surfaces that satisfy exceptional deformation properties. Three types of LCSs are known: elliptic, hyperbolic and parabolic LCSs, capturing coherent vortices, fronts and jets.

Recently developed theories of LCSs introduce variational principles whose solutions explicitly parametrize LCSs. Most of these works refer to two-dimensional flows and obtain LCSs as material curves. LCSs in three dimensions are surfaces, however, and demand different theoretical and numerical approaches.

Here, we develop a new variational theory of elliptic LCSs. Secondly, we show that, in three dimensions, there is a single differential equation capturing all types of LCSs. This result is surprising, because no such unification exists in the simpler two-dimensional case. We develop numerical procedures and algorithms to demonstrate our findings on examples.

Finally, we investigate the dynamics of small spherical particles in flows through branching junctions. Recent experiments have observed that, unexpectedly, particles can get trapped near the crossing of the pipes. Using simulations, we discover a new type of coherent structure that explains how particles become captured in these flows.

Zusammenfassung

Instationäre Strömungen, wie sie z.B. in den Ozeanen oder in der Atmosphäre auftreten, sind normalerweise turbulent und entwickeln sich auf mehreren Zeit- und Längenskalen. Trotz dieser Komplexität bilden sich in diesen Strömungen sehr auffallende Muster von Tracerpartikeln, die sich kohärent im Fluid mitbewegen. Bekannte Beispiele sind Tornados, Gewitterfronten, oder die Bänder des Jupiters.

Um diese Phänomene mathematisch zu beschreiben, definieren Lagrange'sche kohärente Strukturen (LCSs, für engl. *Lagrangian coherent structures*) materielle Flächen mit besonderen Deformationseigenschaften. Drei Arten von LCSs sind bekannt: elliptische, hyperbolische und parabolische LCSs, zur Erfassung von kohärenten Wirbeln, Fronten und Jets.

Aktuelle Arbeiten über LCSs führen Variationsprinzipien ein, deren Lösungen die LCSs explizit parametrisieren. Die meisten dieser Theorien beziehen sich auf zweidimensionale Strömungen, in denen LCSs materielle Kurven sind. LCSs in drei Dimensionen sind jedoch Flächen, und erfordern andere theoretische und numerische Herangehensweisen.

In dieser Arbeit entwickeln wir eine neue Variationstheorie für elliptische LCSs. Ausserdem zeigen wir, dass es in drei Dimensionen eine einzelne Differentialgleichung für alle LCS-Typen gibt. Dieses Ergebnis ist überraschend, da im einfacheren zweidimensionalen Fall keine solche Vereinheitlichung existiert. Wir entwickeln numerische Methoden, um unsere Ergebnisse an Beispielen zu demonstrieren.

Abschliessend untersuchen wir die Dynamik kleiner, sphärischer Partikel in Strömungen durch Rohrverzweigungen. Neue Experimente hatten überraschend gezeigt, dass Teilchen durch die Strömung nahe der Verzweigung festgehalten werden können. Mithilfe von Simulationen entdecken wir eine neue Art von kohärenter Struktur, die erklärt, wie Teilchen in solchen Strömungen gefangen werden.

Acknowledgements

First and foremost, I would like to thank my advisor Prof. George Haller for his continuous support, encouragement and guidance. His clear approach to applied mathematics has been very inspiring, and I have benefited from his experience in many ways that go beyond just research. Thanks to him, I have been in a great environment for four years now, a time filled with many memorable experiences.

I am grateful to Prof. Markus Holzner for kindly agreeing to co-examine my thesis.

I would like to thank Daniel Blazevski, and especially Jesse Ault and Prof. Howard Stone for very interesting collaborations.

It has been a great pleasure to be a part of our research group, who always guaranteed for a good atmosphere and interesting conversations. This has influenced me a lot over time. Thank you all, Alireza Hadjighasem, Arjun Sharma, Beate Fonfé, Daniel Karrasch, Florian Huhn, Florian Kogelbauer, Gabriel Provencher-Langlois, Mattia Serra, Mohammad Farazmand, Paolo Tiso, Sándor Szanyi, Sophie Calabretto, Shobhit Jain, Sten Ponsioen, Thomas Breunung and Zsolt Verasztó.

Finally, I am grateful to my family: to my uncle Hans Christian Öttinger for his advice, and to my parents for pretty much everything.

Contents

Chapter 1

Introduction

1.1 Introduction

Fluid flows are notorious for their complexity in space and time. Be it the sudden shocks we suffer on an airplane caught in turbulence, or the famous *butterfly effect*—it is easy to get the impression that fluids behave randomly. Yet, some of the most turbulent flows produce seemingly simple organized motion: tornadoes in our atmosphere, or the Great Red Spot on Jupiter (Fig. 1.1). Such visually striking phenomena inspire scientists to mathematically seek *coherent structures* underlying these patterns and, hence, contribute to a simplified understanding of fluid dynamics (cf., e.g., [58, 41]).

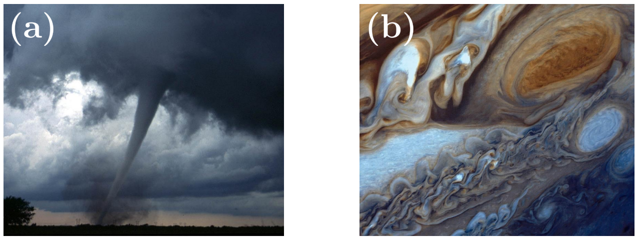

Fig. 1.1: Coherent phenomena in atmospheric flows: **(a)** Tornado near Anadarko, Oklahoma [4], **(b)** Great Red Spot on Jupiter [3].

The traditional approach to fluid mechanics is from an *Eulerian* viewpoint, i.e., based on instantaneous, laboratory-frame quantities such as pressure or the fluid velocity field. While this is advantageous in many problems, explaining material transport and the formation of tracer patterns requires knowledge of the paths of fluid parcels. In general, however, these trajectories are not immediately linked to the Eulerian quantities. Accordingly, assuming the frame of individual fluid parcels is called the *Lagrangian* view of fluid mechanics.

With today's technology, it is tempting to either track a large number of particles in experiments, or to integrate vast amounts of trajectories from simulation data. Such approaches, however, typically produce an incomprehensible mess of curves (Fig. 1.2). In complicated time-dependent problems, it becomes impossible to discern structures from such visualizations. Moreover, individual trajectories are often sensitive to small changes of the initial conditions and small variations of the system parameters. This limits their use for parameter studies and the robust detection of flow features.

Fig. 1.2: A long-exposure photography of a campfire reveals the trajectories of sparks [1].

Dynamical systems theory (cf., e.g., [27]) provides a framework for analyzing large collections of fluid trajectories: e.g., invariant manifolds separate dynamically distinct regions in the flow [74]; or Poincaré maps reveal the delicate structure of invariant tori in vortex rings [73]. Such classic concepts, however, only apply to steady or time-periodic systems defined over an infinite time interval. While these are good assumptions for certain laboratory flows, in most applications, the setting is an ordinary differential equation

$$\dot{\boldsymbol{x}} = \boldsymbol{u}(\boldsymbol{x}, t), \quad \boldsymbol{x} \in D, \quad t \in [t_0, t_1], \tag{1.1}$$

where $\boldsymbol{x}$ is a particle position in a two- or three-dimensional domain D; $[t_0, t_1]$ is a finite time interval. In (1.1), the velocity field $\boldsymbol{u}$ is given, e.g., from observations of geophysical flows or direct numerical simulations of the Navier-Stokes equations, and may have an arbitrary time dependence.

The generality of the setting (1.1) has motivated analyses of fluid flows using mathematical techniques that are not obviously related to fluid mechanics. Despite their intricacy, these approaches can involve critical steps or assumptions: E.g., techniques related to the Koopman operator [10] require ergodicity [5]; use of the Perron-Frobenius operator [25] or spectral clustering [32] leads to the problem of thresholding spectral gaps [72, 30]; braids [78] are restricted to two dimensions. In addition, several of the available methods highlight flow structures whose physical meaning is difficult to assess [30]. An advantage of certain more general mathematical approaches (e.g., [10, 25, 32, 78]) is that they can operate already on sparse trajectory data and, hence, do not require complete availability of the velocity field $\boldsymbol{u}$.

Among the more physics-oriented approaches, numerous methods (c.f., e.g. [30]) provide scalar fields that have a direct interpretation and give a quick global overview of the flow (cf. Fig. 1.3). Extracting definite, parametrized structures from such fields, however, requires numerical post-processing [38, 47]. Moreover, the apparent simplicity of some approaches leaves room for misconceptions: Several traditional vortex criteria, such as the Q criterion [43], are not materially *objective* [34, 29]. Non-objective criteria identify structures relative to a given reference frame, but a simple rotational motion of the observer changes their assessments. Another example is the finite-time Lyapunov exponent (FTLE) field [69]: even though sometimes originating from high shear [33], high FTLE values have been wrongly used for locating repelling and attracting coherent structures [35].

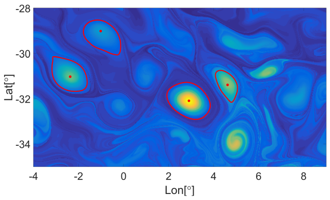

Fig. 1.3: The Lagrangian-averaged vorticity deviation [38] reveals mesoscale ocean eddies, with the highlighted contour lines (*red curves*) representing coherent vortex boundaries [2].

Theories of *Lagrangian coherent structures* (LCSs) [41, 36] directly define transport barriers in unsteady, finite-time flows (1.1). LCSs are material surfaces with exceptional impact on tracer patterns. Their counterparts in classic dynamical systems theory are codimension-one invariant manifolds that locally separate the phase space and satisfy specific kinematic properties.

Recent works on LCSs in two dimensions introduce variational principles that identify hyperbolic, elliptic and parabolic LCSs [35, 37, 19]. These three LCS types are exceptional material curves that underly the formation of fronts, coherent material vortices and jets in fluid flows. To facilitate computations, these theories provide explicit expressions for the tangent vectors of initial-time LCS curves. LCSs in two dimensions are thus obtained by solving ordinary differential equations in the initial configuration of the flow.

The existing variational theories of LCSs [35, 37, 19] belong to two categories. Repelling/attracting hyperbolic LCSs [35] are material surfaces that maximize/minimize the Lagrangian normal repulsion. With the repulsion being defined in terms of the flow-map gradient at a point, where the flow map is the mapping that takes initial to final positions under the flow, the theory in [35] is *local*. The *global* variational LCS theories [37, 19], on the other hand, require initial positions of elliptic and parabolic LCSs to be stationary curves of tangential strain and Lagrangian shear functionals.

Recent work on LCSs in three dimensions [9] introduces local variational definitions of hyperbolic LCSs as most/least repelling material surfaces; and of elliptic LCSs as tubular, shear-maximizing material surfaces. The theory provides explicit normal fields for these LCSs. By introducing reference planes in the flow domain and integrating vector fields that are perpendicular to both the LCS normal and the normal of the reference plane, one can thus obtain LCS slices. Combining the slices allows to construct full LCSs as two-dimensional surfaces. There is, however, an additional mathematical condition that must be monitored during this process: For a surface perpendicular to a prescribed normal field to exist, the helicity of the normal field must vanish.

The conditions for constructing local variational LCSs in three dimensions [9] are restrictive and turn out to be hard to implement numerically. In Chapters 2 and 3 of this work, we hence propose alternative methods for obtaining LCSs in three dimensions. In Chapter 4, we investigate the trapping of small, finite-size particles in branching junctions, and discover a new type of transport barrier in three dimensions.

1.2 Summary

Chapter 2 introduces a new theory of elliptic Lagrangian coherent structures in three-dimensional flows with arbitrary time dependence. Building on previous work for two-dimensional flows [37], here, we start by examining a global variational principle for curves that stretch uniformly under the flow. Attempting to build surfaces from such non-filamenting curves, we discover mathematical restrictions on uniformly-stretching surfaces in any three-dimensional flow. We use these constraints to derive general expressions for the normal fields of the most-uniformly stretching material surfaces. These exceptional surfaces define elliptic LCSs that allow us to parametrize coherent material vortices in three-dimensional unsteady flows (Fig. 1.4).

We propose a numerical method to compute such (near-) uniformly stretching LCSs in applications: First, we slice the three-dimensional flow domain into two-dimensional planes. Within each plane, we compute closed curves of specific vector fields to capture segments of unknown LCS surfaces at the initial time. The second step is to assemble smooth tubular surfaces from a possibly large number of closed curves obtained in the first step. To overcome this challenge, we identify a condition that yields the optimal curve to continue the surface construction. Finally, we apply our method to parametrize vortices in steady and time-aperiodic ABC-type flows.

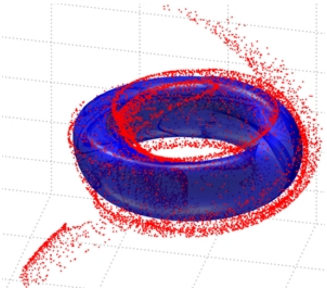

Fig. 1.4: Coherent vortex ring (*blue*) parametrized using the method of Chapter 2. Nearby tracers(*red*) disperse under the flow.

In **Chapter 3**, we review the available definitions of hyperbolic and elliptic LCSs in three-dimensions (cf. [9] and Chapter 2). Despite coming from different variational principles, we observe that the initial-time surfaces for all these LCS types must be tangent to the intermediate eigenvector field of the Cauchy-Green strain tensor. This vector field, hence, defines a dual dynamical system whose two-dimensional invariant manifolds necessarily contain all LCSs in three dimensions. In contrast to the underlying non-autonomous problem, the dual dynamical system is autonomous.

This observation allows us to apply classic concepts for the computation of LCSs: We run long trajectories of the dual dynamical system to detect its two-dimensional invariant manifolds, thus obtaining all LCSs from a single computation (Fig. 1.5). Whereas the procedure of Chapter 2 involves computations on parametric families of two-dimensional vector fields and subsequent reassembly of the data, here, we only require trajectories of a single, three-dimensional dynamical system. We apply our method to a three-dimensional Cat's eye flow, and to steady and time-aperiodic ABC-type flows.

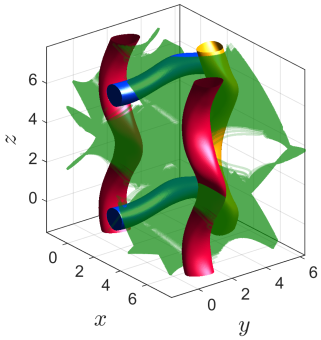

Fig. 1.5: Hyperbolic (*green*) and elliptic LCSs (*red, blue, yellow*) obtained using the dual dynamical system in a time-aperiodic ABC flow (cf. Chapter 3).

In **Chapter 4**, we turn to the more specific setting of inertial particles: These small, finite-size particles show different dynamics than fluids elements, and generally accumulate or disperse within the flow. Starting from the Maxey-Riley equation accounting for the most important fluid-particle interactions [56], it has been shown that such particles approximately follow their own, compressible velocity field [55, 39].

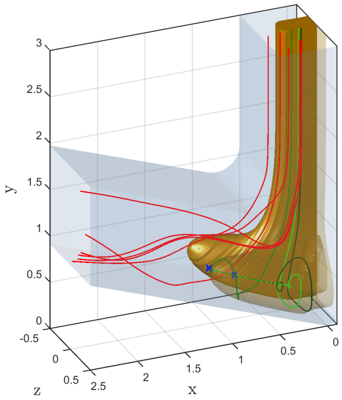

Fig. 1.6: Anchor-shaped trapping region in a V-junction flow (*yellow*) with particle trajectories (*red, green*), cf. Chapter 4.

Using these results, we investigate the recently discovered phenomenon of particle trapping in branching junctions [81]. We discover that the trapping mechanism is due to anchor-type structures that keep particles in the junction (Fig. 1.6). The anchors are invariant manifolds that separate regions of particle trapping from the rest of the flow domain. In contrast to previous notions of LCSs, however, they are not directly visible in patterns created by particle accumulation or passive tracers. Investigating the parameter dependence of the anchor structures, we find that their geometry can undergo transitions, and we identify the parameter domain where particle capture occurs.

Finally, in the mathematical formulation of finite-time systems, we introduce a scalar field, LAQ, measuring the accumulation of particles within the flow. High values of LAQ efficiently visualize either particle clusters or trapping regions. This tool promises to be capable of identifying time-dependent anchor structures in future studies of unsteady particle capture in branching junctions.

Each chapter is based on one research article:

- **Chapter 2**: D. Oettinger, D. Blazevski, and G. Haller. *Global Variational Approach to Elliptic Transport Barriers in Three Dimensions.* Chaos, 26(3):033114, 2016. [64]
- **Chapter 3**: D. Oettinger and G. Haller. *An Autonomous Dynamical System Captures all LCSs in Three-dimensional Unsteady Flows.* Chaos, 26(10), 2016. [65]
- **Chapter 4**: D. Oettinger, J. T. Ault, H. A. Stone, and G. Haller. *Invisible Anchors Trap Particles in Branching Junctions.* preprint, 2017. [63]

Chapter 2

Global Variational Approach to Elliptic Transport Barriers in Three Dimensions

2.1 Introduction

Transport barriers provide a simplified picture of complex time-aperiodic flows as surfaces underlying the formation of tracer patterns [36]. Application areas include fluid dynamics [18], geophysical flows [59, 66] and chemical reactions [49, 62].

An indirect approach to locating transport barriers is to partition the flow into coherent sets [24]. Obtained from a probabilistic transfer operator, coherent sets exhibit minimal leakage among each other. In contrast to the methods that we outline in the following, set-based approaches [24, 10, 32] identify patches and volumes formed by coherent sets of trajectories.

Another, direct approach to transport barriers targets evolving material surfaces with distinguished dynamical behavior. These Lagrangian Coherent Structures (LCSs, see [36] for a review), can be located as explicitly parametrized curves or surfaces using recent variational methods [35, 37, 9, 19]. Three types of LCSs have been introduced in these works: Parabolic LCSs for identifying jet-type structures [19], hyperbolic LCSs as generalized normally hyperbolic invariant manifolds [35], and elliptic LCSs capturing coherent Lagrangian vortices [37]. The latter can be envisioned as sharp material tubes that guide coherent motion of matter over a prolonged interval of time, as often observed, e.g., in tornadoes, steam rings or ocean eddies. In an idealized setting, similar objects exist in steady, incompressible Euler flows [16, 7], in the form of invariant tori or cylinders.

All of the aforementioned variational LCS approaches [35, 37, 19] provide parametrizations of LCS surfaces. These parametrized surfaces are obtained by solving differential equations, as opposed to merely thresholding scalar fields. Moreover, the variational principles underlying the methods in [37, 19] explicitly define the global deformation properties of the surfaces they highlight.

Methods for hyperbolic and elliptic LCSs have recently been extended to three-dimensional flows [9]. These local variational techniques render LCSs as surfaces orthogonal to directions of maximal normal repulsion (hyperbolic LCSs) and maximal tangential shear (elliptic LCSs).

Strictly shear-maximizing elliptic LCSs [9], however, tend to be difficult to locate in real-life data sets, such as the Southern Ocean State Estimate [57]. This is due to the idealized nature of these LCSs, requiring pointwise maximal tangential shear at all points of the surface. This strict maximality requirement may not yield tubular surfaces in complex and noisy data sets.

Here we propose a complementary approach to elliptic LCSs in three-dimensional flows. Our method is an extension of the most recent global variational theory of elliptic LCSs in two-dimensional flows [37], which has already been applied to various numerical velocity fields [37, 31, 82, 42]. The proposed approach replaces the requirement of pointwise maximal tangential shear for elliptic LCSs [9] with the requirement of near-uniform stretching along the LCSs. This allows for small variations in the uniformity of the stretching, thereby yielding numerically more robust elliptic LCS surfaces.

After introducing the mathematical setting, we review the theory of elliptic LCSs in two-dimensional flows from [37]. This approach identifies vortex boundaries as closed material curves that, over a finite time interval, uniformly stretch by a factor λ near unity. By directly extending this variational principle to three dimensions, we find that the generalization of closed and uniformly λ-stretching *curves* to λ-stretching tubular *surfaces* is not straightforward. Our considerations, however, suggest seeking pointwise near-uniformly stretching surfaces. In contrast to the maximal-shear method for elliptic LCSs in three dimensions [9], seeking near-uniformly stretching surfaces yields a parametric family of admissible normal fields for the LCSs. It turns out that, at each point, all near-uniformly stretching surfaces necessarily contain the intermediate eigenvector of the right Cauchy-Green strain tensor. This observation simplifies the construction of elliptic LCSs as tubular near-uniformly stretching surfaces. We finally apply this approach to steady and time-aperiodic ABC-type flows.

2.2 Setup and notation

We consider non-autonomous ordinary differential equations of the form

$$\dot{x} = u(x, \tau), \quad x \in U, \quad \tau \in [t_0, t], \tag{2.1}$$

where the flow domain $U \subset \mathbb{R}^d$ is an open and bounded subset with $d = 2$ or $d = 3$; $[t_0, t]$ is a finite time interval; and the velocity field $u : U \times [t_0, t] \to \mathbb{R}^d$ is assumed to be smooth. In Sec. 2.3, we consider $d = 2$, and from Sec. 2.4 onwards, we take $d = 3$. We denote trajectories passing through a point $x_0 \in U$ at time t_0 by $x(\tau; t_0, x_0)$. For any time $\tau \in [t_0, t]$, we define the flow map as $F_{t_0}^{\tau}(x_0) := x(\tau;\, t_0,\, x_0)$.

Consider a set of initial positions forming a codimension-one surface $\mathcal{M}(t_0)$ at time t_0. Its time-τ image, $\mathcal{M}(\tau)$, termed a *material surface*, is obtained under the flow map, i.e., $\mathcal{M}(\tau) = F_{t_0}^{\tau}(\mathcal{M}(t_0))$. While any material surface divides locally the extended phase space, only special material surfaces with sustained coherence in time will act as transport barriers [9].

We proceed by defining the Cauchy-Green strain tensor field,

$$C_{t_0}^{t}(x_0) := \left[DF_{t_0}^{t}(x_0)\right]^{T} DF_{t_0}^{t}(x_0)\,, \tag{2.2}$$

with $DF_{t_0}^t(x_0)$ denoting the Jacobian matrix of $F_{t_0}^t$ expressed in the standard Euclidean basis, and the T-superscript referring to transposition (see [45] for the formulation on Riemannian manifolds). At each x_0, $C_{t_0}^t(x_0)$ is a symmetric and positive definite matrix. In two dimensions, $C_{t_0}^t(x_0)$ has two positive eigenvalues

$$0 < \lambda_1(x_0) \leq \lambda_2(x_0).$$

Unless the two eigenvalues are equal, the associated unit eigenvectors $\xi_{1,2}(x_0)$ form a well-defined, orthonormal basis. In three dimensions, $C_{t_0}^t(x_0)$ has three positive eigenvalues $\lambda_{1,2,3}(x_0)$, which we order as

$$0 < \lambda_1(x_0) \leq \lambda_2(x_0) \leq \lambda_3(x_0).$$

For incompressible flows, the product of the eigenvalues is unity, i.e., $\lambda_1(x_0) \cdot \lambda_2(x_0) \cdot \lambda_3(x_0) = 1$. Except at points $x_0 \in U$ where the eigenvalues of $C_{t_0}^t(x_0)$ are repeated, i.e., $\lambda_1(x_0) = \lambda_2(x_0)$ or $\lambda_2(x_0) = \lambda_3(x_0)$, the unit eigenvectors $\xi_1(x_0)$, $\xi_2(x_0)$ and $\xi_3(x_0)$ again form an orthonormal basis. Pointwise, we orient them so that $\xi_3(x_0) = \xi_1(x_0) \times \xi_2(x_0)$.

2.3 Review of elliptic Lagrangian Coherent Structures in two dimensions

Following the two-dimensional approach introduced in [37], consider a closed material curve of initial particle positions $\gamma(t_0)$. Over the finite time interval $[t_0, t]$, the averaged relative tangential stretching of $\gamma(t_0)$ is given by the strain functional

$$Q(\gamma(t_0), t) = \oint_{\gamma(t_0)} \sqrt{\frac{\langle x_0'(s),\, C_{t_0}^t(x_0(s))x_0'(s)\rangle}{\langle x_0'(s),\, x_0'(s)\rangle}}\, \mathrm{d}s\,, \tag{2.3}$$

where $x_0(s)$ is a parameterization of $\gamma(t_0)$, $x_0'(s) = dx_0/ds$ is the (non-unit) tangent vector to $\gamma(t_0)$, and $\langle .,. \rangle$ denotes the Euclidean inner product.

Stationary curves of the functional Q defined in (2.3) do not, by definition, exhibit leading-order variation in the averaged tangential strain. They are, therefore, non-filamenting curves that can be used to define *elliptic Lagrangian Coherent Structures* [37]. Mathematically, these elliptic LCSs solve the classic Euler–Lagrange equation associated with the Lagrangian

$$q(x_0, x_0') = \sqrt{\frac{\langle x_0',\, C_{t_0}^t(x_0)x_0'\rangle}{\langle x_0',\, x_0'\rangle}}\,.$$

The Lagrangian $q(x_0, x_0')$ has no explicit dependence on the curve parameter s and hence, by Noether's theorem [26], produces a first integral I for the Euler–Lagrange equation associated with the variational problem $\delta Q(\gamma, .) = 0$. Evaluated on stationary curves of Q, the first integral is of the form

$$I = q - \left\langle x_0', \partial_{x_0'} q \right\rangle = q = \text{const.}\,. \tag{2.4}$$

Denoting the constant in (2.4) by λ, we obtain that $q = \lambda$, which we rewrite as

$$\langle x_0'(s), C_{t_0}^t(x_0(s))x_0'(s)\rangle = \lambda^2 \langle x_0'(s), x_0'(s)\rangle. \tag{2.5}$$

Expressing (2.5) in the eigenbasis of $C_{t_0}^t(x_0)$, one finds that closed stationary curves of Q are closed integral curves of the vector fields

$$\eta_\lambda^\pm(x_0) = \sqrt{\frac{\lambda_2(x_0) - \lambda^2}{\lambda_2(x_0) - \lambda_1(x_0)}}\xi_1(x_0) \pm \sqrt{\frac{\lambda^2 - \lambda_1(x_0)}{\lambda_2(x_0) - \lambda_1(x_0)}}\xi_2(x_0)\,. \tag{2.6}$$

As these curves satisfy (2.5) at each point, they are guaranteed to stretch uniformly by a factor of λ. For such a curve, denoted by $\gamma(t_0)$, the stretching factor λ is a positive number between $\max_{x_0 \in \gamma(t_0)} \sqrt{\lambda_1(x_0)}$ and $\min_{x_0 \in \gamma(t_0)} \sqrt{\lambda_2(x_0)}$. In the particular case of $\lambda = 1$, these stationary curves of Q experience no stretching between the times t_0 and t. We refer to this case of perfect coherence as *neutral stretching.*

2.4 Uniformly and near-uniformly stretching material surfaces in three-dimensional flows

2.4.1 Uniform stretching in three-dimensional flow

As outlined above, in two dimensions, elliptic LCSs are non-filamenting, closed material curves that are infinitesimally λ-stretching. A straightforward generalization to three dimensions is to seek two-dimensional tubular surfaces that are uniformly stretching by a factor of λ along all directions in each of their tangent spaces. We now explore this idea in detail.

Definition 2.1. A smooth material surface $\mathcal{M}(\tau)$ *is pointwise uniformly stretching* if, under advection from time t_0 to t, all vectors in each tangent space $T_{x_0}\mathcal{M}(t_0)$ stretch uniformly by the same factor $\lambda(x_0) \in [\sqrt{\lambda_1(x_0)}, \sqrt{\lambda_3(x_0)}]$.

We illustrate the basic idea of Definition 2.1 in Figure 2.1. The definition translates to the explicit requirement that

$$\sqrt{\frac{\langle v,\, C_{t_0}^t(x_0)\, v\rangle}{\langle v,\, v\rangle}} = \lambda(x_0)\,, \quad \forall x_0 \in \mathcal{M}(t_0),\, \forall v \in T_{x_0}\mathcal{M}(t_0). \tag{2.7}$$

Theorem 2.1. *In three-dimensional flow, as given by (2.1) with* $d = 3$*, any pointwise uniformly stretching material surface* $\mathcal{M}(\tau)$ *would have to satisfy* $\lambda(x_0) = \sqrt{\lambda_2(x_0)}$*.*

Proof. Consider an arbitrary pointwise uniformly stretching surface $\mathcal{M}(\tau)$. At any point $x_0 \in \mathcal{M}(t_0)$ where $C_{t_0}^t$ has distinct eigenvalues, we examine the condition for pointwise uniform stretching (2.7) by considering an arbitrary tangent vector $v \in T_{x_0}\mathcal{M}(t_0)$. Dropping the position argument for brevity, we use the eigenbasis $\xi_{1,2,3}$ to write $v = \alpha\xi_1 + \beta\xi_2 + \gamma\xi_3$. By orthonormality of the $\xi_{1,2,3}$, (2.7) then becomes $\alpha^2\lambda_1 + \beta^2\lambda_2 + \gamma^2\lambda_3 = \lambda^2(\alpha^2 + \beta^2 + \gamma^2)$, or equivalently,

$$\alpha^2(\lambda^2 - \lambda_1) + \beta^2(\lambda^2 - \lambda_2) + \gamma^2(\lambda^2 - \lambda_3) = 0. \tag{2.8}$$

As shown in Table 2.1, condition (2.8) only provides full linear spaces of solutions for

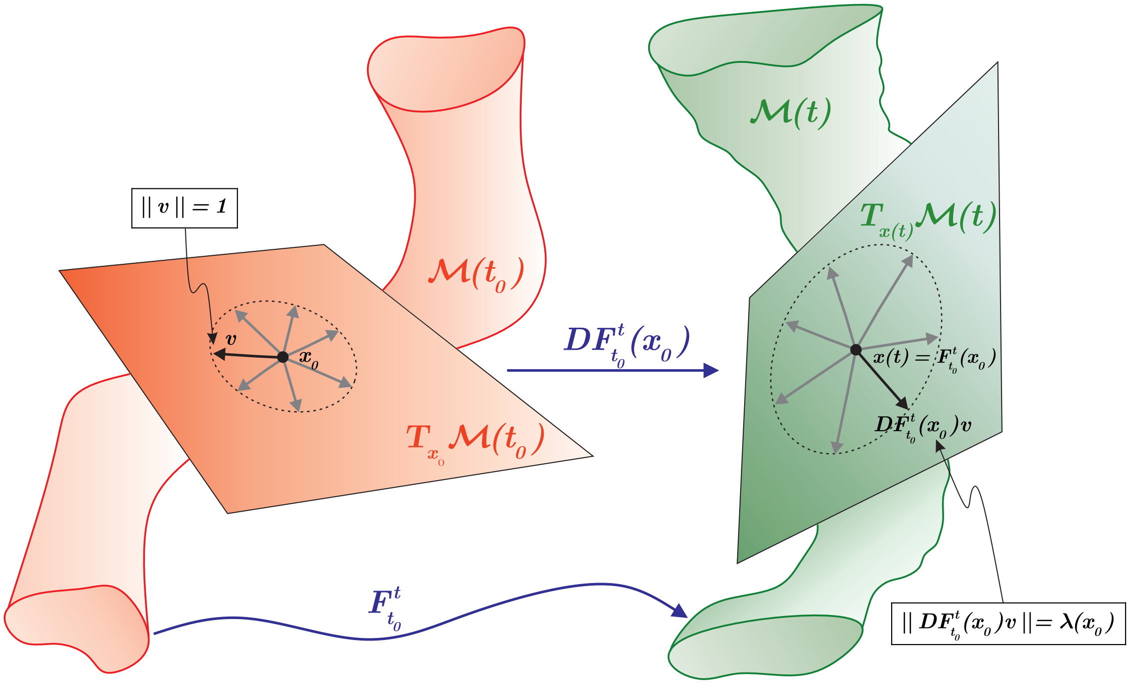

Fig. 2.1: Illustration of a tubular pointwise uniformly stretching surface as introduced in Definition 2.1.

$\lambda = \sqrt{\lambda_2}$ (Case 3). Here the solution set of (2.8) consists of two planes (cf. Fig. 2.2b). For a generic choice of λ, on the other hand, the solution set of (2.8) is a double cone (Cases 2, 4 in Table 2.1). In the remaining two cases of $\lambda = \sqrt{\lambda_1}$ and $\lambda = \sqrt{\lambda_3}$, the solution set of (2.8) is a line (Cases 1, 5 in Table 2.1). The tangent plane $T_{x_0}\mathcal{M}(t_0)$, therefore, has to coincide with one of the two planes obtained for $\lambda = \sqrt{\lambda_2}$ (Case 3). (For points where $C^t_{t_0}$ has repeated eigenvalues, see Appendix 2.B.) $\square$

Case	Values of λ	Geometry of solution set of (2.8)
1	$\lambda = \sqrt{\lambda_1}$	ξ_1-axis (cf. Fig. 2.2a, Appendix 2.A)
2	$\sqrt{\lambda_1} < \lambda < \sqrt{\lambda_2}$	Elliptic double cone about ξ_1-axis (cf. Fig. 2.2a, Appendix 2.C)
3	$\lambda = \sqrt{\lambda_2}$	Two planes (cf. Fig. 2.2b, Appendix 2.A)
4	$\sqrt{\lambda_2} < \lambda < \sqrt{\lambda_3}$	Elliptic double cone about ξ_3-axis (cf. Fig. 2.2c , Appendix 2.C)
5	$\lambda = \sqrt{\lambda_3}$	ξ_3-axis (cf. Fig. 2.2c, Appendix 2.A)

Table 2.1: Solution sets of (2.8) depending on the choice of λ.

Remark 2.1. As opposed to the neutral stretching $\lambda = 1$ in two dimensions, the

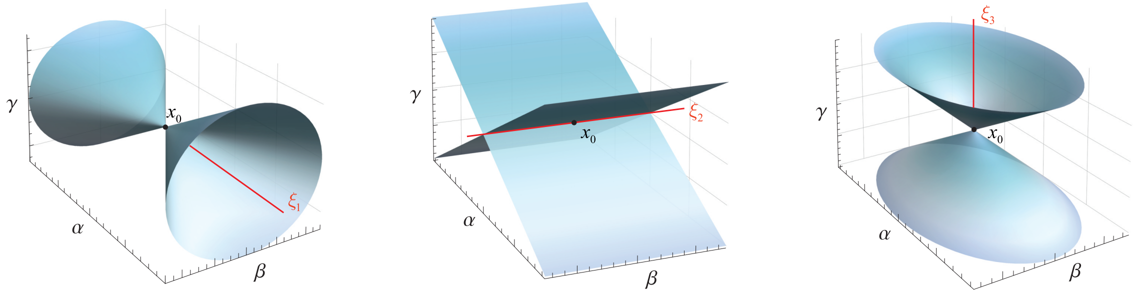

(a) Case 2: λ-stretching directions forming a double cone for $\lambda \in (\sqrt{\lambda_1}, \sqrt{\lambda_2})$.

(b) Case 3: Two planes formed by $\lambda = \sqrt{\lambda_2}$-stretching directions.

(c) Case 4: λ-stretching directions forming a double cone for $\lambda \in (\sqrt{\lambda_2}, \sqrt{\lambda_3})$.

Fig. 2.2: Directions of λ-stretching for Cases 2, 3, 4 in Table 2.1.

three-dimensional analogue of neutral stretching is $\lambda(x_0) = \sqrt{\lambda_2(x_0)}$, representing the only case that allows for the construction of a pointwise uniformly stretching surface $\mathcal{M}(\tau)$. Viewed globally, however, these surfaces cannot be expected to stretch uniformly, since their pointwise stretching factor $\sqrt{\lambda_2(x_0)}$ generally varies in space. The uniformity in stretching refers to their tangent spaces only, and should therefore be viewed as a local property.

Remark 2.2. In order to construct a *globally* uniformly stretching surface, by Theorem 2.1, we would need to find a pointwise $\lambda(x_0)$-stretching surface whose intersection with a particular level set of $\lambda_2(x_0)$ is still a two-dimensional surface. There is generally no reason for this to hold, so we will always consider material surfaces $\mathcal{M}(\tau)$ that are *pointwise* uniformly stretching with a spatially dependent factor $\lambda(x_0) = \sqrt{\lambda_2(x_0)}$. (In the following, for brevity, we therefore sometimes omit the 'pointwise' attribute.) Such surfaces are of intrinsic interest, as pointwise uniform stretching imposes observable coherence in the deformation of tracer blobs.

Remark 2.3. As we show in Appendix 2.D, for a pointwise uniformly stretching surface $\mathcal{M}(t_0)$, all vectors within each tangent space $T_{x_0}\mathcal{M}(t_0)$ *keep their originally enclosed angle* when mapped from time t_0 to time t. They are stretched equally by $\sqrt{\lambda_2(x_0)}$, but are otherwise rotated by the same angle. This means that there is no net material shear *within* the tangent space of the surface $\mathcal{M}(t_0)$ as it evolves into $\mathcal{M}(t)$.

Remark 2.4. At any point x_0 of a pointwise uniformly stretching surface $\mathcal{M}(t_0)$ where $C_{t_0}^t(x_0)$ has distinct eigenvalues, we find that the surface $\mathcal{M}(t_0)$ must be normal to one of the two unit vectors

$$n^{\pm}(x_0) = \sqrt{\frac{\lambda_2(x_0) - \lambda_1(x_0)}{\lambda_3(x_0) - \lambda_1(x_0)}}\xi_1(x_0) \pm \sqrt{\frac{\lambda_3(x_0) - \lambda_2(x_0)}{\lambda_3(x_0) - \lambda_1(x_0)}}\xi_3(x_0) \tag{2.9}$$

(cf. Appendix 2.A). The vectors $n^{\pm}(x_0)$ are precisely the unit normals to the two planes obtained from (2.8) for the case $\lambda(x_0) = \sqrt{\lambda_2(x_0)}$.

2.4.2 Pointwise near-uniformly stretching surfaces

Based on the considerations above, we seek elliptic LCSs as tubular material surfaces built out of material curves $\gamma(t_0) \subset \mathbb{R}^3$ that are stationary curves of the functional

$$S(\gamma(t_0), t) = \int_{\gamma(t_0)} \sqrt{\frac{\langle x_0'(s),\, \tilde{C}_{t_0}^t(x_0(s))x_0'(s)\rangle}{\langle x_0'(s),\, x_0'(s)\rangle}}\,\mathrm{d}s\,. \tag{2.10}$$

Here the integrand measures how $\gamma(t_0)$ stretches under the normalized Cauchy-Green tensor

$$\tilde{C}_{t_0}^t(x_0) = \frac{1}{\lambda_2(x_0)}C_{t_0}^t(x_0).$$

This normalization represents a slight modification of the functional introduced earlier in (2.3), accounting for the fact that the analogue of neutral stretching in three dimensions is given by $\lambda = \sqrt{\lambda_2}$ (see Remark 2.1).

By Noether's theorem [26], the integrand in (2.10) is conserved along stationary curves $x_0(s)$ of S. Therefore, on these stationary curves, we have

$$\sqrt{\frac{\langle x_0'(s), C_{t_0}^t(x_0(s))x_0'(s)\rangle}{\langle x_0'(s), x_0'(s)\rangle}} = \sqrt{\lambda_2(x_0)(1+\delta)} =: \lambda(x_0), \tag{2.11}$$

with the value of the conserved integrand in (2.10) being equal to the constant value $\sqrt{1+\delta}$. Comparing (2.11) to (2.7), we see that stationary curves of S stretch non-uniformly by $\lambda(x_0)$. The constant parameter δ measures the deviation of stretching from the value of neutral stretching $\sqrt{\lambda_2(x_0)}$.

For a given flow under consideration, one cannot expect that there exists a tubular surface that is precisely pointwise uniformly stretching everywhere ($\delta = 0$). Moreover, even if such a surface existed, unavoidable numerical inaccuracies and sensitivities would render it indetectable. We therefore extend our considerations to surfaces built out of curves that stretch by a factor close to $\sqrt{\lambda_2}$ ($|\delta| \ll 1$). In general, away from points where $C_{t_0}^t(x_0)$ has repeated eigenvalues, λ-values satisfying

$$\lambda^2(x_0) = \lambda_2(x_0)\,(1+\delta)\,, \qquad \delta \in \left[-1 + \frac{\lambda_1(x_0)}{\lambda_2(x_0)}\right) \cup \left(-1 + \frac{\lambda_3(x_0)}{\lambda_2(x_0)}\right],$$

yield elliptic cones of uniform stretching directions, and therefore do not define possible tangent spaces for a λ-stretching surface (cf. Theorem 2.1). For $|\delta| \ll 1$, however, these cones become elongated along the ξ_2-axis, and hence large subsets of them are C^1-close to pairs of planes with respective unit normals $\pm n_\delta^\pm(x_0)$, where

$$n_\delta^\pm(x_0) = \sqrt{\frac{\lambda_2(x_0)\,(1+\delta) - \lambda_1(x_0)}{\lambda_3(x_0) - \lambda_1(x_0)}}\,\xi_1(x_0) \pm \sqrt{\frac{\lambda_3(x_0) - \lambda_2(x_0)\,(1+\delta)}{\lambda_3(x_0) - \lambda_1(x_0)}}\,\xi_3(x_0). \quad (2.12)$$

Unless needed, we omit the overall sign for the orientation of the normal direction $n_\delta^\pm$ in the following. The expression (2.12) is well-defined for all points x_0 where the Cauchy-Green strain tensor has distinct eigenvalues and $\delta \in \left[-1 + \frac{\lambda_1(x_0)}{\lambda_2(x_0)}, -1 + \frac{\lambda_3(x_0)}{\lambda_2(x_0)}\right]$. We illustrate the situation in Fig. 2.3, and give further details in Appendix 2.C. We point out that by setting $\delta = 0$ in (2.12), we recover the pair of planes forming the solution set of (2.5) for the uniform case $\lambda(x_0) = \sqrt{\lambda_2(x_0)}$.

The vectors $n_\delta^\pm(x_0)$ from (2.12) turn out to be the optimal choices as normals for surfaces with the smallest possible stretching variations in their tangent spaces:

Proposition 2.1. *At each point x_0 with distinct eigenvalues for $C_{t_0}^t$, and for any prescribed value $\lambda = \sqrt{\lambda_2(1+\delta)} \in [\sqrt{\lambda_1}, \sqrt{\lambda_3}]$ of stretching, the planes normal to the vectors $\pm n_{\lambda^2/\lambda-1}^\pm$ defined in (2.12) experience the smallest possible inhomogeneity in stretching around the value λ. The range of stretching values attained within these planes is the interval $[\min\{\lambda, \sqrt{\lambda_2}\}, \max\{\lambda, \sqrt{\lambda_2}\}]$.*

Proof. See Appendix 2.E. □

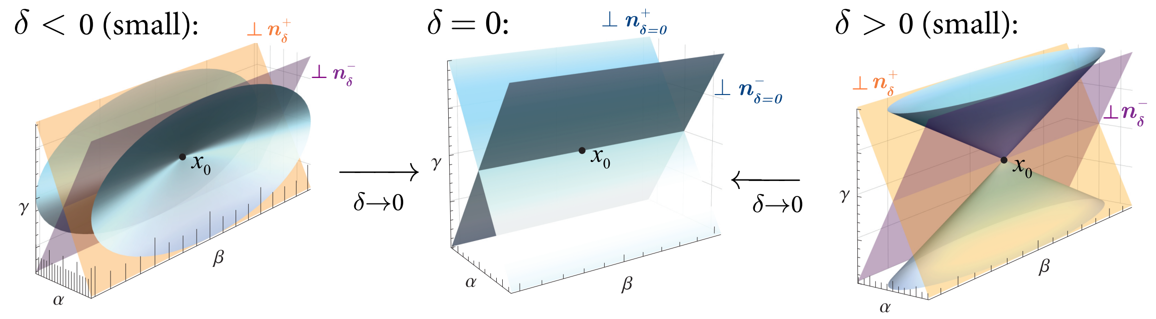

Fig. 2.3: Elongated elliptic double cones formed by $\sqrt{\lambda_2(1+\delta)}$-stretching directions collapse onto a pair of planes for $\delta \to 0$. As long as δ is small, the double cones are well approximated by two planes tangent to them, colored purple and orange here. In Proposition 2.1, we show that these planes define tangent spaces of surfaces that are pointwise most uniformly stretching, as described in Definition 2.2. We give the expression for their unit normals $n_\delta^\pm$ in (2.12).

We now use the unit normals $n_\delta^\pm(x_0)$ (which are optimal in the sense of Proposition 2.1) to define the most uniformly stretching surfaces possible, along which the stretching of tangent vectors varies by no more than a specified percentage around $\sqrt{\lambda_2(x_0)}$. To this end, we introduce a relative stretching variation Δ, $0 \leq \Delta < 1$, such that for any δ,

$$\sqrt{\lambda_2}(1-\Delta) \leq \sqrt{\lambda_2(1+\delta)} \leq \sqrt{\lambda_2}(1+\Delta).$$

Restricting ourselves to small Δ and allowing δ to generally vary along the surface, we introduce the following definition:

Definition 2.2. A smooth material surface $\mathcal{M}_\Delta(\tau)$ is *pointwise nearly uniformly stretching* with stretching variation Δ, $0 \leq \Delta \ll 1$, if for all $x_0 \in \mathcal{M}_\Delta(t_0)$, either $n^+_{\delta(x_0)}(x_0) \perp T_{x_0}\mathcal{M}_\Delta(t_0)$ or $n^-_{\delta(x_0)}(x_0) \perp T_{x_0}\mathcal{M}_\Delta(t_0)$ holds, with $\delta(x_0) \in [-2\Delta + \Delta^2, 2\Delta + \Delta^2]$.

Remark 2.5. In the present study, we seek *elliptic Lagrangian Coherent Structures* as pointwise near-uniformly stretching surfaces (cf. Definition 2.2). We note that the shear-maximizing material surfaces, used in a previous approach to elliptic LCSs in three dimensions [9] (cf. Sec. 2.1), can also be obtained from normals $\tilde{n}^\pm$ of the general form $\tilde{n}^{\pm} = a\xi_1 \pm b\xi_3$.

Remark 2.6. Instead of considering variations of closed material curves (2.10), it would be desirable to derive near-uniformly stretching surfaces (cf. Definition 2.2) from a variational principle for two-dimensional manifolds with boundary [75]. We expect, however, that such a variational problem would be significantly more difficult than the minimal surface problem (see [67] for a review). Deriving a general algebraic condition similar to the expression for the surface normal (2.12) is out of reach here, and hence would necessitate a purely numerical approach.

2.5 Numerical extraction of near-uniformly stretching surfaces

2.5.1 Outline of the extraction procedure

Consider being given a three-dimensional velocity field u (2.1) over a finite time interval $[t_0, t]$. Our goal is to numerically locate elliptic LCSs by seeking time-t_0 positions of near-uniformly stretching material surfaces $\mathcal{M}_\Delta(\tau)$. Their admissible normals $n_\delta^\pm$ are given in (2.12), to be used in a surface-extraction procedure similar to the one in [9].

The idea behind this procedure is to sample the flow domain using an indexed family of N reference planes $(\Pi_i)_{i\in\{1,2,\dots,N\}}$, and then assemble each elliptic LCS by computing its intersections with each reference plane $\Pi \in \{\Pi_i\}$. Such intersection curves $x_0(s)$ have tangent vectors that are normal to both $n_\delta^\pm$ and the normal n_Π of Π. Consequently, the intersection curves are limit cycles of the vector field

$$x_0' = \eta_{\delta,i}^\pm(x_0) := n_{\Pi_i}(x_0) \times n_\delta^\pm(x_0). \tag{2.13}$$

Because $n_\delta^\pm$ are continuous families of direction fields parametrized by δ, we need to scan the interval $\delta \in [-2\Delta + \Delta^2, 2\Delta + \Delta^2]$ to find limit cycles of (2.13). This procedure typically yields a large number of limit cycles in each reference plane Π_i.

The challenge is to combine single limit cycles from each Π_i into a smooth tubular surface $\mathcal{M}_\Delta(t_0)$. Moreover, using the Frobenius integrability theorem, one can show that a necessary condition for the existence of a smooth surface $\mathcal{M}(t_0)$ normal to a smooth vector field n is that the helicity H_n of n vanishes for all points in the surface $\mathcal{M}(t_0)$ [9]. In our case, with $n = \pm n_\delta^\pm$ and $\mathcal{M}(t_0){=}\mathcal{M}_\Delta(t_0)$, the helicity condition reads

$$H_{n_\delta^\pm} = \left\langle \nabla \times n^\pm_{\delta(x_0)}, n^\pm_{\delta(x_0)} \right\rangle = 0. \tag{2.14}$$

Such a helicity condition has already been considered by others [68, 71] for the visualization of surfaces approximately perpendicular to an imposed normal field.

We remark that the procedure outlined above requires computing the flow map $F_{t_0}^t$ and hence the normals $n_\delta^\pm$ (2.12) as fields over the domain of initial positions. In applications where the velocity field u (2.1) is given numerically (from either an experiment or a numerical simulation), the resolution of the velocity data therefore needs to be sufficiently high in both space and time.

2.5.2 Selecting closed orbits for the construction of elliptic LCSs

We now explain how to select the closed orbits of $\eta^\pm_{\delta,i}$ needed for constructing an elliptic LCS $\mathcal{M}_\Delta(t_0)$. Specifically, for a sequence of reference planes $\Pi_{i_0,}\Pi_{i_0+1}, ...,$ in each plane Π_i, we need to identify a single optimal limit cycle of $\eta^\pm_{\delta,i}$ (labeled γ_i). We do this by introducing an auxiliary surface $\mathcal{S}(t_0)$, and, for each plane Π_i, selecting γ_i as the closed orbit closest to the intersection curve $\mathcal{S}(t_0) \cap \Pi_i$.

Considering (2.12), we first observe that at each point $x_0 \in \mathcal{M}_\Delta(t_0)$, we would need to have $\mathcal{M}_\Delta(t_0) \parallel \xi_2$. Now consider that, in an initial reference plane Π_1, we have computed a curve γ_1 as a closed orbit of $\eta^\pm_{\delta,1}$. Away from points with repeated eigenvalues of $C_{t_0}^t$, advecting γ_1 under the ξ_2-field then yields a smooth tubular surface $\mathcal{S}(t_0)$ that is tangent to ξ_2, just as $\mathcal{M}_\Delta(t_0)$ should be. We then compute intersections of $\mathcal{S}(t_0)$ with the remaining reference planes $\Pi_{i=2,3,...}$. In each reference plane Π_i, from the set of all available closed orbits of $\eta^\pm_{\delta,i}$ (denoted by Γ_i), select the orbit γ_i

minimizing the min-distance to the intersection curve $\mathcal{S}(t_0) \cap \Pi_i$. That is, for each $\tilde{\gamma} \in \Gamma_i$ evaluate

$$d(\tilde{\gamma}, \mathcal{S}(t_0) \cap \Pi_i) = \min_{q \in \tilde{\gamma}, p \in \mathcal{S}(t_0) \cap \Pi_i} \| q - p \|, \tag{2.15}$$

and take the orbit $\tilde{\gamma}$ that minimizes the above expression as γ_i. At the end, interpolate the surface $\mathcal{M}_\Delta(t_0)$ from the collection of closed orbits $\gamma_i \parallel \eta^{\pm}_{\delta,i}$.

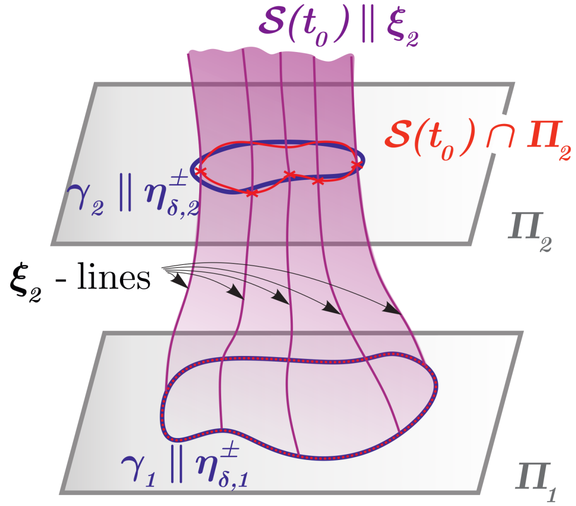

Fig. 2.4: Identifying the best candidate orbit of $\eta^{\pm}_{\delta,2}$ in the Π_2-plane as the one with minimal distance to points of $\mathcal{S}(t_0) \cap \Pi_2$. Instead of computing the entire surface $\mathcal{S}(t_0)$, only few integral curves tangent to the ξ_2-field (ξ_2-lines) may already indicate a useful candidate orbit.

The surface $\mathcal{M}_\Delta(t_0)$ obtained from the above procedure (cf. Fig. 2.4) will generally not satisfy the helicity condition (2.14), because it will not be exactly tangent to ξ_2. The surface $\mathcal{S}(t_0)$ is, however, tangent to ξ_2. In addition, locally, $\mathcal{S}(t_0)$ has a smooth normal field of the general form $\pm n^{\pm}_{\delta(x_0)}$ (see (2.12)), and therefore satisfies a helicity condition of the type (2.14) (see Appendix 2.F); $\delta(x_0) \in [-1 + \frac{\lambda_1(x_0)}{\lambda_2(x_0)}, -1 + \frac{\lambda_3(x_0)}{\lambda_2(x_0)}]$ is unknown on $\mathcal{S}(t_0)$ and possibly exceeds the range $[-2\Delta + \Delta^2, 2\Delta + \Delta^2]$. The above observations thus render the surface $\mathcal{M}_\Delta(t_0)$ as close to a surface $\mathcal{S}(t_0)$ that satisfies both tangency to ξ_2 and a helicity condition of the intended functional form (2.14).

For the examples we study in Sec. 2.6, we find that it is not necessary to construct a full two-dimensional surface $\mathcal{S}(t_0)$ by advecting the entire orbit γ_1 under the ξ_2-

field. It turns out that data points obtained from very few integral curves of ξ_2, launched from arbitrary points on γ_1 (cf. Fig. 2.4), already lead to robust assessments of the min-distance (2.15). This discretization of $\mathcal{S}(t_0)$ will therefore barely affect the selection of closed orbits $\gamma_{2,3,...}$ for building a near-uniformly stretching material surface $\mathcal{M}_\Delta(t_0)$.

2.5.3 Summary of the extraction procedure

Here we briefly summarize the numerical extraction procedure for elliptic LCSs, $\mathcal{M}_\Delta(t_0)$ (see Appendix 2.G for details).

Part 1 (computation of closed orbits): Sample the flow domain by defining a parallel stack of references plane Π_i. For each reference plane Π_i, compute the Cauchy-Green strain tensor $C_{t_0}^t$ on a square main grid. Using bilinear interpolation of the Cauchy-Green eigenvectors $\xi_{1,2,3}$ and eigenvalues $\lambda_{1,2,3}$, compute closed integral curves of $\eta_{\delta,i}^\sigma$, looping over both $\sigma = +, -$ and $\delta \in [-2\Delta + \Delta^2, 2\Delta + \Delta^2]$.

Part 2 (interpolation of closed orbits to an elliptic LCS surface): Consider the first reference plane Π_{i_0} containing at least one closed orbit of $\eta_{\delta=0,i_0}^\pm$ in the region of interest. For visualizing the vortex boundary, pick the outermost closed orbit of $\eta_{\delta=0,i_0}^\pm$, denoted by γ_{i_0}. Starting from points on γ_{i_0}, integrate curves tangent to the ξ_2-line field (ξ_2-lines) until each reference plane containing closed orbits of $\eta_{\delta,i}^\pm$ is intersected at least once. Iterate through the following reference planes Π_i ($i = i_0 + 1, i_0 + 2, ...$), and, in each, select the closed orbit of $\eta_{\delta,i}^\pm$, labeled γ_i, closest to the intersection points between Π_{i_0+1} and the ξ_2-line(s) (in the sense described in Sec. 2.5.2). At the end, use the data points given by the collection of closed orbits $\{\gamma_i\}$ of the $\eta_{\delta,i}^\pm$ -fields to interpolate a smooth surface $\mathcal{M}_\Delta(t_0)$.

2.6 Examples

2.6.1 Steady ABC flow

We consider the steady ABC flow, a stationary solution of the Euler equations. In Cartesian coordinates (x, y, z), its velocity field is given by

$$u(x, y, z) = \begin{pmatrix} A\sin(z) + C\cos(y) \\ B\sin(x) + A\cos(z) \\ C\sin(y) + B\cos(x) \end{pmatrix}, \tag{2.16}$$

where we select $A = \sqrt{3}$, $B = \sqrt{2}$, $C = 1$. For these parameter values, the ABC flow is known to contain several distinct vortical regions in the midst of a bulk of chaotic trajectories [16]. The flow domain is the three-torus $\mathbb{T}^3$ or, equivalently, a cube of $[0, 2\pi]^3$ with periodic boundary conditions imposed on each face.

We sample the flow domain using a family of 100 uniformly spaced reference planes perpendicular to the z-axis, each of them given by

$$\Pi_i = \{(x, y, z) \in [0, 2\pi]^3 |\, z = (i-1)\cdot 2\pi/100\}\,, \quad i = 1, ..., 100.$$

Choosing the extraction window as $[t_0, t] = [0, 40]$, we analyze the vortical region located around ($x \approx 3.7$, $y \approx 4.7$, $z \approx 0.0$), seeking the largest elliptic LCS as a nearly uniformly stretching surface $\mathcal{M}_\Delta(t_0)$ with pointwise relative stretching deviation up to $\Delta = 0.1$ (see Appendix 2.H for the remaining numerical details).

We scan the parameter window $\delta \in [-0.19, 0.21]$ using 80 uniformly spaced δ-values, and in addition run $\delta = 0$ to identify closed orbits of $\eta^{\pm}_{\delta,i}$ on all reference planes. In Fig. 2.5, we visualize part of the flow in lowest reference plane Π_1 using the Finite-time Lyapunov Exponent (FTLE) field $[2(t-t_0)]^{-1}\log\lambda_3$, and superimpose the closed orbits of $\eta^{\pm}_{\delta,1}$. The procedure described in *Part 2* of Appendix 2.G then leads us to building the outermost elliptic LCS starting from the orbit γ_1 indicated in Fig. 2.5. For the selection of the remaining closed orbits $\gamma_{2,...,100}$, we integrate one trajectory of ξ_2 from $(x \approx 4.34, y \approx 4.19, z = 0.0) \in \gamma_1$ to $(x \approx 3.17, y \approx 5.11, z \approx 6.22) \in \Pi_{100}$.

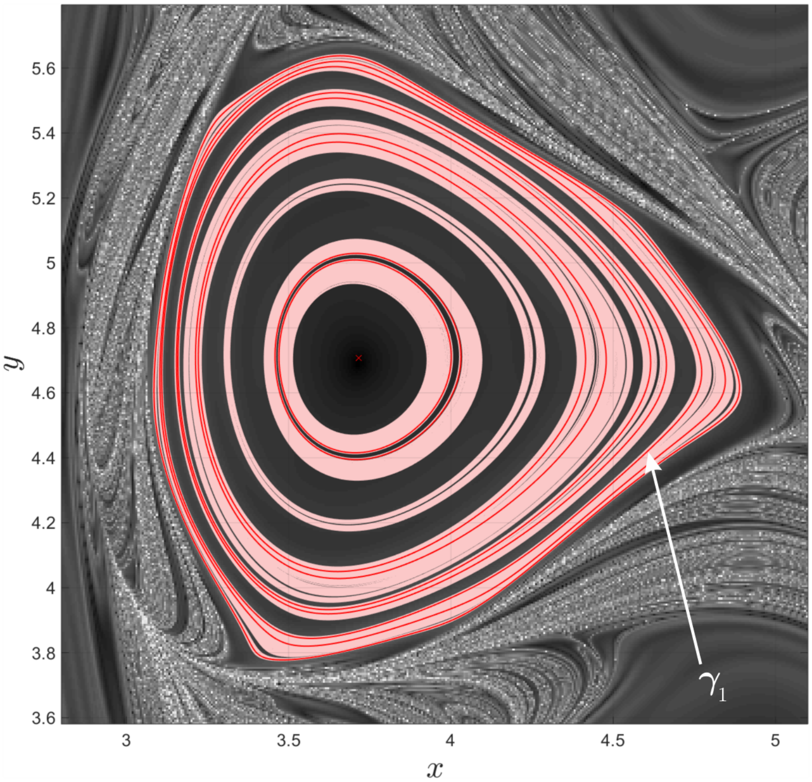

Fig. 2.5: Steady ABC flow, time-window $[0, 40]$: Closed orbits of $\eta^{\pm}_{\delta,1}$ with $\delta \in [-0.19, 0.21]$ in the plane Π_1, displaying curves with $\delta = 0$ in strong red and with $\delta \neq 0$ in light red. The red cross indicates the approximate vortex center. The curve γ_1 is used as the initial orbit in the assembly of the elliptic LCS. Background visualization: Finite-time Lyapunov exponent field.

We show the arclength and δ-value of each orbit $\gamma_{1,\dots,100}$ in Figs. 2.6a, 2.6b. These provide qualitative insight into smoothness and stretching variation of the tubular surface $\mathcal{M}_\Delta(t_0)$ that we then create from the orbits $\gamma_{1,\dots,100}$ by interpolation. For better visualization of $\mathcal{M}_\Delta(t_0)$, we use toroidal coordinates $(\bar{x}, \bar{y}, \bar{z})$,

$$\begin{aligned}
\bar{x} &= (x - x_c(z) + R_1)\cos(z), \\
\bar{y} &= (x - x_c(z) + R_1)\sin(z), \\
\bar{z} &= R_2(y - y_c(z)).
\end{aligned}$$

with $x_c(z)$, $y_c(z)$ parametrizing the vortex center (extracted heuristically by local FTLE minima), and $R_1 = 2$, $R_2 = 1$. In Fig. 2.7a, we show the final result for the elliptic LCS surface $\mathcal{M}_\Delta(t_0)$ in red. We place a toroidal cloud of tracers closely

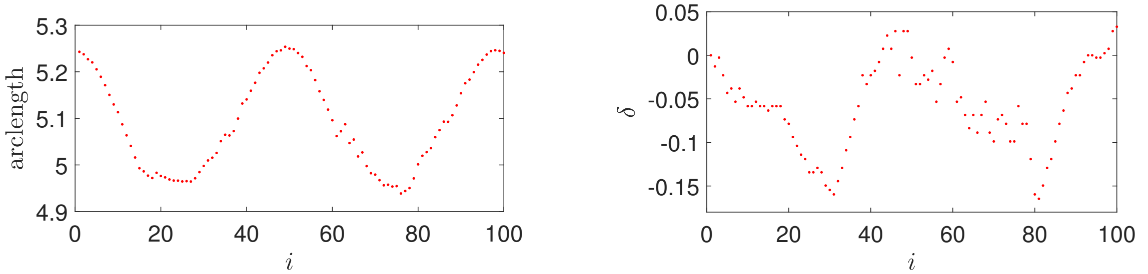

(a) Arclengths of the closed orbits γ_i selected on each reference plane.

(b) Values of δ of the closed orbits γ_i selected on each reference plane.

Fig. 2.6: Steady ABC flow, time-window $[0, 40]$: Properties of the closed orbits $\gamma_{1,\ldots,100}$ used to build an elliptic LCS.

around $\mathcal{M}_\Delta(t_0)$ (purple dots), and then advect these together with $\mathcal{M}_\Delta(t_0)$ over the time-window of extraction, as shown in Fig. 2.7b. With the elliptic LCS at the final time $\mathcal{M}_\Delta(t)$ displayed in green, we observe that $\mathcal{M}_\Delta(t)$ preserves its coherence, while the purple tracer cloud disperses into a complex geometric structure.

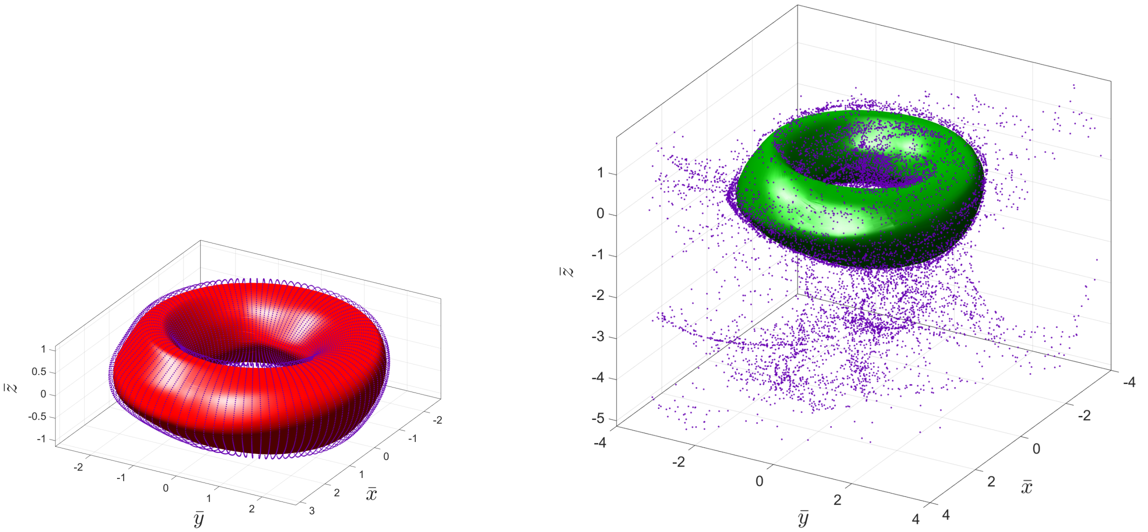

(a) Red: elliptic LCS $\mathcal{M}_{\Delta=0.1}(t_0 = 0)$, extracted for the time-interval $[0, 40]$. Purple: Locations of tracers placed closely outside the LCS surface.

(b) Green: time-40 advected image of the elliptic LCS in Fig. 2.7a, purple: Tracers advected from the locations in Fig. 2.7a.

Fig. 2.7: Steady ABC flow, time-window $[0, 40]$: Advecting the elliptic LCS from $t_0 = 0$ to $t = 40$, in comparison to nearby tracers, which spread incoherently.

For a longer extraction window $[t_0, t] = [0, 250]$, we also want to verify whether invariant tori of the steady ABC flow are well approximated by the elliptic LCSs we extract. In Fig. 2.8 we show a Poincaré map indicating all the invariant tori together with closed orbits of $\eta^{\pm}_{\delta,1}$ in the Π_1-reference plane. Here the relative stretching deviation we allow is again $\Delta = 0.1$, with the same sampling of δ-values as above. Compared with Fig. 2.5, more closed orbits with $\delta = 0$ are visible, indicating that there are more elliptic LCSs than for a shorter extraction time. As expected, the KAM tori are closely aligned with the elliptic LCSs. We show a representative elliptic LCS in Fig. 2.9.

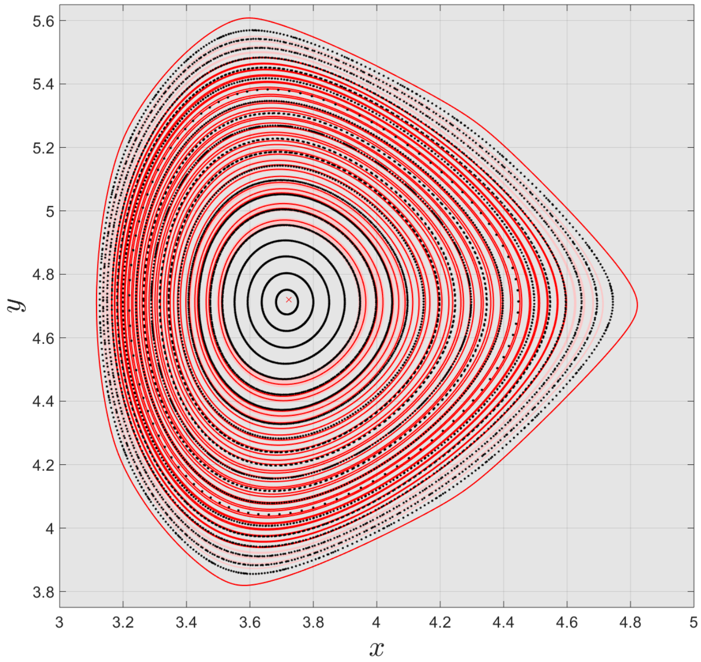

Fig. 2.8: Steady ABC flow, time-window $[0, 250]$: Closed orbits of $\eta^{\pm}_{\delta,1}$ with $\delta \in [-0.19, 0.21]$ in the plane Π_1, displaying curves with $\delta = 0$ in strong red and with $\delta \neq 0$ in light red. The red cross indicates the approximate vortex center. Black: Poincaré map obtained from the long-time behavior of multiple trajectories of (2.16).

2.6.2 Time-aperiodic ABC-type flow

We consider a time-aperiodic modification of the ABC flow,

$$u(x, y, z, \tau) = \begin{pmatrix} A_0 \sin(z) + (C_0 + C(\tau)) \cos(y) \\ (B_0 + B(\tau)) \sin(x) + A_0 \cos(z) \\ (C_0 + C(\tau)) \sin(y) + (B_0 + B(\tau)) \cos(x) \end{pmatrix}, \qquad (2.17)$$

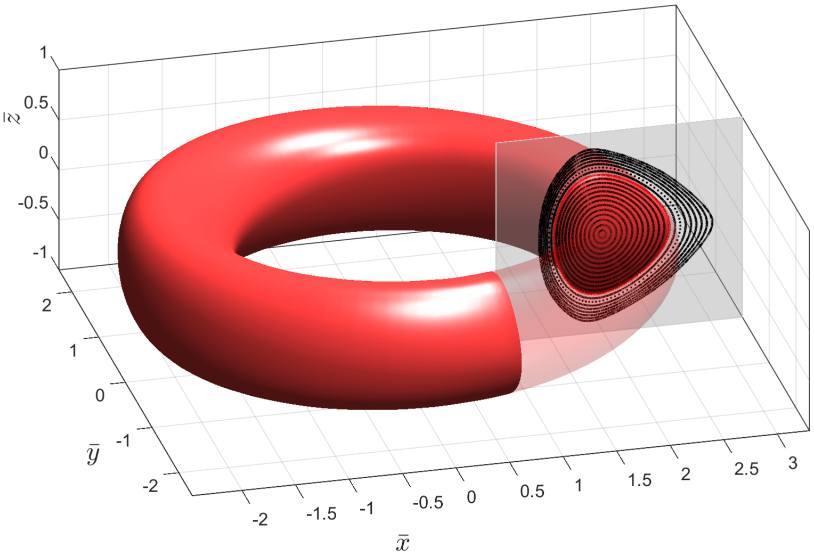

Fig. 2.9: Steady ABC flow, time-window $[0, 250]$: Representative 3D elliptic LCS and Poincaré map from Fig. 2.8.

with $A_0 = \sqrt{3}$, $B_0 = \sqrt{2}$, $C_0 = 1$. The added time-dependent perturbations are

$$\begin{aligned} B(\tau) &= B_0 k_0 \tanh(k_1 \tau) \cos((k_2 \tau)^2), \\ C(\tau) &= C_0 k_0 \tanh(k_1 \tau) \sin((k_2 \tau)^2), \end{aligned}$$

where $k_0 = 0.15$, $k_1 = 0.05$ and $k_2 = 0.12$. We plot $B(\tau)$, $C(\tau)$ in Fig. 2.10. The time-dependence we have selected for these functions models how the steady ABC flow, a locally unstable solution to the Euler equations [23], develops oscillations followed by saturation into another ABC-type flow with aperiodic time-dependence.

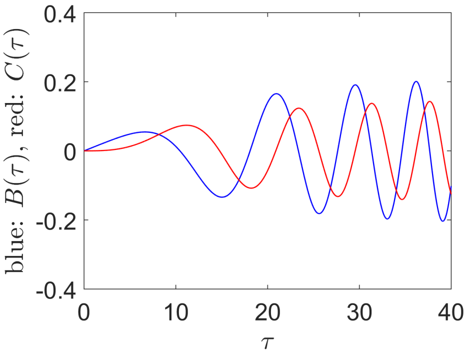

Fig. 2.10: Time-dependence of the coefficients of the unsteady ABC-type flow (2.17).

Like for the steady ABC flow, we consider the time-interval $[0, 40]$, and analyze the vortical region located around ($x \approx 3.7$, $y \approx 4.7$, $z \approx 0.0$). We allow a pointwise stretching variation $\Delta = 0.15$ for constructing the barrier, sampling the interval of $\delta \in [-0.2775, 0.3225]$ with 160 uniformly spaced values and, in addition, $\delta = 0$ (see Appendix 2.H for the remaining numerical details). We show the closed orbits of $\eta^{\pm}_{\delta,1}$ in the lowest reference plane Π_1 at $z = 0$ in Fig. 2.11. The integral curve of ξ_2 used for the selection of the remaining closed orbits $\gamma_{2,\dots,100}$ connects $(x \approx 3.64, y \approx 4.15, z = 0.0) \in \gamma_1$ and $(x \approx 3.32, y \approx 4.88, z \approx 6.22) \in \Pi_{100}$. The arclengths and δ-values of these orbits $\gamma_{1,\dots,100}$ constituting the LCS $\mathcal{M}_\Delta(t_0)$ are shown in Figs. 2.12a, 2.12b.

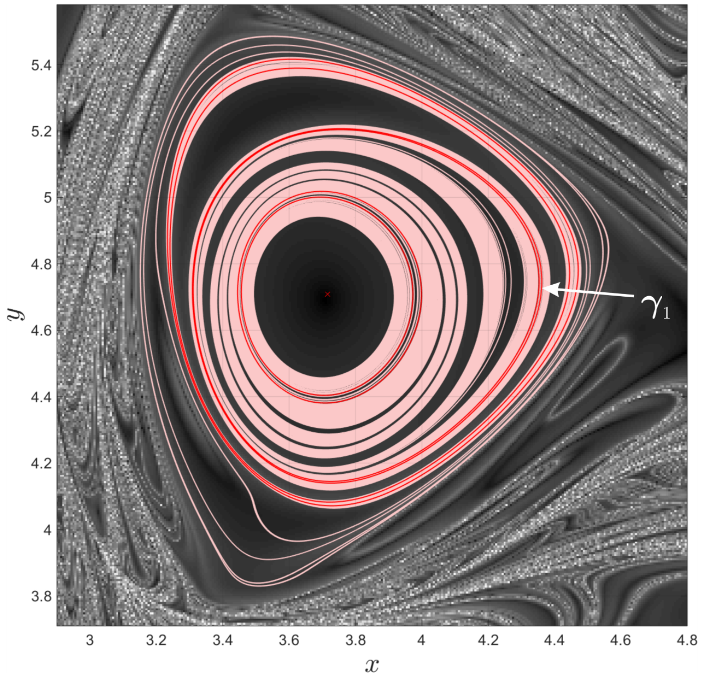

Fig. 2.11: Aperiodic ABC-type flow, time-window $[0, 40]$: Closed orbits of $\eta^{\pm}_{\delta,1}$ with $\delta \in [-0.2775, 0.3225]$ in the plane Π_1, displaying curves with $\delta = 0$ in strong red and with $\delta \neq 0$ in light red. The red cross indicates the approximate vortex center. The curve γ_1 is used as the initial orbit in the assembly of the elliptic LCS. Background visualization: Finite-time Lyapunov exponent field.

For $t_0 = 0$, we visualize this largest elliptic LCS $\mathcal{M}_\Delta(t_0)$ as the red surface in Fig. 2.13a, together with purple dots indicating a toroidal cloud of tracers placed closely around it. In comparison to the green surface $\mathcal{M}_\Delta(t)$ in Fig. 2.13b, we see that the elliptic LCS $\mathcal{M}_\Delta(\tau)$ does move under advection over $[0, 40]$, but keeps its coherence. The purple tracer cloud, on the other hand, starts to develop two filaments.

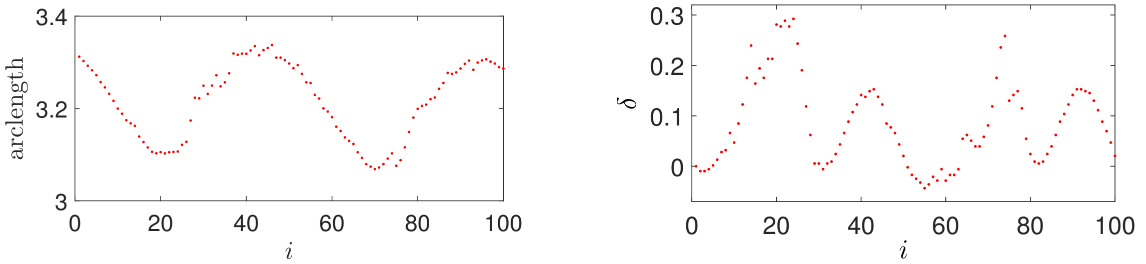

(a) Arclengths of the closed orbits γ_i selected on each reference plane.

(b) Values of δ of the closed orbits γ_i selected on each reference plane.

Fig. 2.12: Aperiodic ABC-type flow, time-window $[0, 40]$: Properties of the closed orbits $\gamma_{1,\ldots,100}$ used to build an elliptic LCS.

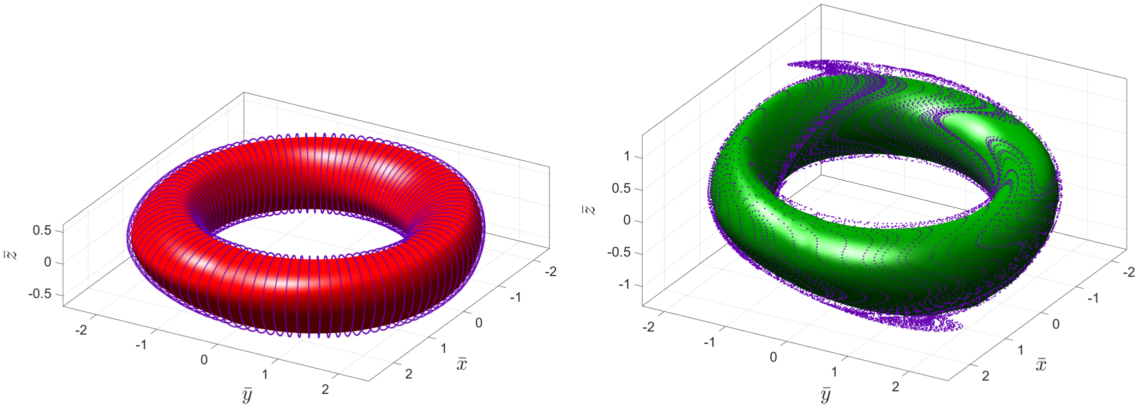

(a) Red: elliptic LCS $\mathcal{M}_{\Delta=0.1}(t_0 = 0)$, extracted for the time-interval $[0, 40]$. Purple: Locations of tracers placed closely outside the LCS surface.

(b) Green: time-40 advected image of the elliptic LCS in Fig. 2.13a, purple: Tracers advected from the locations in Fig. 2.13a.

Fig. 2.13: Aperiodic ABC-type flow, time-window $[0, 40]$: Advecting the elliptic LCS from $t_0 = 0$ to $t = 40$, in comparison to tracers.

Comparing Fig. 2.13b to Fig. 2.7b, we see that the steady ABC flow spreads tracers outside the elliptic LCS more than the time-aperiodic version. This phenomenon arises as follows: The LCS we obtain for the steady ABC flow is the outermost structure of a large family of nested tori that are going to advect coherently. Parts of the tracer cloud placed around the LCS are already in the chaotic region and undergo large stretching. Including time-aperiodic functions in the coefficients of the ABC flow, on the other hand, lets a large number of the outermost tori disappear. Consequently, the LCS we obtain in the aperiodic case is much smaller and far away from the hyperbolic structures. In comparison to the steady case, tracers initialized along the LCS we obtain in the time-aperiodic ABC type flow thus experience less dramatic stretching over the time interval considered here.

The vortices in the two ABC-type flows analyzed here have a simpler spatial structure than the ones analyzed in other works (e.g., [70]). Here our focus is to describe a new method and provide a proof of concept in a simpler setting. Analyzing a time-aperiodic version of the time-periodic flow considered in [70] would be a worthwhile application of the approach derived here.

2.7 Conclusions

We have extended the construction of elliptic LCSs as uniformly stretching material surfaces from the two-dimensional setting of [37] to three-dimensional unsteady flows. With this approach, we obtain near-uniformly stretching tubular material surfaces that do not filament under the flow. This is in contrast to the 3D elliptic LCS approach from [9], which imposes a strict point-wise maximum shear principle. For the steady ABC flow, we have shown that our elliptic LCS construction identifies invariant tori revealed also by the Poincaré map. In an aperiodically driven ABC-type flow, we have located temporally aperiodic non-filamenting tori. The two-dimensional version [37] of the present ideas has proven effective in locating material boundaries of Agulhas rings in the south Atlantic [37, 82], of the Great Red Spot of Jupiter [31], and of coherent Lagrangian vortices in the wake of swimming fish [42]. Our method offers a similar tool for locating coherent material vortex boundaries in three-dimensional numerical and experimental, highly resolved velocity data.

Recent work [38] has identified rotationally coherent (and not necessarily uniformly stretching) LCSs using the Lagrangian-Averaged Vorticity Deviation (LAVD). This approach, therefore, targets flows with non-vanishing vorticity. The present approach makes no such assumption, and hence is of general relevance for 3D dynamical systems that are not necessarily fluid flows.

Another recent approach identifies elliptic LCSs in two- and three-dimensional flows from tubular level sets of the polar rotation angle (PRA) [22]. The PRA measures the total rotation of the Cauchy-Green eigenbasis under the deformation gradient. The PRA is obtained from the polar decomposition of the deformation gradient into a rotation tensor and a right stretch tensor. The latter has the same eigenvalues and eigenvectors as the Cauchy-Green strain tensor and thus contains all the quantities needed to define the surfaces we use here (cf. Definition 2.2). Defining the PRA, on the other hand, requires the rotation tensor only. The PRA approach can hence be viewed as dual to the present method, and is applicable beyond fluid flows as well. In contrast to extracting near-uniformly stretching surfaces, however, identifying structures from PRA level sets is not an objective (frame-invariant) method in three-dimensional flows. The present approach overcomes this limitation.

We thank Alireza Hadjighasem and Daniel Karrasch for helpful discussions and suggestions.

2.A Details on solving (2.8) in the Proof of Theorem 2.1

We examine why the solution set of (2.8) in the case of $\lambda = \sqrt{\lambda_2}$ consists of two planes, while $\lambda = \sqrt{\lambda_3}$ and $\lambda = \sqrt{\lambda_1}$ yield lines.

For $\lambda = \sqrt{\lambda_2}$, (2.8) can be written as

$$\alpha^2(\lambda_2 - \lambda_1) + \gamma^2(\lambda_2 - \lambda_3) = 0. \tag{2.18}$$

Rearranging this equation, we obtain

$$\gamma = \mp\sqrt{\frac{\lambda_2 - \lambda_1}{\lambda_3 - \lambda_2}}\alpha.$$

The solution set of (2.8) for $\lambda = \sqrt{\lambda_2}$ is therefore given by two planes. (These planes are normal to the unit vectors $n^{\pm}$ defined in (2.9).)

For $\lambda = \sqrt{\lambda_3}$, (2.8) can be written as

$$\alpha^2(\lambda_3 - \lambda_1) + \beta^2(\lambda_3 - \lambda_2) = 0. \tag{2.19}$$

This equation is similar to (2.18), but, since both $(\lambda_3 - \lambda_1) > 0$ and $(\lambda_3 - \lambda_2) > 0$, the only solution of (2.19) is given by $\alpha = \beta = 0$, $\gamma \in \mathbb{R}$ (which is exactly the ξ_3-axis). For $\lambda = \sqrt{\lambda_1}$, we similarly conclude that the ξ_1-axis is the solution set of (2.8).

The reasoning leading to double cones for the remaining two cases of $\lambda \in (\lambda_1, \lambda_2)$ and $\lambda \in (\lambda_2, \lambda_3)$ will appear in Appendix 2.C. We hence omit it here for brevity.

2.B Repeated eigenvalues in the Proof of Theorem 2.1

Given the inital position $\mathcal{M}(t_0)$ of a pointwise uniformly stretching material surface $\mathcal{M}(\tau)$, we show that $\lambda(x_0) = \sqrt{\lambda_2(x_0)}$ holds for all points $x_0 \in \mathcal{M}(t_0)$ where the Cauchy-Green strain tensor has repeated eigenvalues:

- For any point $x_0 \in \mathcal{M}(t_0)$ where $\lambda_1(x_0) \neq \lambda_2(x_0) = \lambda_3(x_0)$, we may repeat the procedure as for points with distinct eigenvalues. For the expansion of $v \in T_{x_0}\mathcal{M}(t_0)$, pick any two orthogonal vectors $\tilde{\xi}_{2,3}$ in the plane normal to $\xi_1(x_0)$, and write $v = \alpha\xi_1 + \beta\tilde{\xi}_2 + \gamma\tilde{\xi}_3$. The λ-stretching condition is then identical to (2.8) with $\lambda_2 = \lambda_3$, that is

$$\alpha^2(\lambda^2 - \lambda_1) + (\beta^2 + \gamma^2)(\lambda^2 - \lambda_2) = 0. \tag{2.20}$$

  Here, three cases are possible: If $\lambda = \sqrt{\lambda_1}$, then the solution set of (2.20) is the ξ_1-axis (see Case 1 in Tab. 2.1). If $\lambda \in (\sqrt{\lambda_1}, \sqrt{\lambda_2})$ then the solution set of (2.20) is a circular double cone about the ξ_1-axis (see Case 2 in Tab. 2.1). If $\lambda = \sqrt{\lambda_2}$, then directions satisfying (2.20) form a plane perpendicular to ξ_1. (This corresponds to Case 3 in Tab. 2.1, with the two planes collapsed into one.) This implies that the tangent plane $T_{x_0}\mathcal{M}(t_0)$ is normal to $\xi_1(x_0)$. Vectors tangent to $\mathcal{M}(t_0)$ therefore stretch by $\lambda(x_0) = \sqrt{\lambda_2(x_0)} = \sqrt{\lambda_3(x_0)}$.

- For any point $x_0 \in \mathcal{M}(t_0)$ where $\lambda_1(x_0) = \lambda_2(x_0) \neq \lambda_3(x_0)$, repeating the argument from above shows that there exists a plane of uniformly stretching directions perpendicular to $\xi_3(x_0)$. With the tangent plane $T_{x_0}\mathcal{M}(t_0)$ therefore being perpendicular to $\xi_3(x_0)$, we conclude that all vectors from $T_{x_0}\mathcal{M}(t_0)$ stretch by $\lambda(x_0) = \sqrt{\lambda_1(x_0)} = \sqrt{\lambda_2(x_0)}$.

- For any point $x_0 \in \mathcal{M}(t_0)$ where $\lambda_1(x_0) = \lambda_2(x_0) = \lambda_3(x_0)$, the surface $\mathcal{M}(t_0)$ may be perpendicular to any unit normal $n(x_0) \in S^2$. All elements of its tangent space $T_{x_0}\mathcal{M}(t_0)$ then stretch by $\lambda(x_0) = \sqrt{\lambda_1(x_0)} = \sqrt{\lambda_2(x_0)} = \sqrt{\lambda_3(x_0)}$.

2.C Geometry of elliptic cones and planes

In order to motivate the expression for $n_\delta^\pm(x_0)$ given in (2.12), consider $\lambda^2(x_0) = \lambda_2(x_0)\,(1+\delta)$ with positive $\delta \in (0, -1 + \frac{\lambda_3(x_0)}{\lambda_2(x_0)})$ (Case 4 in Table 2.1), and examine the equation (2.8) of λ-stretching directions. After rearranging and again omitting the position arguments, we find

$$\frac{\alpha^2}{a^2} + \frac{\beta^2}{b^2} = 1, \tag{2.21}$$

where

$$a = \sqrt{\frac{\lambda_3 - \lambda_2(1+\delta)}{\lambda_2(1+\delta) - \lambda_1}\gamma^2}, \quad b = \sqrt{\frac{\lambda_3 - \lambda_2(1+\delta)}{\lambda_2\delta}\gamma^2}.$$

For any fixed γ, and recalling that α, β, γ are the coordinates along ξ_1, ξ_2, ξ_3, we recognize (2.21) as the equation of an ellipse with minor axis ξ_1 and major axis ξ_2. This explicitly shows that the λ-stretching directions form elliptic double cones about the ξ_3-axis (Table 2.1). Considering small δ, we have that $b \gg a$, confirming that these cones are indeed elongated along the ξ_2-axis. We therefore approximate these cones using the two planes shown in purple and orange in Fig. 2.14. Setting $\beta = 0$

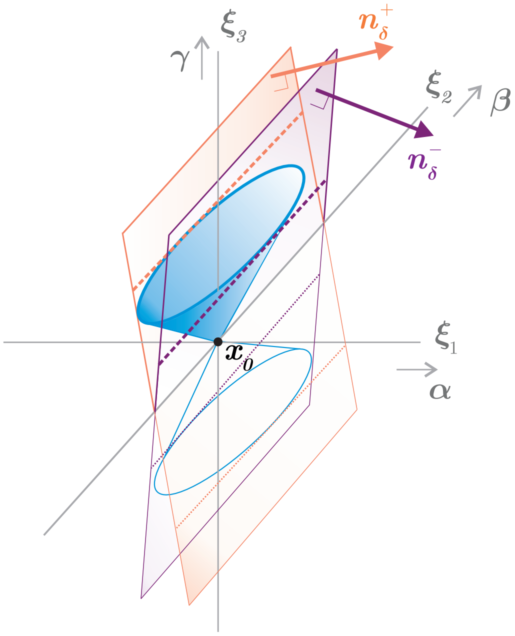

Fig. 2.14: Small $\delta > 0$: The elliptic double cones of λ-stretching directions can be approximated by a pair of planes.

in (2.21), we find that such cones satisfy

$$\gamma = \mp\sqrt{\frac{\lambda_2(1+\delta)-\lambda_1}{\lambda_3-\lambda_2(1+\delta)}}\alpha,$$

and hence the two planes are perpendicular to the unit vectors $n_\delta^\pm$ given in (2.12). We omit repeating the argument for $\delta < 0$.

2.D Angle preservation within uniformly stretching surfaces

As shown in Appendix 2.A, at any initial position x_0, a uniformly stretching surface $\mathcal{M}(t_0)$ will be perpendicular to one of the two possible unit normals

$$n_0^\pm(x_0) = n_{\delta=0}^\pm(x_0) = \sqrt{\frac{\lambda_2(x_0)-\lambda_1(x_0)}{\lambda_3(x_0)-\lambda_1(x_0)}}\xi_1(x_0) \pm \sqrt{\frac{\lambda_3(x_0)-\lambda_2(x_0)}{\lambda_3(x_0)-\lambda_1(x_0)}}\xi_3(x_0). \quad (2.22)$$

The tangent space $T_{x_0}\mathcal{M}(t_0)$ is therefore spanned by $\xi_2(x_0)$ and

$$\xi_0^{\pm}(x_0) := \pm\sqrt{\frac{\lambda_3(x_0)-\lambda_2(x_0)}{\lambda_3(x_0)-\lambda_1(x_0)}}\xi_1(x_0) - \sqrt{\frac{\lambda_2(x_0)-\lambda_1(x_0)}{\lambda_3(x_0)-\lambda_1(x_0)}}\xi_3(x_0). \tag{2.23}$$

With these definitions, we have $\xi_0^{\pm}(x_0) \times \xi_2(x_0) = n_0^{\pm}(x_0)$. Consider two arbitrary vectors $u, v \in T_{x_0}\mathcal{M}(t_0)$, see Fig. 2.15. We expand them in the orthonormal basis

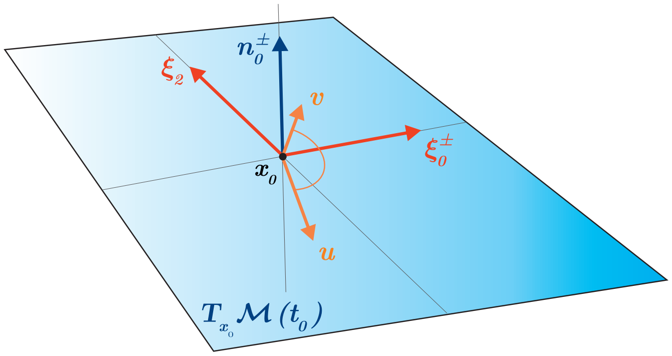

Fig. 2.15: Set-up to evaluate the change of angle between two arbitrary-vectors $u, v \in T_{x_0}\mathcal{M}(t_0)$ under advection by $DF_{t_0}^t$.

defined above, dropping the position label,

$$\begin{aligned} u &= u_0\xi_0^{\pm} + u_2\xi_2, \\ v &= v_0\xi_0^{\pm} + v_2\xi_2. \end{aligned}$$

By the singular-value decomposition of $DF_{t_0}^t$ (cf. [45]), one obtains that under advection from time t_0 to time t, the eigenvectors of $C_{t_0}^t$ are mapped according to

$$DF_{t_0}^t\xi_i = \sqrt{\lambda_i}\theta_i\,, \quad i = 1, 2, 3, \tag{2.24}$$

where $\theta_{1,2,3}$ are orthonormal eigenvectors of the left Cauchy-Green strain tensor $B_{t_0}^t = DF_{t_0}^t(DF_{t_0}^t)^T$. Applying these relations after fully writing out u and v in terms of the ξ_i-vectors, we obtain

$$\begin{aligned}\langle DF_{t_0}^t u,\, DF_{t_0}^t v\rangle &= \lambda_2(u_0 v_0 + u_2 v_2) \equiv \lambda_2\langle u,\, v\rangle,\\ \|DF_{t_0}^t u\| &= \sqrt{\lambda_2}\sqrt{(u_0)^2 + (u_2)^2} = \sqrt{\lambda_2}\,\|u\|,\\ \|DF_{t_0}^t v\| &= \sqrt{\lambda_2}\,\|v\|.\end{aligned}$$

Combining these expressions yields

$$\frac{\langle DF_{t_0}^t u,\, DF_{t_0}^t v\rangle}{\|DF_{t_0}^t u\| \cdot \|DF_{t_0}^t v\|} = \frac{\langle u,\, v\rangle}{\|u\| \cdot \|v\|}, \tag{2.25}$$

which means that, under advection from time t_0 to time t, the angle between u, v is indeed preserved.

2.E Proof of Proposition 2.1

Consider an arbitrary unit normal $n \in S^2$ and the plane Π_n perpendicular to it, $\Pi_n = \{v \in \mathbb{R}^3 | \langle v,\, n\rangle = 0\}$. We introduce an orthonormal basis ijk of $\mathbb{R}^3$ such that i and j lie in Π_n and $k := i \times j \equiv n$. We parametrize directions $\eta \in S^2 \cap \Pi_n$ by

$$\eta = \eta(\phi) = i\cos(\phi) + j\sin(\phi), \quad \phi \in [0, 2\pi). \tag{2.26}$$

The stretching within Π_n can then be mapped out by introducing a function

$$q_n(\phi) := \sqrt{\langle \eta(\phi), C_{t_0}^t\, \eta(\phi)\rangle}. \tag{2.27}$$

We evaluate this explicitly in terms of the Cauchy-Green invariants.

Lemma 2.1. *Using the above definitions, choosing*

$$\begin{cases} \langle i, \xi_2\rangle = 0, \quad \operatorname{sgn}(\langle i, \xi_1\rangle) = \operatorname{sgn}(n_3) & \textit{if } n \neq \pm\xi_2, \\ i = \xi_1, \quad j = -\xi_3 & \textit{if } n = \pm\xi_2, \end{cases}$$

and expanding $n = n_1\xi_1 + n_2\xi_2 + n_2\xi_3$, we find

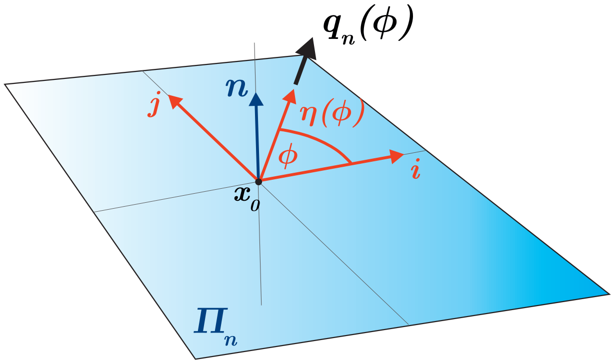

Fig. 2.16: Mapping out the stretching within Π_n, see also (2.26), (2.27).

$$q_n(\phi) = \begin{cases} \sqrt{\frac{\lambda_1(n_3\cos\phi - n_1 n_2 \sin\phi)^2 + \lambda_2(n_1^2+n_3^2)^2\sin^2\phi + \lambda_3(n_1\cos\phi + n_2 n_3\sin\phi)^2}{n_1^2+n_3^2}}, & \textit{if } n \neq \pm\xi_2, \\ \sqrt{\lambda_3 + (\lambda_1 - \lambda_3)\,\cos^2(\phi)}, & \textit{if } n = \pm\xi_2. \end{cases} \tag{2.28}$$

In particular,

$$q_{\pm n_\delta^\pm}(\phi) = \sqrt{\lambda_2(1+\delta\,\cos^2\phi)}, \tag{2.29}$$

$$q_{\pm\xi_1}(\phi) = \sqrt{\lambda_2 + (\lambda_3 - \lambda_2)\,\cos^2(\phi)}, \tag{2.30}$$

$$q_{\pm\xi_3}(\phi) = \sqrt{\lambda_2 + (\lambda_1 - \lambda_2)\,\cos^2(\phi)}. \tag{2.31}$$

Proof. If $n \neq \pm\xi_2$, writing out the equations $\langle i, n\rangle = 0$ and $\langle i, \xi_2\rangle = 0$ while requiring $i \in S^2$ allows two coordinate expressions for i with opposite orientation, from which we pick

$$i = \frac{n_3}{\sqrt{n_1^2+n_3^2}}\xi_1 - \frac{n_1}{\sqrt{n_1^2+n_3^2}}\xi_3.$$

From $j = k \times i = n \times i$ we get that

$$j = -\frac{n_1 n_2}{\sqrt{n_1^2+n_3^2}}\xi_1 + \sqrt{n_1^2+n_3^2}\,\xi_2 - \frac{n_2 n_3}{\sqrt{n_1^2+n_3^2}}\xi_3.$$

Plugging these expressions into (2.26) and then (2.27) yields the first equation in (2.28). □

Proof. [of Proposition 2.1] For any given λ, first consider $n = \pm n_\delta^\pm$ with $\delta = \lambda^2/\lambda_2 - 1$. Equation (2.29) shows that the range of stretching values attained in $\Pi_{\pm n_\delta^\pm}$ is the interval

$$[\min\{\lambda, \sqrt{\lambda_2}\}, \max\{\lambda, \sqrt{\lambda_2}\}]\,. \tag{2.32}$$

We compare this to what an arbitrary $n \in S^2$ can provide for any prescribed λ: If $\lambda > \lambda_2$, consider that $\Pi_n \cap \Pi_{\xi_3} \neq \emptyset$ always holds, and thus by Eq. (2.31) there exists a ϕ_0 such that $q_n(\phi_0) \in [\sqrt{\lambda_1}, \sqrt{\lambda_2}]$. The smallest range of stretching values within Π_n that one could possibly obtain is therefore $[\sqrt{\lambda_2}, \lambda]$. But this is exactly what we have already achieved above by taking $n = \pm n_\delta^\pm$, see (2.32), rendering it the optimal choice. If $\lambda < \sqrt{\lambda_2}$, repeat the argument considering $\Pi_n \cap \Pi_{\xi_1} \neq \emptyset$, which by Eq. (2.30) means that there exists a ϕ_0 such that $q_n(\phi_0) \in [\sqrt{\lambda_2}, \sqrt{\lambda_3}]$, and therefore the smallest possible range is $[\lambda, \sqrt{\lambda_2}]$. This can again be achieved with $n = \pm n_\delta^\pm$. □

2.F Connection between surfaces tangent to ξ_2 and the $n_\delta^\pm$ fields

We consider an arbitrary smooth surface tangent to ξ_2, and relate its normal field to the normal fields $\pm n_\delta^\pm$ (see (2.12), taking into account orientation here).

Lemma 2.2. *Consider a surface $\mathcal{S}(t_0)$ that is normal to the vector field*

$$m_\phi = \cos\phi\,\xi_1 + \sin\phi\,\xi_3, \tag{2.33}$$

with $\phi : x_0 \mapsto \phi(x_0) \in [0, 2\pi)$ denoting a scalar field on $\mathcal{S}(t_0)$. Then for each $x_0 \in \mathcal{S}(t_0)$, there exists an injective function F from ϕ to $(\delta, \sigma_1, \sigma_2)$, the parameters of the vector field $n_\delta^{\sigma_1,\sigma_2}$. Here $n_\delta^{\sigma_1,\sigma_2}$ is related to $n_\delta^\pm$ (2.12) via $n_\delta^{\sigma_1,\sigma_2} = \sigma_2 n_\delta^{\sigma_1}$, i.e., we define

$$n_\delta^{\sigma_1,\sigma_2} = \sigma_2(a_\delta\xi_1 + \sigma_1 c_\delta \xi_3), \quad a_\delta = \sqrt{\frac{\lambda_2\,(1+\delta) - \lambda_1}{\lambda_3 - \lambda_1}}, \quad c_\delta = \sqrt{\frac{\lambda_3 - \lambda_2\,(1+\delta)}{\lambda_3 - \lambda_1}}, \quad \sigma_{1,2} \in \{-1, 1\}.$$

Proof. Solving either $a_\delta = \cos\phi$ or $c_\delta = \sin\phi$ for δ yields

$$\delta = f(\phi) := \frac{\lambda_1 - \lambda_2 + (\lambda_3 - \lambda_1)\cos^2\phi}{\lambda_2}.$$

We thus define the function F as

$$F : \begin{cases} [0,\pi) & \rightarrow \left[-1+\frac{\lambda_1}{\lambda_2}, -1+\frac{\lambda_3}{\lambda_2}\right] \times \{-1,1\} \times \{-1,1\}\,, \\ \phi & \mapsto (F_0(\phi), F_1(\phi), F_2(\phi)) := \begin{cases} (f(\phi),1,1)\,, & \text{if } \phi \in [0,\pi/2)\,, \\ (f(\phi),-1,1) & \text{if } \phi \in [\pi/2,\pi)\,, \\ (f(\phi),1,-1) & \text{if } \phi \in [\pi,3\pi/2)\,, \\ (f(\phi),-1,-1) & \text{if } \phi \in [3\pi/2,2\pi)\,. \end{cases} \end{cases}$$

□

Now consider an arbitrary smooth surface $\mathcal{S}(t_0)$ tangent to ξ_2. Since $\mathcal{S}(t_0)$ does not contain points where $C_{t_0}^t$ has repeated eigenvalues, locally, the direction fields ξ_1 and ξ_3 can be oriented into smooth vector fields. The normal field of $\mathcal{S}(t_0)$ is therefore given by a smooth vector field m_ϕ of the form (2.33). Allowing $\delta \in \left[-1+\frac{\lambda_1}{\lambda_2}, -1+\frac{\lambda_3}{\lambda_2}\right]$ to vary in space, we choose $(\delta, \sigma_1, \sigma_2) = (F_0(\phi), F_1(\phi), F_2(\phi))$, and identify

$$m_\phi = n_{F_0(\phi)}^{F_1(\phi),F_2(\phi)} = n_\delta^{\sigma_1,\sigma_2} = \sigma_2 n_\delta^{\sigma_1}.$$

The surface $\mathcal{S}(t_0)$ therefore satisfies the helicity condition

$$\langle \nabla \times m_\phi, m_\phi \rangle = \langle \nabla \times n_\delta^{\sigma_1}, n_\delta^{\sigma_1} \rangle = 0.$$

2.G Detailed summary of the extraction procedure

Here we summarize the numerical extraction procedure for elliptic LCSs, $\mathcal{M}_\Delta(t_0)$, in detail:

Part 1: Using a parallel stack of square grids, each of them corresponding to one reference plane Π_i, define a 3D main grid in the flow domain. For each reference plane Π_i, compute closed orbits of $\eta^{\pm}_{\delta,i}$. The steps listed below are similar to the procedure for (elliptic) LCS computations in two dimensions [20, 37]:

1. Compute an approximation to the Cauchy-Green strain tensor $C^t_{t_0}$: Along each of the three coordinate axes defined by the 3D Cartesian grid, place two particles with displacements $-d$ and $+d$ relative to each main grid point of the current reference plane. Obtain their flow maps by integration of the velocity field. Using finite-differencing [36], approximate $DF^t_{t_0}$ and thus $C^t_{t_0}$.

2. Use an eigensolver to compute the Cauchy-Green invariants $\xi_{1,2,3}$ and $\lambda_{1,2,3}$ on each main grid point.

3. Using bilinear interpolation for $\lambda_{1,2,3}$ and the components of $\xi_{1,2,3}$, compute closed integral curves of $\eta^{\sigma}_{\delta,i}$, looping over both $\sigma = +,-$ and $\delta \in [-2\Delta + \Delta^2, 2\Delta + \Delta^2]$. This is easiest to do using a one-dimensional Poincaré section within Π_i as a secondary one-dimensional grid of initial conditions for candidate orbits of $\eta^{\sigma}_{\delta,i}$. We then detect closed orbits of $\eta^{\sigma}_{\delta,i}$ from changes in the spiralling behaviour of the candidate orbits, refining the result by the bisection method.

Part 2: Select closed orbits $\{\gamma_i\}$ and interpolate to obtain an elliptic LCS surface $\mathcal{M}_{\Delta}(t_0)$:

1. Consider the first reference plane Π_{i_0} containing at least one closed orbit of $\eta^{\pm}_{\delta=0,i_0}$ in the region of interest. For the purpose of visualizing the vortex boundary, we pick the outermost closed orbit, which we refer to as as γ_{i_0}.

2. Construct (parts of) $\mathcal{S}(t_0)$: Starting from points on γ_{i_0}, integrate curves tangent to the ξ_2-line field (ξ_2-lines) until each reference plane containing closed orbits of $\eta^{\pm}_{\delta,i}$ is intersected at least once. When integrating ξ_2-lines, for each integration step, we recompute ξ_2 by placing 6 particles at distances $\pm d$ from the current point of the trajectory (see Part 1, Steps 1 and 2).

3. In the following reference plane Π_{i_0+1}, select the closed orbit of $\eta^{\pm}_{\delta,i_0+1}$, labeled γ_{i_0+1}, closest to the intersection points between Π_{i_0+1} and the ξ_2-line(s) (in the sense described in Sec. 2.5.2).

4. Keep repeating Step 3, going through all reference planes that contain closed orbits of $\eta^{\pm}_{\delta,i}$. At the end, use the data points given by the collection of closed orbits $\{\gamma_i\}$ of the $\eta^{\pm}_{\delta,i}$ -fields to interpolate a smooth surface $\mathcal{M}_{\Delta}(t_0)$. If this is not possible, go back to Π_{i_0} and repeat the selection procedure from another available closed orbit of $\eta^{\pm}_{\delta=0,i_0}$.

For both the steady and the time-aperiodic ABC-type flow analyzed here (cf. Sec. 2.6), the elliptic LCS traverses the entire flow domain along the z-direction, and we find closed orbits of $\eta^{\pm}_{\delta,i}$ on all the reference planes Π_i. The extraction algorithm listed here can, however, handle the more generic case. That is, if the LCS does not span across the whole flow domain, our procedure terminates and produces a shorter LCS: By the end of *Part 1*, for all the reference planes $\Pi_{i=1,2,3,\ldots}$, we have computed a collection of closed orbits of the $\eta^{\pm}_{\delta,i}$ vector fields. Assume that for some index i^*, no nearby closed orbit of the vector field $\eta^{\pm}_{\delta,i^*}$ in the plane Π_{i^*} is available. This prevents us from carrying out Step 3 of *Part 2* for i^*, and hence our LCS construction procedure terminates.

Overall, the method described here is computationally costly. It is therefore not suitable for running quick diagnostics, but designed to yield results at a very high level of detail. The computational cost is, however, not vastly greater than the cost of computing the FTLE field (*Part 1*, Step 2): The extra effort is mostly required by the handling of the data produced by the algorithm, rather than by the additional computational steps.

2.H Numerical details for the examples

The numerical settings listed here apply to all three examples: the steady ABC flow over $[t_0, t] = [0, 40]$ and $[0, 250]$, and the time-aperiodic ABC-type flow over $[0, 40]$.

For the computation of $C_{t_0}^t$, in each reference plane Π_i, we define a square main grid of 1000×1000 points and place initial conditions with relative spacing $d = 10^{-5}$. For searching closed orbits of $\eta_{\delta,i}^{\pm}$, in each plane Π_i, we use a Poincaré section parallel to the x-axis at $y = 4.73$, and place initial conditions for $\eta_{\delta,i}^{\pm}$-orbits at a uniform spacing $\Delta x = 0.002$. We allow for up to 10 bisection iterations, with an absolute error bound of 10^{-4}. All ODE integrations are performed by a Runge-Kutta (4,5) method [17] combined with an adaptive stepper whose absolute and relative error tolerances we set to 10^{-8}.

For the steady ABC flow analyzed over $[0, 40]$, we obtain 591 closed orbits of $\eta_{\delta,1}^{\pm}$ in Π_1. We identify these closed orbits of $\eta_{\delta,1}^{\pm}$ (cf. Fig. 2.5) by their intersection points with the Poincaré section at $y = 4.73$, and plot their δ-values in Fig. 2.17. In our scans of the remaining reference planes $\Pi_2, ..., \Pi_{100}$, we find between 547 and 775 closed orbits.

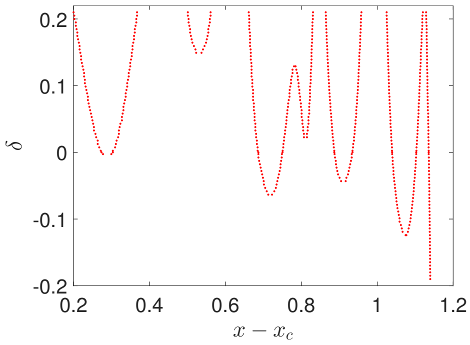

Fig. 2.17: Steady ABC flow analyzed over $[t_0, t] = [0, 40]$: Values of δ for the closed orbits of $\eta_{\delta,1}^{\pm}$ shown in Fig. 2.5, plotted over the x-coordinate of their intersections with the Poincaré section $(x - x_c, 4.73, 0.0)$, where $x_c = 3.73$.

Chapter 3

An Autonomous Dynamical System Captures all LCSs in Three-Dimensional Unsteady Flows

3.1 Introduction

Lagrangian coherent structures (LCSs, [36]) are exceptional surfaces of trajectories that shape tracer patterns in unsteady flows over finite time intervals of interest. By their sustained coherence, LCSs are observed as barriers to transport. In autonomous or time-periodic dynamical systems, classic codimension-one invariant manifolds play a similar role (e.g., Komolgorov-Arnold-Moser (KAM) tori [6]). In the time-aperiodic and finite-time setting, this role is taken over by LCSs as codimension-one invariant manifolds (*material surfaces*) in the *extended* phase space.

Material surfaces are abundant, yet most impose no observable coherence. LCSs are distinguished material surfaces that have exceptional impact on nearby material surfaces. Since various distinct mechanisms producing such impact are known [36], no unique mathematical approach has been available to locate all the LCSs in a given flow. Instead, separate mathematical methods and computational algorithms exist for the three main LCS types: hyperbolic LCSs as generalizations of stable and unstable manifolds [35, 9]; elliptic LCSs as generalizations of invariant tori [37, 9, 64]; and, in two dimensions, parabolic LCSs as generalized jet cores [19].

Several works [35, 37, 19, 9, 64] have implemented properties that distinguish LCSs from generic material surfaces by requiring the LCSs to yield a critical value for a relevant quantity of material deformation. The criticality requirement defining, for instance, repelling hyperbolic LCSs (generalized stable manifolds) is that these material surfaces exert locally strongest repulsion [9]. Elliptic LCSs in two dimensions, on the other hand, can be obtained as stationary curves of an averaged stretching functional [37]. For the remaining LCS types in two and three dimensions, similar variational theories are available [35, 19, 9, 64].

All the variational LCS theories [35, 37, 19, 9, 64] provide particular direction fields to which initial LCS positions must be either tangent (in two dimensions) or normal (in three dimensions). Later LCS positions can then be constructed by forward or backward advection under the flow map.

In two dimensions, LCSs are simply material curves [36, 37, 19]. Initial LCS positions can thus be identified by computing integral curves of (time-independent) direction fields defined in the two-dimensional phase space. Obtaining initial-time LCS surfaces in three dimensions [9, 64], on the other hand, is significantly more complicated: One has to construct entire surfaces perpendicular to a given three-dimensional direction field. The presently available approach to extracting these surfaces is to sample the flow domain using two-dimensional reference planes, and then, within each plane, integrate direction fields that are perpendicular to the imposed LCS normal field. This procedure typically yields a high number of integral curves, which are candidates for intersection curves between unknown LCSs and the respective slice of the flow domain. As a second step, from this large collection of candidate curves, one has to identify smaller families of curves that can be interpolated into surfaces. Moreover, since the normal fields depend on the type of LCS, one has to repeat this complicated analysis for each LCS type [9, 64].

Here we observe that initial positions of all available variational LCSs in three dimensions share a common tangent vector field: the intermediate eigenvector field,

$\xi_2(x_0)$, of the right Cauchy-Green strain tensor. This allows us to seek all LCSs in three dimensions as invariant manifolds of the autonomous dynamical system generated by the ξ_2-field. The evolution of the ξ_2-system takes place in the initial configuration of the underlying non-autonomous system, but contains averaged information about the non-autonomous flow. The autonomous ξ_2-system is hence dual to the original unsteady flow. Equivalently, LCS final positions are invariant manifolds of the intermediate eigenvector field, $\eta_2(x_1)$, of the left Cauchy-Green strain tensor.

Instead of identifying LCSs in three dimensions from various two-dimensional direction fields [9, 64], we therefore need to consider only a single three-dimensional direction field. We then locate LCSs by familiar numerical methods developed for autonomous dynamical systems.

3.2 Set-up for Lagrangian coherent structures in 3D

Here we briefly review the mathematical foundations for Lagrangian coherent structures in three dimensions [36]. We consider ordinary differential equations of the form

$$\dot{x} = u(x,t), \quad x \in U, \quad t \in I, \tag{3.1}$$

where U is a domain in the Euclidean space $\mathbb{R}^3$; I is a time interval; u is a smooth mapping from the extended phase space $U \times I$ to $\mathbb{R}^3$. The setting in (3.1) includes time-aperiodic, non-autonomous dynamical systems for which asymptotic limits are undefined.

We consider a finite time interval $[t_0, t_1] \subset I$ and denote a trajectory of (3.1) passing through a point x_0 at time t_0 by $x(t; t_0, x_0)$. For points x_0 where the trajectory $x(t; t_0, x_0)$ is defined for all times $t \in [t_0, t_1]$, we introduce the flow map $F_{t_0}^t(x_0) := x(t;\, t_0,\, x_0)$. Denoting the support of $F_{t_0}^t$ by D, the flow map is a diffeomorphism onto its image $F_{t_0}^t(D)$. Hence the inverse $\left(F_{t_0}^t\right)^{-1}$ exists, and, in particular, $\left(F_{t_0}^t\right)^{-1} = F_t^{t_0}$.

Definition 3.1 (Material surface). Consider a set of initial positions forming a two-dimensional surface $\mathcal{M}(t_0)$ at time t_0 in U. Its time-t image, $\mathcal{M}(t)$, is obtained under the flow map as

$$\mathcal{M}(t) = F_{t_0}^{t}(\mathcal{M}(t_0)). \tag{3.2}$$

The union of all time-t images, $\cup_{t\in[t_0,t_1]}\mathcal{M}(t)$, is a hypersurface in the extended phase space $U \times I$, called a *material surface*. Unless we consider a specific time-t^* image $\mathcal{M}(t^*)$ by fixing time to a certain value $t^* \in [t_0, t_1]$, we refer to the entire material surface simply by the notation $\mathcal{M}(t)$.

Any material surface is an invariant manifold in the extended phase space $U \times I$ and, hence, cannot be crossed by integral curves $(x(t; t_0, x_0), t)$. Only special material surfaces, however, create coherence in the phase space U and hence act as observable transport barriers. Such material surfaces are generally called *Lagrangian coherent structures* (LCSs).

Quantifying material coherence in a general non-autonomous system requires considering (3.1) for a fixed time interval $[t_0, t_1]$. This reflects the observation that coherent structures in truly unsteady flows are generally transient. (See also [36].) Accordingly, any LCS is defined with respect to the fixed time interval $[t_0, t_1]$. (Thus, in applications where multiple time intervals $[t_0, t_1]$ are relevant, the LCSs need to be determined separately for each time interval.)

Viewed in the phase space U, LCSs are time-dependent surfaces, even if the underlying dynamical system (3.1) is autonomous. LCS positions at different times are related via (3.2).

In applications, even if the flow map $F_{t_0}^{t}$ is available for all $t \in [t_0, t_1]$, it remains challenging to detect and parametrize all the a priori unknown LCSs. This, fortunately, need not be done in the extended phase space: Since the flow map applied to any LCS position $\mathcal{M}(t^*)$ uniquely generates any required time-t image $\mathcal{M}(t)$, we can fix the time t^* to an arbitrary value in $[t_0, t_1]$ and parametrize $\mathcal{M}(t^*)$ in the phase space U. For simplicity, we generally choose $t^* = t_0$. (For attracting hyperbolic LCSs, however, it is advantageous to parametrize $\mathcal{M}(t_1)$ instead of $\mathcal{M}(t_0)$, see Sec. 3.5.3.). The difficulty remains in that almost any conceivable surface from the domain D

evolves incoherently under the flow, and hence does not define an LCS $\mathcal{M}(t)$ (cf. Fig. 1). We therefore need additional properties that, for any time-aperiodic flow, distinguish LCSs from generic material surfaces.

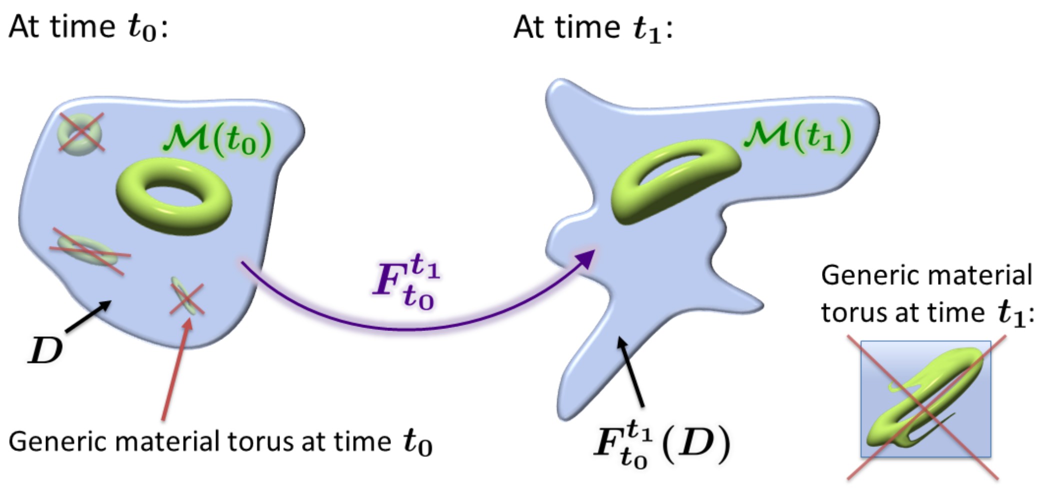

Fig. 3.1: Schematic of an elliptic LCS $\mathcal{M}(t)$, obtained as a toroidal surface $\mathcal{M}(t_0)$ in the flow domain D at time t_0. Up to rotations and translations, the time-t_1 image, $\mathcal{M}(t_1)$, is only moderately deformed relative to $\mathcal{M}(t_0)$ and does not display additional features, such as filaments. (In the context of fluid dynamics, such an LCS could capture a coherently evolving vortex ring in a three-dimensional unsteady flow.) Generic tori in D, on the other hand, are expected to evolve incoherently under the flow $F_{t_0}^{t_1}$ and thus do not yield LCSs.

3.3 Review of variational approaches to Lagrangian coherent structures in 3D

Within the general class of three-dimensional flows with arbitrary time dependence (3.1), several types of material surfaces can be viewed as coherently evolving. Each of them defines a distinct type of LCS. Three LCS types have so far been identified: hyperbolic repelling and attracting LCSs (generalized stable and unstable manifolds) [9], and elliptic LCSs (generalized invariant tori or invariant tubes) [9, 64].

Hyperbolic LCSs are locally most repelling or attracting material surfaces [9]. To express this property mathematically, we introduce the normal repulsion ρ of a material surface $\mathcal{M}(t)$ between times t_0 and t_1 (cf. Fig. 3.2). Specifically, at an

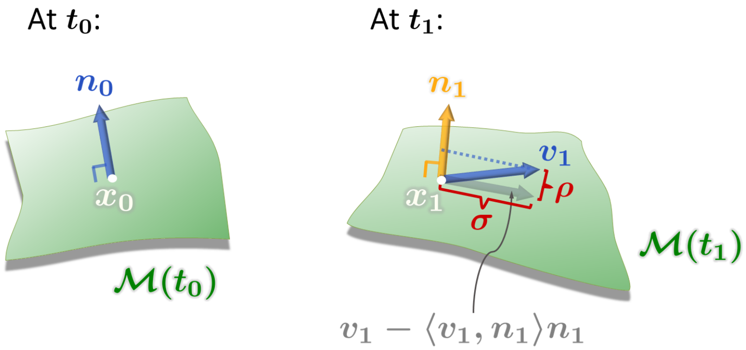

Fig. 3.2: Definitions of normal repulsion ρ, cf. (3.3), and the tangential shear σ, cf. (3.4).

arbitrary point x_0 in $\mathcal{M}(t_0)$, we consider a unit surface normal $n_0(x_0)$: Mapping $n_0(x_0)$ under the linearized flow $DF_{t_0}^{t_1}(x_0)$ from t_0 to t_1 yields a vector $v_1(x_1) = DF_{t_0}^{t_1}(x_0)n_0(x_0)$, where $x_1 = F_{t_0}^{t_1}(x_0)$ is a point in $\mathcal{M}(t_1)$. The vector $v_1(x_1)$ will generally neither be of unit length nor perpendicular to the surface $\mathcal{M}(t_1)$. Denoting the unit normal of $\mathcal{M}(t_1)$ at x_1 by $n_1(x_1)$, we introduce the normal repulsion ρ as

$$\rho = || \langle v_1, n_1 \rangle n_1 || = \langle v_1, n_1 \rangle , \tag{3.3}$$

where $\langle ., . \rangle$ is the Euclidean scalar product, and $||.||$ is the Euclidean norm. A large value of ρ means that the component of $v_1(x_1)$ normal to the surface $\mathcal{M}(t_1)$ is large and, thus, material elements that were initially aligned with $n_0(x_0)$ appear repelled from $\mathcal{M}(t_1)$. Similarly, if the normal component of $v_1(x_1)$ is small, then the components of $v_1(x_1)$ tangent to $\mathcal{M}(t_1)$ must be large, corresponding to attraction of material elements aligned with $n_0(x_0)$ to the surface $\mathcal{M}(t_1)$. Formally, we consider the normal repulsion as a function of the initial position x_0 and the surface normal $n_0(x_0)$, i.e., $\rho = \rho(x_0, n_0)$. With this convention, $\mathcal{M}(t_0)$ determines ρ. We now use ρ to define hyperbolic LCSs as most repelling or attracting material surfaces:

Definition 3.2 (Repelling and attracting hyperbolic LCS [9]). A smooth material surface $\mathcal{M}(t)$ is a *repelling (or attracting) hyperbolic LCS* if the unit normals $n_0(.)$ of $\mathcal{M}(t_0)$ maximize (or minimize) the normal repulsion function ρ among all perturbations $n_0(.) \mapsto \tilde{n}_0(.)$, with $\tilde{n}_0 : \mathcal{M}(t_0) \to S^2$ denoting an arbitrary unit vector field.

We additionally require $\rho > 1$ ($\rho < 1$) for repelling (attracting) hyperbolic LCSs, which is automatically satisfied for incompressible flows.

Motivated by KAM tori and coherent vortex rings in fluid flows, we require elliptic LCSs to be tubular surfaces in the phase space. By a tubular surface, we mean a smooth surface that is diffeomorphic to a torus, cylinder, sphere or paraboloid. In order to capture the most influential tubular surfaces, Fig. 3.2 suggests considering elliptic LCSs as surfaces maximizing the tangential shear σ under perturbations to the surface normal [9]. This Lagrangian shear σ is defined as

$$\sigma = ||v_1 - \langle v_1, n_1 \rangle\, n_1|| = ||v_1 - \rho\, n_1|| \tag{3.4}$$

(cf. Fig. 3.2). We consider the tangential shear σ as a function of the initial position x_0 and the surface normal $n_0(x_0)$, i.e., we write $\sigma = \sigma(x_0, n_0)$.

Definition 3.3 (Shear-maximizing elliptic LCS [9]). A tubular material surface $\mathcal{M}(t)$ is an *elliptic LCS* if the unit normals $n_0(.)$ of $\mathcal{M}(t_0)$ maximize the tangential shear function σ among all perturbations $n_0(.) \mapsto \tilde{n}_0(.)$, with $\tilde{n}_0 : \mathcal{M}(t_0) \to S^2$ denoting an arbitrary unit vector field.

As pointed out in [64], due to ever-present numerical inaccuracies, it is difficult to construct entire tubular surfaces that satisfy the strict requirement of pointwise maximal shear. A less restrictive definition of elliptic LCSs has been obtained recently by considering material surfaces $\mathcal{M}(t)$ that stretch nearly uniformly under the flow [64]. Considering any point x_0 in $\mathcal{M}(t_0)$, the linearized flow $DF_{t_0}^{t_1}$ maps any vector $e_0(x_0)$ from the tangent space $T_{x_0}\mathcal{M}(t_0)$ to a vector $e_1(x_1)$ in $T_{x_1}\mathcal{M}(t_1)$, where $x_1 = F_{t_0}^{t_1}(x_0)$. We define $\mathcal{M}(t)$ as *nearly uniformly stretching* at x_0 if all tangent vectors $e_0(x_0)$ satisfy

$$||e_1(x_1)|| = \lambda(x_0) \cdot ||e_0(x_0)|| \quad \text{with} \quad \lambda(x_0) \in [\sigma_2(x_0) \cdot (1 - \Delta), \sigma_2(x_0) \cdot (1 + \Delta)], \tag{3.5}$$

where $\sigma_2(x_0)$ is the intermediate singular value of $DF_{t_0}^{t_1}(x_0)$ (introduced below, cf.

(3.6)); and Δ is a small stretching deviation ($0 \leq \Delta \ll 1$). As shown in [64], setting $\lambda(x_0) = \sigma_2(x_0)$ (i.e., $\Delta = 0$) is the only way to obtain a material surface that is exactly uniformly stretching at x_0 (cf. Fig. 3.3).

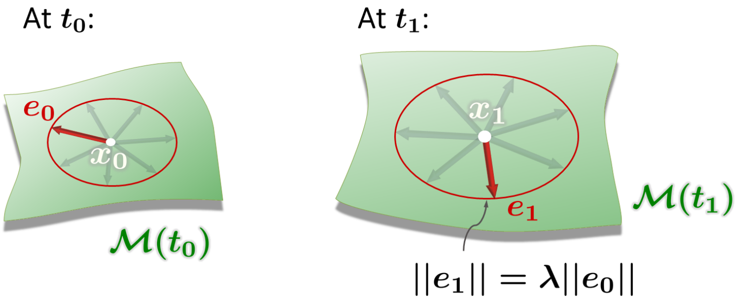

Fig. 3.3: Local deformation of a pointwise uniformly stretching surface (cf. (3.5)): All tangent vectors based at x_0 stretch exactly by the same factor of $\lambda(x_0)$ between times t_0 and t_1.

Definition 3.4 (**Near-uniformly stretching elliptic LCS [64]**)**.** A tubular material surface $\mathcal{M}(t)$ is an *elliptic LCS* if it is *nearly uniformly stretching* at any point in $\mathcal{M}(t_0)$.

Remark 3.1. In [64], the stretching deviation Δ is chosen to be constant on $\mathcal{M}(t_0)$. We could, however, let Δ vary on $\mathcal{M}(t_0)$ and still obtain valid elliptic LCSs (as long as $0 \leq \Delta \ll 1$). Requiring exact uniform stretching ($\Delta = 0$) would be similarly restrictive as requiring maximal tangential shear (cf. Definition 3.3).

Remark 3.2. Since $\sigma_2(x_0)$ is given by the problem and generally not a constant function, the factor $\lambda = \lambda(x_0)$ varies within the surface $\mathcal{M}(t_0)$ even when $\Delta = 0$. In two dimensions, however, it is possible to construct elliptic LCSs that stretch by a factor λ that is constant on $\mathcal{M}(t_0)$ [37].

Remark 3.3. Other types of distinguished material surfaces revealing elliptic LCSs are level sets of the polar rotation angle [22] and level sets of the Lagrangian-averaged vorticity [38]. These approaches are based on the notion of rotational coherence rather than stretching, and are hence not directly related to the variational approaches we review here.

From the linearization of the flow map $F_{t_0}^{t_1}$, we can derive explicit geometric conditions for both hyperbolic and elliptic LCSs (Definitions 3.2–3.4). These conditions are expressible in terms of eigenvectors and eigenvalues of the left and right Cauchy-Green strain tensors (cf. Remark 3.4 below). A fully equivalent, yet simpler picture is provided by the singular-value decomposition (SVD) of the the linearized flow map $DF_{t_0}^{t_1}(x_0)$: The linearized flow map $DF_{t_0}^{t_1}(x_0)$ (also called deformation gradient) maps vectors from the tangent space at x_0 onto their time-t_1 images in the tangent space at the point $x_1 = F_{t_0}^{t_1}(x_0)$. (Since the flow domain U is in the Euclidean space $\mathbb{R}^3$, each of these tangent spaces is simply $\mathbb{R}^3$ as well.) In particular, $DF_{t_0}^{t_1}(x_0)$ maps its three right-singular vectors $\xi_{1,2,3}(x_0)$ onto its three left-singular vectors $\eta_{1,2,3}(x_1)$, i.e.,

$$DF_{t_0}^{t_1}(x_0)\xi_i(x_0) = \sigma_i(x_0) \cdot \eta_i(x_1), \qquad i = 1, 2, 3, \tag{3.6}$$

see Fig. 3.4 and [80]. The singular vectors $\xi_{1,2,3}(x_0)$ and the $\eta_{1,2,3}(x_1)$ are unit vectors.

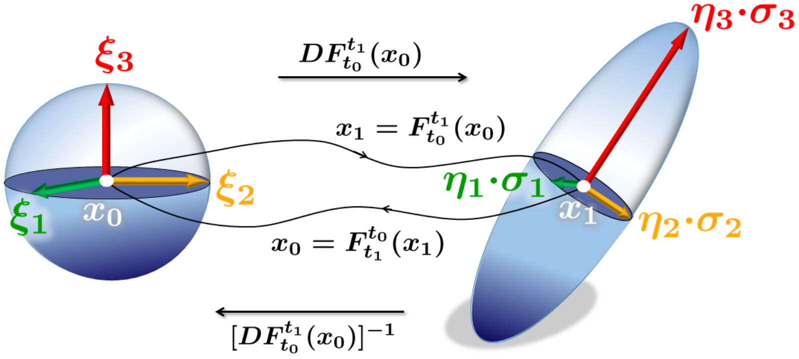

Fig. 3.4: The deformation gradient $DF_{t_0}^{t_1}$ mapping its right-singular vectors $\xi_{1,2,3}$ onto its left-singular vectors $\eta_{1,2,3}$.

Both the $\xi_{1,2,3}(x_0)$ and the $\eta_{1,2,3}(x_1)$ define an orthonormal basis of $\mathbb{R}^3$. The stretch factors $\sigma_{1,2,3}(x_0)$ in (3.6) are the singular values of $DF_{t_0}^{t_1}(x_0)$, which we assume to be distinct and ordered so that

$$0 < \sigma_1(x_0) < \sigma_2(x_0) < \sigma_3(x_0). \tag{3.7}$$

The available LCS definitions [9, 64] do not consider points where two singular values are equal.

We illustrate the kinematic role of the right-singular vectors $\xi_{1,2,3}(x_0)$ by considering the stretch factor of a vector $v(x_0)$, defined as

$$\Lambda_{t_0}^{t_1}(x_0, v(x_0)) = \frac{\left\| DF_{t_0}^{t_1}(x_0)\, v(x_0) \right\|}{||v(x_0)||}. \tag{3.8}$$

Since $\sigma_1(x_0) < \sigma_2(x_0) < \sigma_3(x_0)$, any vector $v(x_0)$ parallel to $\xi_3(x_0)$ maximizes the stretch factor $\Lambda_{t_0}^{t_1}(x_0, .)$ among all vectors from $\mathbb{R}^3$. The direction $\xi_1(x_0)$, on the other hand, minimizes $\Lambda_{t_0}^{t_1}(x_0, .)$. We thus refer to the (right-) singular vector $\xi_2(x_0)$ as the *intermediate* (right-) singular vector of $DF_{t_0}^{t_1}(x_0)$. In many applications, the flow $F_{t_0}^{t_1}$ is volume-preserving (incompressible). Incompressibility means that $\sigma_1\sigma_2\sigma_3 = 1$ holds everywhere. Together with $0 < \sigma_1 < \sigma_2 < \sigma_3$, this implies that σ_2 is the singular value closest to unity (cf. Appendix 3.A). Accordingly, ξ_2 is the singular vector closest to unit stretching (i.e., $\Lambda_{t_0}^{t_1} = 1$).

The backward-time flow map $F_{t_1}^{t_0}$ yields a similar interpretation for the left-singular vectors $\eta_{1,2,3}(x_1)$: The backward-time deformation gradient, $DF_{t_1}^{t_0}(x_1)$, satisfies $DF_{t_1}^{t_0}(x_1) = \left[DF_{t_0}^{t_1}(x_0)\right]^{-1}$. The right-singular vectors of $DF_{t_1}^{t_0}(x_1)$ are, therefore, precisely the vectors $\eta_{1,2,3}(x_1)$; the left-singular vectors of $DF_{t_1}^{t_0}(x_1)$ are the $\xi_{1,2,3}(x_0)$. In backward time, the $\eta_{1,2,3}(x_1)$ hence play a similar role to $\xi_{1,2,3}(x_0)$ in forward time. With the singular values of $DF_{t_1}^{t_0}(x_1)$ being $[\sigma_{1,2,3}(x_0)]^{-1}$, it is, however, the vector $\eta_1(x_1)$ that maximizes $\Lambda_{t_1}^{t_0}$. This means, the direction of largest stretching in backward time is $\eta_1(x_1)$. Similarly, the vector $\eta_3(x_1)$ coincides with the direction of least stretching in backward time; and $\eta_2(x_1)$ is the intermediate (right-) singular vector of $DF_{t_1}^{t_0}(x_1)$.

Remark 3.4. By introducing the right Cauchy-Green strain tensor

$$C_{t_0}^{t_1}(x_0) = \left[DF_{t_0}^{t_1}(x_0)\right]^T DF_{t_0}^{t_1}(x_0)\,, \tag{3.9}$$

where the T-superscript indicates transposition, we recover the singular vectors $\xi_{1,2,3}(x_0)$ as eigenvectors of $C_{t_0}^{t_1}(x_0)$. The associated eigenvalues of $C_{t_0}^{t_1}(x_0)$ are $\lambda_{1,2,3}(x_0) =$

$[\sigma_{1,2,3}(x_0)]^2$. Similarly, introducing the left Cauchy-Green strain tensor [54] as

$$B_{t_0}^{t_1}(x_1) = DF_{t_0}^{t_1}(x_0)\left[DF_{t_0}^{t_1}(x_0)\right]^T, \tag{3.10}$$

where $x_0 = F_{t_1}^{t_0}(x_1)$, the left-singular vectors $\eta_{1,2,3}(x_1)$ are the eigenvectors of $B_{t_0}^{t_1}(x_1)$. The use of $C_{t_0}^{t_1}$ and $B_{t_0}^{t_1}$ is a common approach in the LCS literature [36, 40]. As it is, however, numerically advantageous to use SVD instead of eigendecomposition [83, 45], we will not use the Cauchy-Green strain tensors here.

From the above it follows that the hyperbolic LCSs introduced in Definition 3.2 can be specified in terms of the vectors $\xi_1(x_0)$, $\xi_3(x_0)$ (or $\eta_1(x_1)$, $\eta_3(x_1)$). (For a proof, see [9], Appendix C.)

Proposition 3.1. *A smooth material surface is a repelling hyperbolic LCS if its time-t_0 position is everywhere normal to the direction ξ_3 of largest stretching in forward time; or, if its time-t_1 position is everywhere normal to the direction η_3 of least stretching in backward time.*

Proposition 3.2. *A smooth material surface is an attracting hyperbolic LCS if its time-t_0 position is everywhere normal to the direction ξ_1 of least stretching in forward time; or, if its time-t_1 position is everywhere normal to the direction η_1 of largest stretching in backward time.*

Elliptic LCSs (cf. Definitions 3.3, 3.4) can be constructed similarly in terms of the $\xi_{1,2,3}(x_0)$ (or $\eta_{1,2,3}(x_1)$) and the $\sigma_{1,2,3}(x_0)$:

Proposition 3.3. *A smooth material surface is pointwise shear-maximizing if its time-t_0 position is everywhere normal to one of the two directions*

$$\tilde{n}^{\pm} = \tilde{\alpha}(\sigma_1, \sigma_2, \sigma_3)\, \xi_1 \pm \tilde{\gamma}(\sigma_1, \sigma_2, \sigma_3)\, \xi_3. \tag{3.11}$$

Here $\tilde{\alpha}$, $\tilde{\gamma}$ are positive functions of the singular values $\sigma_{1,2,3}$. (See [9] for the specific expressions for $\tilde{\alpha}$ and $\tilde{\gamma}$.)

Proof. See [9], Theorem 1. □

Proposition 3.4. *A smooth material surface is nearly uniformly stretching if its time-t_0 position is everywhere normal to one of the two directions*

$$n_\lambda^\pm = \alpha(\sigma_1, \sigma_2, \sigma_3, \lambda)\, \xi_1 \pm \gamma(\sigma_1, \sigma_2, \sigma_3, \lambda)\, \xi_3. \tag{3.12}$$

Here α, γ are positive functions of the singular values $\sigma_{1,2,3}$, and $\lambda \in [\sigma_2(1-\Delta), \sigma_2(1+\Delta)]$ with $0 \leq \Delta \ll 1$. (See [64] for the specific expressions for α and γ.)

Proof. See [64], Proposition 1. □

3.4 Main result: An autonomous dynamical system for all Lagrangian coherent structures in 3D

As reviewed in Sec. 3.3, all known LCSs in three dimensions are geometrically constrained by the singular vectors of the deformation gradient: Repelling hyperbolic LCSs are normal to the largest singular vector ξ_3 (Proposition 3.1); attracting hyperbolic LCSs normal to the smallest singular vector ξ_1 (Proposition 3.2); elliptic LCSs can be obtained as surfaces normal to certain linear combinations of ξ_1 and ξ_3 (Propositions 3.3, 3.4). All these definitions, therefore, pick out material surfaces $\mathcal{M}(t)$ which, at the initial time t_0, are perpendicular to a normal field n of the general form

$$n = a\xi_1 + c\xi_3, \tag{3.13}$$

with real functions a and c. In other words, any initial LCS surface $\mathcal{M}(t_0)$ is normal to a linear combination of the smallest and largest singular vector of $DF_{t_0}^{t_1}$. Consequently, the intermediate singular vector ξ_2 must always lie in the surface $\mathcal{M}(t_0)$. This means, $\mathcal{M}(t_0)$ is necessarily tangent to the ξ_2-direction field. An integral curve of the ξ_2-direction field launched from an arbitrary point of the surface $\mathcal{M}(t_0)$ will, therefore, remain confined to $\mathcal{M}(t_0)$ upon further integration. In the language of dynamical systems theory, we summarize this observation as follows (cf. Fig. 3.5):

Theorem 3.1. *The initial position $\mathcal{M}(t_0)$ of any hyperbolic LCS (Definition 3.2) or any elliptic LCS (Definitions 3.3, 3.4) is an invariant manifold of the autonomous dynamical system*

$$x_0' = \xi_2(x_0). \tag{3.14}$$

Similarly, final positions $\mathcal{M}(t_1)$ of hyperbolic and elliptic LCSs are invariant manifolds of the autonomous dynamical system

$$x_1' = \eta_2(x_1). \tag{3.15}$$

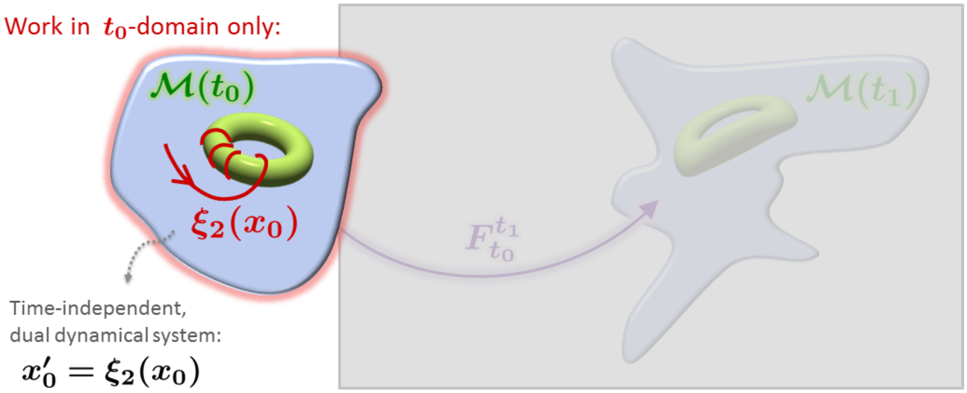

Fig. 3.5: Schematic of an elliptic LCS $\mathcal{M}(t)$, revealed as a toroidal invariant manifold $\mathcal{M}(t_0)$ of the autonomous dual dynamical system (3.14), cf. Theorem 3.1.

We refer to the autonomous systems (3.14)–(3.15) as the *dual dynamical systems* associated with the original, non-autonomous system (3.1) over the time interval $[t_0, t_1]$. The dynamics of these dual systems are not equivalent to the non-autonomous dynamical system (3.1). Rather, the dual systems allow locating the LCSs associated with (3.1) using classical methods for autonomous dynamical systems (e.g., Poincaré maps).

Since we usually identify LCS surfaces at the initial time t_0 (cf. Sec. 3.2), we will mostly discuss the ξ_2-system (3.14). Analogous results hold for the η_2-system (3.15).

Remark 3.5. We refer to the right-hand side of (3.14) as the ξ_2-*field*, to its integral curves as ξ_2-*lines*, and to its invariant manifolds as ξ_2-*invariant manifolds.* Calling (3.14) a dual dynamical system guides our intuition, but requires some clarification:

For (3.14) to be well-defined, we need to locally assign an orientation to the ξ_2-direction field. Along integral curves, once we assign an initial orientation, this can always be done in a smooth fashion (cf. Appendix 3.C). With this prescription, the orientation of trajectories in the ξ_2-system is defined unambiguously. (Since the ξ_2-vectors in (3.14) are unit vectors, here, the evolutionary variable is arclength.)

Theorem 3.1 enables locating unknown LCSs of all types using only one equation: Any two-dimensional invariant manifold $\mathcal{S}(t_0)$ of the ξ_2-system (3.14) is a surface that fulfills a necessary condition (i.e., tangency to ξ_2) required for the initial positions $\mathcal{M}(t_0)$ of both hyperbolic and elliptic LCSs. Since invariant manifolds of (3.14) are already exceptional objects by themselves, any ξ_2-invariant manifold $\mathcal{S}(t_0)$ that we obtain for a given dynamical system (3.1) is a relevant candidate for an LCS surface $\mathcal{M}(t_0)$.

Since the LCS normals from Propositions 3.1–3.4 do not encompass all linear combinations of ξ_1 and ξ_3, the converse of Theorem 3.1 does not hold. In other words, a ξ_2-invariant manifold $\mathcal{S}(t_0)$ does not necessarily correspond to an LCS $\mathcal{M}(t_0)$. To fully determine whether $\mathcal{S}(t_0)$ does satisfy one of the Definitions 3.2–3.4, therefore, one has to verify tangency to a second vector field (cf. Appendix 3.D). In applications, however, it is enough to categorize an LCS candidate qualitatively as either elliptic, hyperbolic repelling or attracting. As seen in the examples below (cf. Sec. 3.5), we can then omit the procedure in Appendix 3.D and examine both the topology of an LCS candidate $\mathcal{S}(t_0)$ and its image under the flow map, $\mathcal{S}(t_1)$, to assess if the material surface $\mathcal{S}(t)$ belongs to any of the three general LCS types: Any tubular surface $\mathcal{S}(t_0)$ is a candidate for an elliptic LCS, any sheet-like surface $\mathcal{S}(t_0)$ is a candidate for a hyperbolic LCSs. Mapping $\mathcal{S}(t_0)$ under the flow map reveals if $\mathcal{S}(t)$ indeed holds up as an elliptic or hyperbolic LCS.

As outlined in Sec. 3.1, previous approaches [9, 64] locate LCSs of all the types in three dimensions (Definitions 3.2–3.4) using the expressions for their surface normals from Propositions 3.1–3.4. Specifically, these methods sample the flow domain using extended families of two-dimensional reference planes. Taking the cross product between the LCS normal and the normal of each reference plane then defines two-dimensional direction fields to which the unknown LCS surfaces need to be tangent. These two-dimensional fields depend on the type of LCS; in particular, for the near-uniformly stretching LCSs, by (3.12), there are two parametric families of normal fields $n_\lambda^\pm$, which need to be sampled using a dense set of λ-parameters. Overall, therefore, one has to perform integrations of a large number of two-dimensional direction fields. (E.g., [64] obtained elliptic LCSs in the steady Arnold-Beltrami-Childress from integral curves of 1600 distinct direction fields.) Accordingly, this procedure typically produces a large collection of possible intersection curves between reference planes and LCSs. As a second step, these approaches require identification of curves from this collection that can be interpolated into LCS surfaces. Despite these efforts, the previous approaches [9, 64] do not enforce Theorem 3.1 and hence cannot guarantee more accurate LCS results than the present approach. An advantage is, however, that these approaches [9, 64] inherently distinguish between the specific normal fields given in Propositions 3.1–3.4 and hence do not require further analysis to determine the LCS type.

Clearly, opposed to the previous methods [9, 64] described above, analyzing the ξ_2-system (3.14) is a conceptually simpler approach to obtaining LCSs in three dimensions: First, the ξ_2-field is a single direction field suitable for all types of LCSs. Secondly, as opposed to considering a large number of independent two-dimensional equations, the ξ_2-system (3.14) is defined on a three-dimensional domain. In comparison to the methods in [9, 64], this eliminates the effort of handling large amounts of unutilized data and eliminates possible issues with the placement of reference planes. A full determination of the LCS types, however, requires verifying tangency to a second vector field (cf. Appendix 3.D).

In two dimensions, initial positions of LCSs can be viewed as invariant manifolds of differential equations similar to (3.14). There, however, the available LCS types (hyperbolic, parabolic and elliptic LCSs [35, 19, 37]) do not satisfy a single common differential equation: With only two right-singular vectors $\tilde{\xi}_{1,2}$ in two dimensions (and no counterpart to the intermediate eigenvector ξ_2 in three dimensions), the initial positions of hyperbolic and parabolic LCSs are defined by integral curves of either $\tilde{\xi}_1$ or $\tilde{\xi}_2$ [35, 19]. Similarly, elliptic LCSs are limit cycles of direction fields belonging to a parametric family of linear combinations of $\tilde{\xi}_1$ and $\tilde{\xi}_2$ [37]. Therefore, there cannot be a counterpart to Theorem 3.1 in two dimensions. Locating the LCSs in two dimensions requires analyzing all these differential equations separately.

In four dimensions and higher, there are no suitable extensions to the LCS definitions from Sec. 3.3, and hence there is no counterpart to Theorem 3.1 either (cf. Appendix 3.B).

3.5 Examples

In this section, we consider several (steady and time-aperiodic) flows and locate their LCSs by finding invariant manifolds of their associated ξ_2-fields. Our approach is to run long ξ_2-trajectories which may asymptotically accumulate on normally attracting invariant manifolds of the ξ_2-field (for numerical details, see Appendix 3.C). By Theorem 3.1, such invariant manifolds are candidates for time t_0-positions of LCSs. Obtaining the LCSs as attractors in the ξ_2-system ensures their robustness, whereas this property does not generally hold for them in the original non-autonomous system. (For incompressible flows, such as the examples in this section, there are no attractors at all.)

For a generally applicable numerical algorithm, a more refined method for obtaining two-dimensional invariant manifolds in three-dimensional, autonomous dynamical systems needs to be combined with the ideas presented here (cf. Sec. 3.6). We postpone these additional steps to future work.

We first consider steady examples where transport barriers are known from other approaches, and hence the results obtained from the ξ_2-system are readily verified. We then move on to an example with a temporally aperiodic velocity field.

3.5.1 Cat's eye flow

In Cartesian coordinates (x, y, z), consider a vector field

$$u(x,y,z) = \begin{pmatrix} -\partial_y \psi(x,y) \\ \partial_x \psi(x,y) \\ W \circ \psi(x,y) \end{pmatrix}, \tag{3.16}$$

where W, ψ are smooth, real-valued functions, and ψ is a stream function, i.e., $\Delta\psi = F(\psi)$ for some smooth function F. Any velocity field u satisfying (3.16) is a solution of the Euler equations of fluid motion in three dimensions [53]. We consider the two-and-a-half-dimensional Cat's eye flow [53], given by (3.16) with $W(\psi) = \exp(\psi)$ and

$$\psi(x,y) = -\log[c\cosh(y) + \sqrt{c^2-1}\cos(x)], \quad c = 2. \tag{3.17}$$

We assume that $u = u(x, y, z)$ is defined on the cylinder $S^1 \times \mathbb{R}^2$, with $x \in [0, 2\pi)$. Because u only depends on the x, y-coordinates here, i.e., $u = u(x, y)$, any flow generated by a velocity field u as in (3.16) is called two-and-a-half-dimensional.

Denoting the trajectory passing through (x_0, y_0, z_0) at time t_0 by $(x(t), y(t), z(t))$, the flow map takes the form $F_{t_0}^{t_1}(x_0, y_0, z_0) = (x_0, y_0, z_0)^T + \int_{t_0}^{t_1} u(x(s), y(s))ds$. Thus, the flow map $F_{t_0}^{t_1}$ is linear in z_0. Consequently, the deformation gradient $DF_{t_0}^{t_1}$, its singular values $\sigma_{1,2,3}$, and singular vectors $\xi_{1,2,3}$ do not depend on z_0.

Identifying the coordinates of the domain D of initial positions (x_0, y_0, z_0) with (x, y, z), we we cannot expect, however, that any of the $\xi_{1,2,3}$-fields will have a vanishing z-component, i.e., be effectively two-dimensional.

For the numerical integrations of the ξ_2-field (3.14), we choose 20 representative initial conditions p_0 in the plane $z = 0$ and, imposing the initial orientation such that the z-component of $\xi_2(p_0)$ is positive, we compute ξ_2-lines up to arclength $s = 500$. As the time-interval, we consider $[t_0, t_1] = [0, 100]$. We show the results in Fig. 3.6, together with level sets of ψ that correspond to the values $\psi(p_0)$. Each level set of ψ defines a two-dimensional invariant manifold of the Cat's eye flow. The ξ_2-lines are well-aligned with the corresponding level sets of ψ, including the separatrix, showing

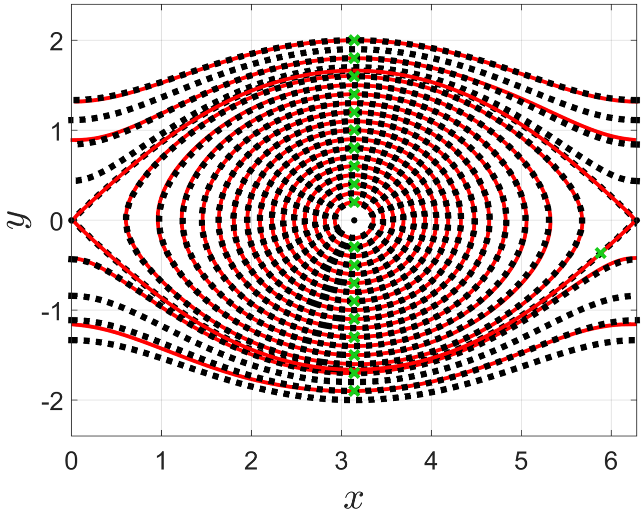

Fig. 3.6: Cat's eye flow: Comparison between x, y-projections of ξ_2-lines, displayed for arclength $s \in [0, 500]$, (solid red curves) and level sets of the stream function ψ (dotted black curves). The ξ_2-lines have nonzero z-components and are confined to generalized cylinders. The initial conditions of the ξ_2-lines, p_0, are marked by green crosses.

consistency between the possible locations of LCSs and the invariant manifolds of the Cat's eye velocity field. (We note that full alignment would require sampling the infinite-time dynamics of the Cat's eye flow, i.e., letting $t_1 \to \infty$ [36].) We observe that the x, y-projection of each ξ_2-line is a periodic orbit, and thus, each ξ_2-line is confined to a generalized (two-dimensional) cylinder.

3.5.2 Steady ABC flow

Our second steady example is a fully three-dimensional solution of the Euler equations, the steady Arnold-Beltrami-Childress (ABC) flow

$$u(x, y, z) = \begin{pmatrix} A\sin(z) + C\cos(y) \\ B\sin(x) + A\cos(z) \\ C\sin(y) + B\cos(x) \end{pmatrix}, \tag{3.18}$$

with $A = \sqrt{3}$, $B = \sqrt{2}$, $C = 1$. The coordinates in (3.18) are Cartesian, with $(x, y, z) \in [0, 2\pi]^3$ and periodic boundary conditions imposed in x, y and z.

Using the plane $z = 0$ as a Poincaré section, and placing in it a square grid of

20×20 initial positions (cf. Fig. 3.7a), we integrate trajectories of (3.18) from time 0 to time $2 \cdot 10^4$. Retaining only their long-time behavior from the time interval $[10^4, 2 \cdot 10^4]$, we obtain a large number of iterations of the Poincaré map (cf. Fig. 3.7b). The plot reveals 5 vortical regions surrounded by a chaotic sea. Each of the vortical regions contains a family of invariant tori that act as transport barriers.

Here we want to obtain both elliptic and hyperbolic LCSs using the dual ξ_2-system (3.14) for $[t_0, t_1] = [0, 10]$. The phase space of the ξ_2-system coincides with the domain of (3.18). In contrast to trajectories of u, independently of the time interval $[t_0, t_1]$, we can run ξ_2-lines as long as we need. Choosing the same Poincaré section and the same grid of initial conditions as above (cf. Fig. 3.7a), we integrate ξ_2-lines (initially aligned with $(0, 0, 1)$) up to arclength $5 \cdot 10^4$. Retaining segments from the arclength interval $[4 \cdot 10^4, 5 \cdot 10^4]$, and intersecting these segments with the $z = 0$ plane, we obtain iterations of a dual Poincaré map (cf. Fig. 3.7c). This Poincaré map indicates invariant manifolds of the dual ξ_2-system. Specifically, the principal vortices of the ABC flow correspond to families of invariant tori of the ξ_2-field (cf. Fig. 3.7c), which are candidates for initial positions of elliptic LCSs. The tori of the ξ_2-system are similar to the invariant tori obtained from the classical Poincaré map (cf. Fig. 3.7b). In the region corresponding to the chaotic sea, however, the

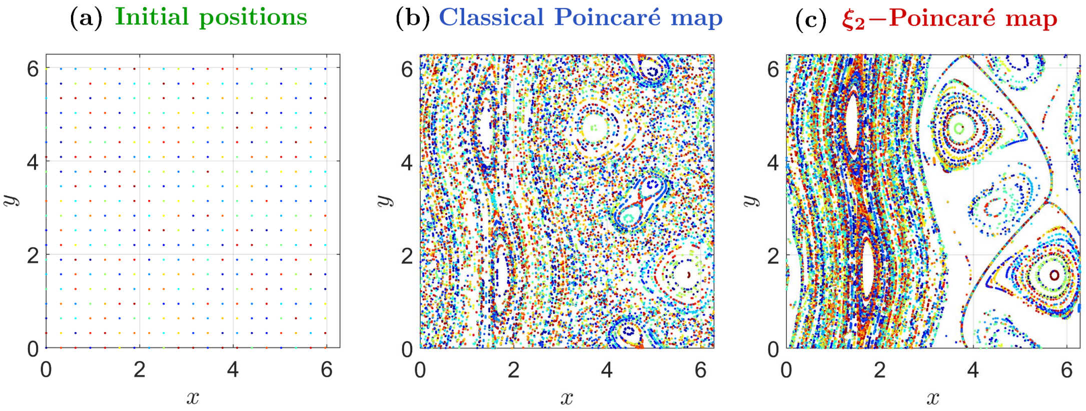

Fig. 3.7: Steady ABC flow: Comparison of Poincaré maps at $z = 0$. (a) Grid of 20×20 initial positions in the $z = 0$-plane. (b) Poincaré map of (3.18) obtained from trajectories over $[10^4, 2 \cdot 10^4]$, indicating invariant manifolds of the ABC flow; (c) Poincaré map of the ξ_2-field, obtained from ξ_2-lines over the arclength interval $[4 \cdot 10^4, 5 \cdot 10^4]$, indicating initial positions of LCSs.

ξ_2-field is strongly dissipative and thus reveals a candidate for a transport barrier in the ABC flow that has no counterpart in the classical Poincaré map obtained from the asymptotic dynamics of the incompressible system (3.18): We see a structure that has a large basin of attraction in the dual dynamics of the ξ_2-system and, secondly, spans the entire domain. In Sec. 3.5.3, we will examine a slightly perturbed version of this structure in detail, finding that it is a hyperbolic repelling LCS.

We note that computing Poincaré maps for the ξ_2-system does not imply applying the flow map $F_{t_0}^{t_1}$ repetitively. Iterating a ξ_2-based Poincaré map simply serves to refine our understanding of the LCSs associated with $F_{t_0}^{t_1}$. Indeed, the iterated Poincaré map highlights intersections of fixed LCSs with a given plane of the ξ_2-system in more and more detail.

3.5.3 Time-aperiodic ABC-type flow

We next use the dual ξ_2-system (3.14) to analyze a time-aperiodic modification of the ABC flow, given by (3.18) with the replacements

$$\begin{aligned} B \mapsto \tilde{B}(t) = \quad & B + B \cdot k_0 \tanh(k_1 t) \cos[(k_2 t)^2], \\ C \mapsto \tilde{C}(t) = \quad & C + C \cdot k_0 \tanh(k_1 t) \sin[(k_3 t)^2]. \end{aligned} \tag{3.19}$$

Neither a classical Poincaré map nor any other method requiring long trajectories are options here, due to the temporal aperiodicity of the system. In (3.19), we choose $k_0 = 0.3$, $k_1 = 0.5$, $k_2 = 1.5$ and $k_3 = 1.8$. We show the functions $\tilde{B}(t) - B$, $\tilde{C}(t) - C$ in Fig. 3.8. Elliptic LCSs in similar time-aperiodic ABC-type flows have been obtained in [9, 64]; hyperbolic repelling LCSs in [9], although only of small extent in the z-direction.

Considering the ξ_2-system for the time interval $[t_0, t_1] = [0, 5]$, we compute the dual Poincaré map (cf. Fig. 3.9a). The algorithm and numerical settings are the same as in Sec. 3.5.2. Compared to Fig. 3.7c, there are a few structures that persist under the time-aperiodic perturbation (3.19) to the velocity field (3.18): The large (presumably hyperbolic) structure spanning the flow domain is still present and barely changed. In

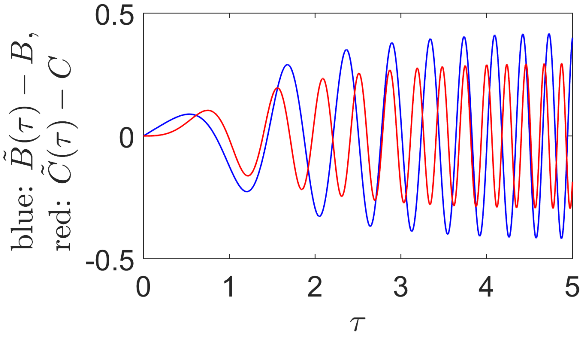

Fig. 3.8: Time dependence of the coefficient functions $\tilde{B}(t)$, $\tilde{C}(t)$ in (3.19).

Fig. 3.9b, we show ξ_2-lines corresponding to this hyperbolic LCS candidate (green). The ξ_2-lines indicate a complicated surface which they, however, do not cover densely. Regarding elliptic structures, instead of entire families of ξ_2-invariant tori, we are left with three large elliptic structures, each with a sizable domain of attraction (cf. Fig. 3.9a). The ξ_2-lines corresponding to these elliptic structures yield tori, which we show as tubular surfaces in Fig. 3.9b (red, blue, yellow). The dual Poincaré map (Fig. 3.9a) also shows that, inside two of these tori, there are additional, smaller elliptic structures. By plotting the ξ_2-lines corresponding to these smaller objects (not shown), we find that the surfaces they indicate are not tori and thus ignore them in our search for LCS candidates.

In Fig. 3.10a, we represent the yellow tubular surface from Fig. 3.9b in toroidal coordinates

$$\begin{aligned} \bar{x} &= \quad (x - x_c(z) + R_1)\cos(z), \\ \bar{y} &= \quad (x - x_c(z) + R_1)\sin(z), \\ \bar{z} &= \quad R_2(y - y_c(z)), \end{aligned} \tag{3.20}$$

with $R_1 = 2$, $R_2 = 1$. In (3.20), the functions $x_c(z)$, $y_c(z)$ are the x, y coordinates of the (approximate) vortex center. (For evaluating $x_c(z)$ and $y_c(z)$, we use our numerical values from previous work [64].) Mapping the resulting torus under the flow map F_0^5, we see that it does advect coherently over the interval $[t_0, t_1] = [0, 5]$ (cf. Fig. 3.10b). Therefore, even though this surface was just obtained from tangency to ξ_2 (a necessary condition for Definition 3.4), it renders a full-blown elliptic LCS.

We next examine locally whether the complicated green structure from Fig. 3.9b

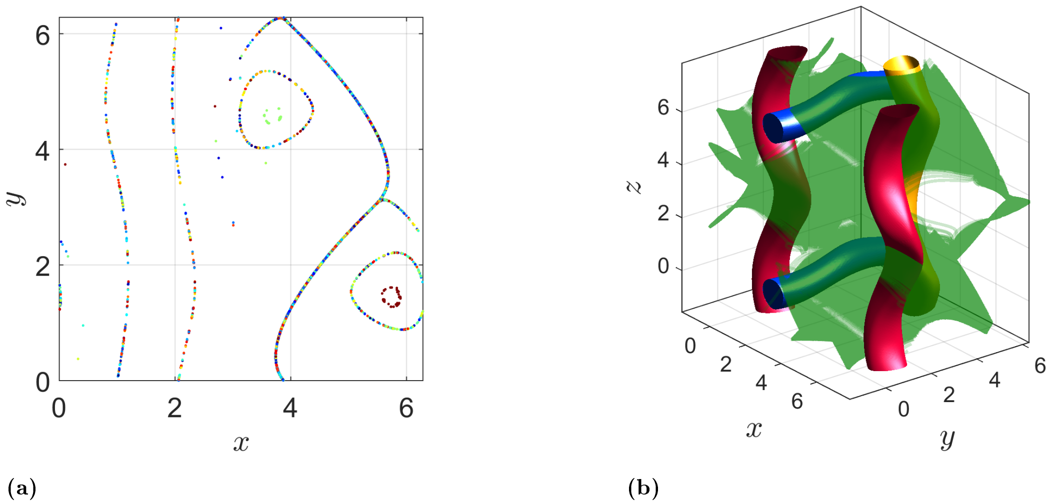

(a) **(b)**

Fig. 3.9: Time-aperiodic ABC-type flow: Arc segments of ξ_2-lines (corresponding to arclength $s \in [4 \cdot 10^4, 5 \cdot 10^4]$) reveal locations of elliptic and hyperbolic LCSs. (a) Dual Poincaré map, showing intersections between the Poincaré section $z = 0$ and possible time-t_0 locations of elliptic and hyperbolic LCSs. (b) Possible time-t_0 locations of elliptic and hyperbolic LCSs: The structure in green (indicating a hyperbolic LCS) consists of segments from several ξ_2-lines. The tubular surfaces (indicating elliptic LCSs) are fitted from point data of individual ξ_2-lines. Here we use the periodicity of the phase space to extend the domain slightly beyond $[0, 2\pi]^3$.

indeed corresponds to a hyperbolic LCS (Definition 3.2): In Fig. 3.11a, we take an illustrative part of the domain and interpolate a surface from the ξ_2-lines (green). Centered around a point in the surface, we additionally place a sphere of tracers (purple). Mapping the two objects forward in time under the flow map F_0^1, we see that the tracers deform into an ellipsoid that is most elongated in the direction normal to the advected surface (cf. Fig. 3.11b). Considering Proposition 3.1 and Fig. 3.4, we thus classify this structure as a repelling hyperbolic LCS. (For an approach to confirming this globally, see Appendix 3.D.) Considering Fig. 3.9b, we see that this structure is much larger than the hyperbolic LCS obtained for a similar time-aperiodic ABC-type flow in previous work (cf. [9], Fig. 15).

By Theorem 3.1, we can also take the direction field η_2 and repeat the above analysis. Using the same algorithm and numerical parameters as for the previous ξ_2-Poincaré map (cf. Fig. 3.9a), except that we now take the backward-time flow map F_5^0 instead of F_0^5, we obtain a Poincaré map for the dual dynamical system

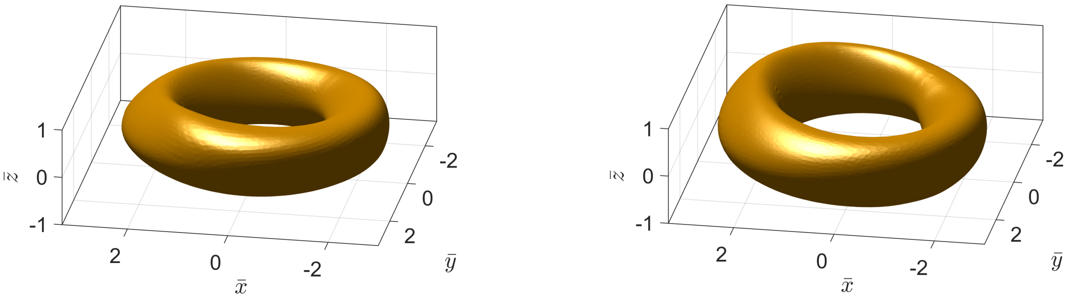

(a) **(b)**

Fig. 3.10: Time-aperiodic ABC-type flow: Mapping one of the tubular surfaces obtained from the ξ_2-lines (cf. Fig. 3.9b, yellow) under the flow map F_0^5, we confirm that this surface is a useful elliptic LCS. (a) Elliptic LCS surface at time $t_0 = 0$. (b) Elliptic LCS surface at time $t_1 = 5$.

$x_1' = \eta_2(x_1)$ (cf. Fig. 3.12). This Poincaré map reveals possible time-t_1 positions of LCSs. The result is similar to the ξ_2-Poincaré map (cf. Fig. 3.9a), showing again a large hyperbolic structure, and the time-t_1 positions of the tori obtained earlier (cf. Fig. 3.9b).

We perform a local deformation analysis for the large hyperbolic structure indicated by Fig. 3.12: From a sample part of the η_2-lines corresponding to this structure, we fit a surface (cf. Fig. 3.13b, colored green) and map it backward in time under F_5^4, obtaining a surface at time $t = 4$ (cf. Fig. 3.13a, green). Then we place a small tracer sphere (purple) in this part of the surface. Mapping both the time-4 surface and the tracer sphere forward in time under F_4^5, we find that the tracers fully align with the surface (cf. Fig. 3.13b). By Proposition 3.2 and Fig. 3.4, this suggests that the large hyperbolic structure from Fig. 3.12 belongs to the time-t_1 position of an attracting hyperbolic LCS. (For confirming this globally, see Appendix 3.D.)

Remark 3.6. With the present approach, for incompressible flows, it is generally easier to obtain attracting hyperbolic LCSs $\mathcal{M}(t_1)$ at time t_1, rather than at time t_0: An attracting LCS at time t_0 is a surface $\mathcal{M}(t_0)$ parallel to ξ_2 and ξ_3 (cf. Proposition 3.2). Mapping $\mathcal{M}(t_0)$ to $\mathcal{M}(t_1)$, the area element changes by a factor of $\sigma_2\sigma_3$. Due to incompressibility ($\sigma_1\sigma_2\sigma_3 = 1$), any attracting LCS is guaranteed to stretch in forward-time ($\sigma_2\sigma_3 > 1$). Since separation can, e.g., grow exponentially in time

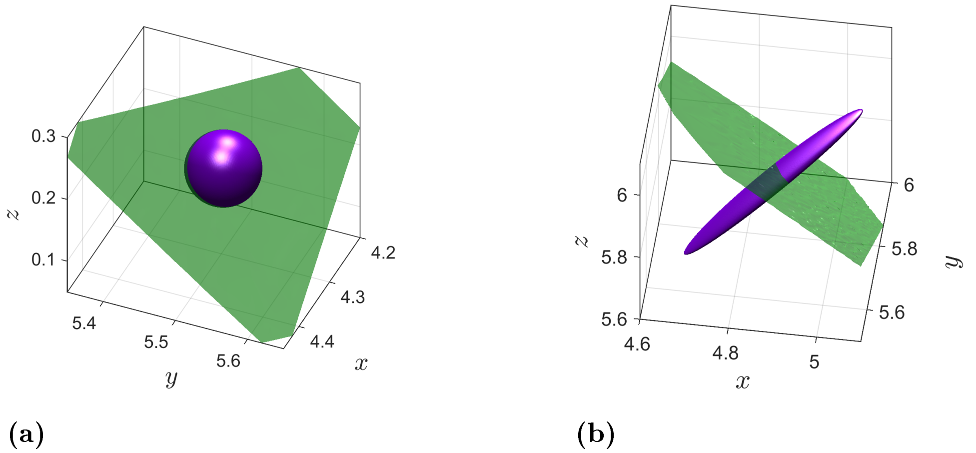

(a) **(b)**

Fig. 3.11: Time-aperiodic ABC-type flow: Local impact of the hyperbolic repelling LCS surface (interpolated from ξ_2-lines). (a) Zoom-in on the hyperbolic repelling LCS surface at time $t_0 = 0$ (green), shown together with a sphere formed by tracers (purple). (b) Time-1 positions of the hyperbolic repelling LCS surface and the deformed tracer sphere (obtained under F_0^1).

($\sigma_3 \propto \exp(t_1 - t_0)$), we generally expect the stretching of an attracting LCS to be substantial ($\sigma_2\sigma_3 \gg 1$). At the final time t_1, we thus expect that any attracting LCS of global impact, $\mathcal{M}(t_1)$, traverses a significant portion of the phase space. At time t_0, on the other hand, the surface $\mathcal{M}(t_0)$ can still be very small. In this sense, seeking LCSs as invariant manifolds of the η_2-field is generally easier than using the ξ_2-field. For repelling LCSs, which shrink between times t_0 and t_1, the converse holds. (In two dimensions, the challenges of computing repelling and attracting hyperbolic LCSs at different times t^* are similar [21, 46].)

In summary, compared to previous methods of identifying LCSs from various two-dimensional direction fields [9, 64], the advantage of the present approach is that it reveals both hyperbolic and elliptic LCSs from integrations of a single direction field. Instead of using multiple one-dimensional Poincaré sections [9, 64], we can therefore search LCSs globally by using two-dimensional Poincaré sections (cf. Figs. 3.7c, 3.9a, 3.12). Finally, as opposed to classical Poincaré maps that require autonomous or time-periodic systems, the dual Poincaré map is well-defined for any non-autonomous system. We in fact treat autonomous, time-periodic and time-aperiodic dynamical systems on the same footing, while still benefiting from the advantages that a classical

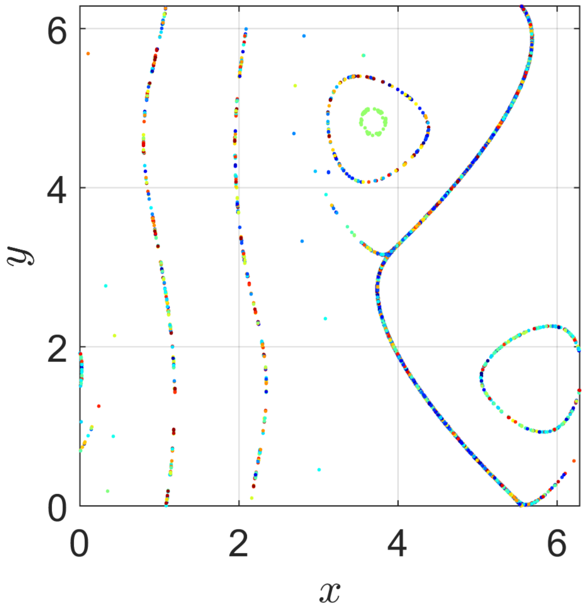

Fig. 3.12: Dual Poincaré map obtained from $x_1' = \eta_2(x_1)$, showing intersections between the Poincaré section $z = 0$ and possible time-t_1 locations of elliptic and hyperbolic LCSs.

Poincaré map offers.

3.6 Conclusions

We have presented a unified approach to obtaining elliptic and hyperbolic LCSs in three-dimensional unsteady flows. In contrast to prior methods based on different direction fields for different types of LCSs [9, 64], we obtain a common direction field, the intermediate eigenvector field, $\xi_2(x_0)$, of the right Cauchy-Green strain tensor. Initial positions of all variational LCSs in three dimensions are necessarily invariant manifolds of this autonomous direction field. Equivalently, LCS final positions are invariant manifolds of the intermediate eigenvector field, $\eta_2(x_1)$, of the left Cauchy-Green strain tensor. We can thus identify LCS surfaces globally by classic methods for autonomous dynamical systems. While the ξ_2- and η_2-systems by themselves do not discriminate between LCS types, the procedure from Appendix 3.D outlines how to numerically assess the LCS type if needed.

Overall, the present approach is significantly simpler than previous numerical

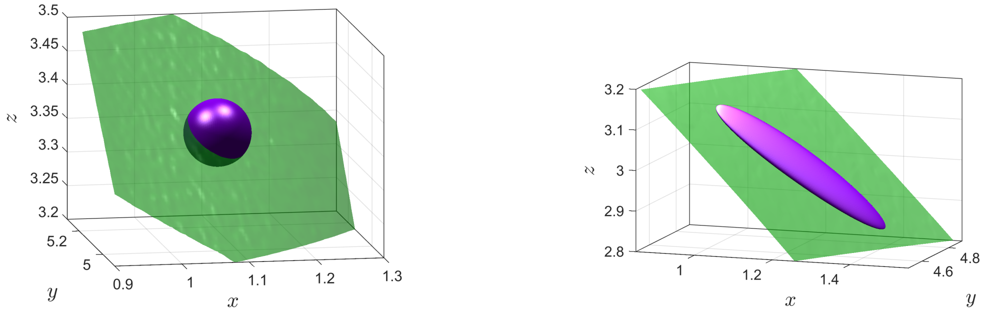

(a) **(b)**

Fig. 3.13: Time-aperiodic ABC-type flow: Local impact of the hyperbolic attracting LCS surface (fitted from η_2-lines). (a) Zoom-in on the hyperbolic attracting LCS surface at time $t = 4$ (green), shown together with a sphere formed by tracers (purple). (b) Time-t_1 positions of the hyperbolic attracting LCS surface and the deformed tracer sphere (obtained under F_4^5).

methods [9, 64], and reveals larger hyperbolic LCSs in the time-aperiodic ABC-type flow than seen in a comparable example from previous work [9]. An important advantage of our approach is that LCSs are attractors of the generally dissipative ξ_2-system, which is not the case in the original, typically incompressible system. Obtaining the LCSs as attractors of the dual ξ_2-system also guarantees their structural stability, implying that these structures will persist under small perturbations to the underlying flow. Our approach is restricted to three-dimensional systems, which is, however, highly relevant for fluid mechanical applications.

With the examples of Sec. 3.5, we have illustrated the ability of the ξ_2-system to reveal LCSs. For a broadly applicable numerical method, further development is required. Computing two-dimensional invariant manifolds of the ξ_2-field by simply running long integral curves is not always efficient. General approaches for growing global stable and unstable manifolds of autonomous, three-dimensional vector fields are, however, available in the literature (cf. [50] for a review). We expect that a general computational method for obtaining LCSs from the ξ_2-system (3.14) can be most easily developed by transferring one of these available approaches to computing invariant manifolds from the setting of vector fields to direction fields. For a given dynamical system, one would first compute the ξ_2-field on a grid, and then apply the most suitable method for growing invariant manifolds to construct LCSs globally in the dual ξ_2-system.

3.A For incompressible flows, σ_2 is the singular value of $DF_{t_0}^{t_1}$ closest to unity

We clarify our statement that $0 < \sigma_1 < \sigma_2 < \sigma_3$ and incompressibility (i.e., $\sigma_1\sigma_2\sigma_3 = 1$) imply that σ_2 is the singular value of $DF_{t_0}^{t_1}$ closest to unity. We first note that $\sigma_1 = \sqrt[3]{\sigma_1^3} < \sqrt[3]{\sigma_1\sigma_2\sigma_3} = 1$, and, similarly, $\sigma_3 > 1$. In general, it is unclear whether $\sigma_2 < 1$, $\sigma_2 = 1$, or $\sigma_2 > 1$. Due to the inequalities

$$\sigma_1 < \min\left\{\sigma_2, \frac{1}{\sigma_2}\right\} \leq 1 \leq \max\left\{\sigma_2, \frac{1}{\sigma_2}\right\} < \sigma_3, \tag{3.21}$$

however, we consider σ_2 as the singular value closest to unity. Eq. 3.21 follows from a more general statement:

Lemma 3.1. *Given any three real numbers a, b, and c satisfying $0 < a < b < c$, denoting their geometric mean by*

$$m = \sqrt[3]{abc}, \tag{3.22}$$

we have

$$\frac{a}{m} < \min\left\{\frac{b}{m}, \frac{m}{b}\right\} \leq 1 \leq \max\left\{\frac{b}{m}, \frac{m}{b}\right\} < \frac{c}{m}. \tag{3.23}$$

Proof. Denoting the natural logarithm by log, we introduce $M = \log(m)$, $A = \log(a)$, $B = \log(b)$, and $C = \log(c)$. Taking the logarithm of (3.22), we then obtain

$$3M = A + B + C. \tag{3.24}$$

Furthermore, since $a = \sqrt[3]{a^3} < \sqrt[3]{abc} = m$, we have

$$M - A > 0, \tag{3.25}$$

and, similarly,

$$C - M > 0. \tag{3.26}$$

1. For the first inequality in (3.23), we show that $a/m < m/b$. By strict monotonicity of the logarithm, this is equivalent to $\log\left(\frac{a}{m}\right) < \log\left(\frac{m}{b}\right)$, which we verify as follows:

   $$\log\left(\tfrac{a}{m}\right) = A-M \overset{(3.24)}{=} 3M-B-C-M = (M-B)-(C-M) \overset{(3.26)}{<} M-B = \log\left(\tfrac{m}{b}\right).$$

   For the last inequality in (3.23), we can similarly show that $m/b < c/m$ (using (3.25) instead of (3.26)).

2. We show that $\min\left\{\log\left(\frac{b}{m}\right), \log\left(\frac{m}{b}\right)\right\} \leq 0$, which is equivalent to $\min\left\{\frac{b}{m}, \frac{m}{b}\right\} \leq 1$. To verify the former inequality, we use that the minimum of any two real numbers r_1 and r_2 satisfies $\min\{r_1, r_2\} = \frac{r_1+r_2}{2} - \frac{|r_1-r_2|}{2}$. We obtain

   $$\min\left\{\log\left(\tfrac{b}{m}\right), \log\left(\tfrac{m}{b}\right)\right\} = \tfrac{1}{2}\left[(B-M)+(M-B)\right] - \tfrac{1}{2}\left|(B-M)-(M-B)\right|,$$

   and, thus,

   $$\min\left\{\log\left(\tfrac{b}{m}\right), \log\left(\tfrac{m}{b}\right)\right\} = -\left|B-M\right| \leq 0.$$

   Similarly, we can use $\max\{r_1, r_2\} = \frac{r_1+r_2}{2} + \frac{|r_1-r_2|}{2}$ and show that $1 \leq \max\left\{\frac{b}{m}, \frac{m}{b}\right\}$.

□

Setting $a = \sigma_1$, $b = \sigma_2$, $c = \sigma_3$ and $m = 1$, Lemma 3.1 implies (3.21).

3.B Theorem 3.1 and higher dimensions

We discuss the possibility of a counterpart to our main result, Theorem 3.1, in higher dimensions. We start with four dimensions, where there are four singular vectors $\xi_{1,2,3,4}$. As in Sec. 3.3, we label them such that the corresponding singular values $\sigma_{1,2,3,4}$ are in ascending order.

Example. As a prerequisite, we would need to extend, e.g., the notion of a hyperbolic repelling LCS (cf. Definition 3.2) from three to four dimensions. As in Proposition 3.1, we would need a three-dimensional hypersurface $\mathcal{M}(t_0)$ in $\mathbb{R}^4$ which is normal to ξ_4 and hence tangent to $\xi_{1,2,3}$ everywhere. It is not a priori obvious whether such a geometry is possible or not.

Consider a small open ball $B \subset \mathbb{R}^4$ where the singular values $\sigma_{1,2,3,4}$ are distinct. Within B, we may assume that the $\xi_{1,2,3,4}$-fields are smooth vector fields. We denote the Lie bracket between two such vector fields v and w by $[v, w]$.

We want to construct a three-dimensional hypersurface $\mathcal{M}(t_0)$ such that $\mathcal{M}(t_0) \cap B$ is normal to ξ_4. This is possible only if the fields $\xi_{1,2,3}$ satisfy

$$[\xi_1, \xi_2], [\xi_1, \xi_3], [\xi_2, \xi_3] \in \operatorname{span}\{\xi_1, \xi_2, \xi_3\} \tag{3.27}$$

for all points in $\mathcal{M}(t_0) \cap B$ (cf., e.g., [52]). Conditions (3.27) are equivalent to the Frobenius conditions

$$\langle [\xi_1, \xi_2], \xi_4 \rangle = 0,\ \langle [\xi_1, \xi_3], \xi_4 \rangle = 0,\ \langle [\xi_2, \xi_3], \xi_4 \rangle = 0. \tag{3.28}$$

(In the context of LCSs, such conditions have already been considered in [9].) Unless 0 is a critical value, by the Preimage Theorem [28], each of the three conditions in (3.28) defines a codimension-one submanifold in B. Now there are two main possibilities:

Case 1: We suppose that 0 is a regular value for all conditions in (3.28). Since the conditions (3.28) are generally independent from each other, the subset S of B where all three conditions are satisfied simultaneously is codimension-three, i.e., a line. For $\mathcal{M}(t_0)$ to be a well-defined repelling LCS, we need $\mathcal{M}(t_0) \cap B$ to be a subset of S. By our assumption, however, $\mathcal{M}(t_0) \cap B$ is a three-dimensional hypersurface. Since S is only one-dimensional, we have reached a contradiction.

Case 2: The remaining possibility is that 0 is a critical value for at least one of the conditions in (3.28). Then there is no general restriction on the geometry of the corresponding zero-level sets from (3.28). In particular, if 0 is critical value for at least two of the three conditions in (3.28), then the subset S of B where all three conditions are satisfied simultaneously can be a three- or four-dimensional manifold. In this case, S can contain a three-dimensional surface $\mathcal{M}(t_0) \cap B$ and, thus, locally allow for a repelling LCS $\mathcal{M}(t_0)$. The catch is, however, that the set of critical values for each of the conditions in (3.28) has measure zero in $\mathbb{R}$. (This is due to Sard's Theorem [28].) Because of inevitable numerical inaccuracies and imprecisions, with probability 1, the collection of practically available $\xi_{1,2,3,4}$-fields will hence produce a regular value for each of the Frobenius conditions in (3.28). This brings us back to *Case 1*.

We conclude that only *Case 1* is relevant in practice. (Unless, of course, a special symmetry of the flow map $F_{t_0}^{t_1}$ implies that the Frobenius conditions (3.28) are not independent to begin with.) Straightforwardly extending Definition 3.2 and, therefore, seeking hyperbolic repelling LCSs as surfaces normal to ξ_4 is not a useful approach for general dynamical systems $\dot{x} = u(x, t)$ in four dimensions.

The above discussion holds in any dimension $N \in \{4, 5, ...\}$ and for any LCS type: From a collection of $N - 1$ vector fields, we can pick $f = \binom{N-1}{2}$ pairs, yielding precisely f Frobenius conditions (cf. (3.28)). For useful and general LCS definitions in the spirit of Sec. 3.3, we would generally need $f = 1$, but this is only achieved for $N = 3$. This precludes straightforward extensions of Theorem 3.1 from three to higher dimensions.

3.C Numerical details for the examples

Here we describe the details of our numerical approach. These apply to all the examples in Sec. 3.5.

In order to evaluate ξ_2, we need to compute both the flow map $F_{t_0}^{t_1}$ and its derivative $DF_{t_0}^{t_1}$. Here we do not use finite differentiating in order to obtain $DF_{t_0}^{t_1}$ from $F_{t_0}^{t_1}$(cf., e.g., [36]), but we explicitly solve for $DF_{t_0}^{t_1}$. Since the flow map $F_{t_0}^{t}$ satisfies

$$\frac{d}{dt}F_{t_0}^{t}(x_0) = u(F_{t_0}^{t}(x_0), t), \tag{3.29}$$

we differentiate (3.29) with respect to x_0, and conclude that $DF_{t_0}^{t}(x_0)$ evolves according to the well-known equation of variations

$$\frac{d}{dt}DF_{t_0}^{t}(x_0) = Du\left(F_{t_0}^{t}(x_0), t\right) DF_{t_0}^{t}(x_0). \tag{3.30}$$

Written out in coordinates, (3.30) is a system of nine equations that is coupled to the three equations in (3.29) and, therefore, both (3.29) and (3.30) need to be solved simultaneously as a system of 12 variables. We can thus obtain $DF_{t_0}^{t_1}$ and ξ_2 to very high accuracy, which we need for running long integral curves of (3.14).

Once $DF_{t_0}^{t_1}$ is available, rather than using the Cauchy-Green strain tensor [36], we obtain ξ_2 by SVD (cf. Remark 3.4 and [83]). (For η_2, we use the backward-time deformation gradient $DF_{t_1}^{t_0}$.)

We do not compute the ξ_2-field on a spatial grid, but just along the ξ_2-lines that we integrate. This ensures that we can locate both small and highly-modulated LCSs, instead of risking to accidentally undersample unknown structures. At each point of the curve, we assign the orientation of ξ_2 to be the same as it was at the previous point on the curve. For the initial point, one has to make a manual choice; e.g., in Cartesian coordinates (x, y, z), impose alignment with the $(0, 0, 1)$-direction.

We perform all the integrations using a Runge-Kutta (4,5) method [17], with an adaptive stepper at absolute and relative error tolerances of $Tol = 10^{-8}$.

Finally, we obtain all the Poincaré maps from trajectories (of either u, ξ_2, or η_2) by plotting the (x, y)-point data corresponding to z-values from $[0, \varepsilon] \cup [2\pi - \varepsilon, 2\pi]$, with $\varepsilon = 2 \cdot 10^{-3}$.

For the steady ABC flow (cf. Sec. 3.5.2), we evaluate how the equation of variations (3.30) improves the results for ξ_2 compared to finite differencing of $F_{t_0}^{t_1}$ (cf.

[36]). We define a uniform rectangular grid of 500×500 initial conditions x_0 in the plane given by $\{(x, y, 0) : x, y \in [0, 2\pi]\}$, for which we evaluate $DF_{t_0}^{t_1}$ and thus ξ_2 using these two methods. We perform finite differencing as described in [36], Eq. 9, with $\delta_{1,2,3} = 10^{-5} e_{1,2,3}$ and $e_{1,2,3}$ denoting the unit vectors in the x, y, z coordinate directions. In Fig. 3.14a, we show the angle between ξ_2 obtained using (3.30) and ξ_2 obtained from finite differencing of $F_{t_0}^{t_1}$. The former method can be considered practically exact here, with the only numerical parameter being $Tol = 10^{-8}$ (checked for convergence). The largest error we find in Fig. 3.14a is approximately 88.35°. Since ξ_2 is only defined up to orientation, the largest possible error would be 90°. Hence we conclude from Fig. 3.14a that finite differencing can cause arbitrarily large errors in ξ_2. Even though errors are confined to locations of exceptionally large separation, as indicated by the finite-time Lyapunov exponent (FTLE) field (cf. Fig. 3.14b), these locations belong to ridges of the FTLE field, a widely used indicator of hyperbolic LCSs [36]. Since we want to globally detect hyperbolic LCSs by integrating the ξ_2-field, we use (3.30) to determine ξ_2.

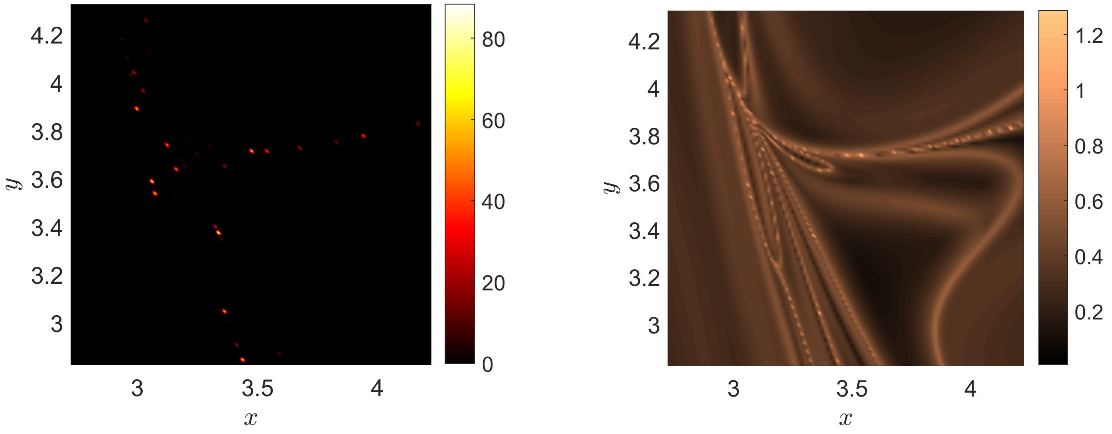

(a) **(b)**

Fig. 3.14: Steady ABC flow: Error due to finite differencing. (a) Angle in degrees between ξ_2 obtained from finite differencing of $F_{t_0}^{t_1}$ (cf. [36]) and ξ_2 obtained using the equation of variations (3.30). (b) FTLE $(t_1 - t_0)^{-1} \log \sigma_3$ obtained using the equation of variations (3.30).

We note that even when the velocity field (3.1) is only available through data from experiments and simulations, the equation of variations (3.30) has been used to obtain numerically accurate results for the flow map and its gradient [61].

3.D Perturbations to the ξ_2-field

In Figs. 3.11a, 3.11b, we place a tracer sphere in an LCS candidate surface, finding that it stretches most in the direction normal to the surface. Based on this local property, in Sec. 3.5.3, we conclude that the entire surface should be a repelling LCS. Even though we expect any hyperbolic LCS obtained from a forward-time computation to be repelling (cf. Remark 3.6), it is desirable to have a global approach to assessing the LCS type of a candidate surface.

If we consider, e.g., a repelling LCS $\mathcal{M}(t_0)$, at any point $x_0 \in \mathcal{M}(t_0)$, the tangent space $T_{x_0}\mathcal{M}(t_0)$ is the subspace of $\mathbb{R}^3$ spanned by $\xi_2(x_0)$ and $\xi_1(x_0)$ (cf. Proposition 3.1). By repeating the reasoning that leads to Theorem 3.1, we conclude that any repelling LCS $\mathcal{M}(t_0)$ must be an invariant manifold of any dynamical system of the form

$$x_0' = p\,\xi_2(x_0) + (1-p)\xi_1(x_0), \quad p \in [0,1].$$

By Propositions 3.2–3.4, we can make similar observations for the remaining LCS types. In summary:

Proposition 3.5. *For any parameter value $p \in [0,1]$, the initial position $\mathcal{M}(t_0)$ of any hyperbolic or elliptic LCS (Definitions 3.2–3.4) is an invariant manifold of the autonomous dual dynamical system*

$$x_0' = p\,\xi_2(x_0) + (1-p)\tilde{\xi}(x_0)\,, \tag{3.31}$$

with $\tilde{\xi}$=ξ_3 for attracting hyperbolic LCSs; $\tilde{\xi} = \xi_1$ for repelling hyperbolic LCSs; and $\tilde{\xi} = \mp\tilde{\gamma}\xi_1 + \tilde{\alpha}\xi_3$ or $\tilde{\xi} = \mp\gamma\xi_1 + \alpha\xi_3$ for elliptic LCSs (cf. (3.11), (3.12)).

Remark 3.7. Replacing the $\xi_{1,2,3}$ by $\sigma_{1,2,3} \cdot \eta_{1,2,3}$, Proposition 3.5 applies *verbatim* to final LCS positions $\mathcal{M}(t_1)$.

This means that for each LCS type, there is a specific family of dual dynamical systems that yields the respective LCS initial positions as invariant manifolds. The dual dynamical system associated with ξ_2 remains exceptional though, because this is the only dual dynamical system shared by all LCS types (cf. Proposition 3.5).

We now demonstrate how these observations help to determine the LCS type of a candidate surface: For the hyperbolic LCS candidate in the time-aperiodic ABC-type flow (cf. Sec. 3.5.3), it turns out that only a single long ξ_2-line is enough to indicate the surface (cf. Fig. 3.15a). Specifically, among the ξ_2-lines that get attracted to the hyperbolic LCS candidate surface in the dual Poincaré map (cf. Fig. 3.9a), we have randomly picked the ξ_2-line with initial condition approximately equal to $(5.03, 3.14, 0.00)$. Other choices of ξ_2-lines yield similar results.

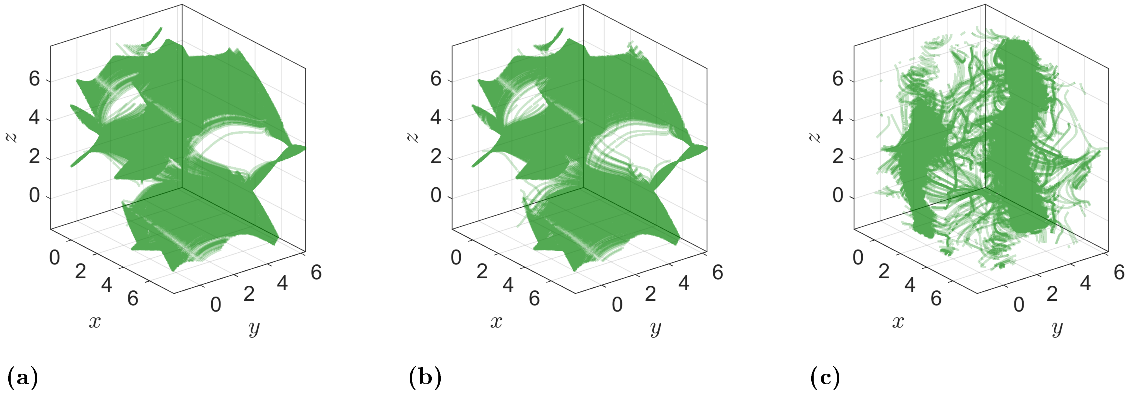

Fig. 3.15: Time-aperiodic ABC-type flow: Arc segments of integral curves of three $\xi_2 + \varepsilon\tilde{\xi}$ fields. (Each curve is shown for arclength parameter $s \in [4 \cdot 10^4, 5 \cdot 10^4]$). The initial condition is approximately $(5.03, 3.14, 0.00)$ for all three integral curves. Here we use the periodicity of the phase space to extend the domain slightly beyond $[0, 2\pi]^3$. (a) A ξ_2-line ($\varepsilon = 0$) indicates the hyperbolic candidate surface obtained from the dual Poincaré map (cf. Fig. 3.9a). (b) An integral curve of $\xi_2 + \varepsilon\xi_1$ ($\varepsilon = 0.01$) reproduces the hyperbolic candidate surface obtained from the corresponding ξ_2-line (cf. Fig. 3.15a). (c) An integral curve of $\xi_2 + \varepsilon\xi_3$ ($\varepsilon = 0.01$) does not reproduce the hyperbolic candidate surface obtained from the corresponding ξ_2-line (cf. Fig. 3.15a).

We next add a small perturbation to the ξ_2-field, i.e., consider the dual dynamical system

$$x_0' = \xi_2(x_0) + \varepsilon\xi_1(x_0), \tag{3.32}$$

with $\varepsilon = 0.01$. Using the same initial condition and numerical settings as above, we compute an integral curve of (3.32). The result indicates virtually the same surface as obtained from the ξ_2-field (cf. Fig. 3.15b). This suggests that this surface is invariant for the entire family of direction fields $p\xi_2 + (1-p)\xi_1$. By Proposition 3.5, the entire structure should hence be a repelling LCS.

If we, on the other hand, repeat the above computation for the dual dynamical system

$$x_0' = \xi_2(x_0) + \varepsilon\xi_3(x_0), \tag{3.33}$$

where $\varepsilon = 0.01$, then the entire structure disappears, and the attractor for this initial condition remains unclear (cf. Fig. 3.15c). Even though the perturbation $\varepsilon\xi_3$ is small, the dynamics of (3.33) is completely different than for (3.32). This is consistent with our conclusion that the structure from Figs. 3.15a, 3.15b is a repelling hyperbolic LCS.

Chapter 4

Invisible Anchors Trap Particles in Branching Junctions

4.1 Introduction

Branching junctions are common building blocks of pipe networks appearing in industrial applications [51] and in the arterial system [44]. By their simple geometry, one anticipates straightforward fluid behavior in these configurations for moderate flow velocities. In particular, pumping a particle-laden fluid into the inlet of a branching junction (Fig. 4.1), one naturally expects that both the fluid and the particles will exit through the two outlets. Recent observations, however, reveal the possibility that light particles, such as gas bubbles in water, become trapped and remain in the junction indefinitely [81]. The capture process leads to the formation of large particle clouds at the crossing between pipes. This phenomenon occurs for a significant range of Reynolds numbers, for several types of light particles, and for various junction angles [81, 8].

Investigations of the fluid phase link the capture mechanism to flow reversal caused by bubble-type vortex breakdown structures emerging near the junction [12, 8]. The geometry and stability of these vortical structures strongly depends on the Reynolds number and the junction angle, and undergoes bifurcations [12, 13].

While these flow features of the fluid phase give strong indications of trapping, here we focus on the fluid-particle interactions, directly investigating the dynamics of individual particles. This enables us to answer detailed questions about the capture mechanism, such as: How large are the regions where particles become trapped? How do particles accumulate within these trapping regions?

4.2 Experiment: The dynamics of a single trapped particle

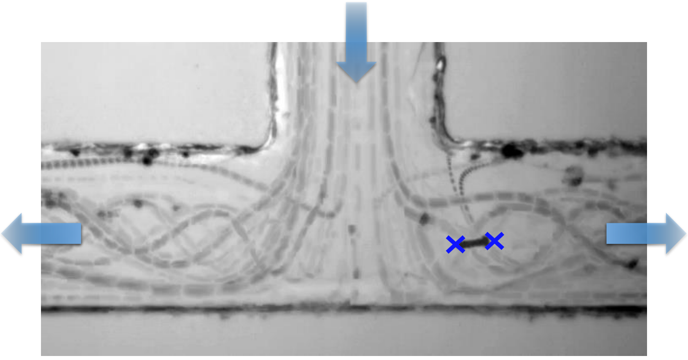

Fig. 4.1: Merger of frames from video footage of a T-junction experiment with hollow glass beads in a stationary flow of water (Reynolds number $\mathrm{Re} = 277$). Large arrows mark the inlet (*top*) and two outlets (*left, right*). Beads are released at the inlet and then exit through one of the two outlets. The spiraling of some bead paths (*dark gray curves*) is due to vortex breakdown in the left and right arms. For later comparisons with Fig. 4.3, blue crosses mark estimated positions of two fixed points. The dark line between these points is the path of a captured bead (cf. Fig. 4.2).

Footage from an experiment with hollow glass beads in a stationary flow through a T-junction (Fig. 4.1; cf. [8] for experimental details) shows that most particles quickly exit the junction. Their paths lead either directly to an outlet, or, near the vortices in the lower arms of the junction, show brief recirculation.

As shown in Figs. 4.2 (a), (c), however, within the right vortical region, we find a single particle at rest. This particle remains at its spot for a long period, until it is displaced by another, passing particle (Fig. 4.2 (d)). After briefly moving into the downstream direction, the particle develops rapid spiraling and then stops its downstream motion (Fig. 4.2 (e)). Afterwards, the particle slowly creeps back to

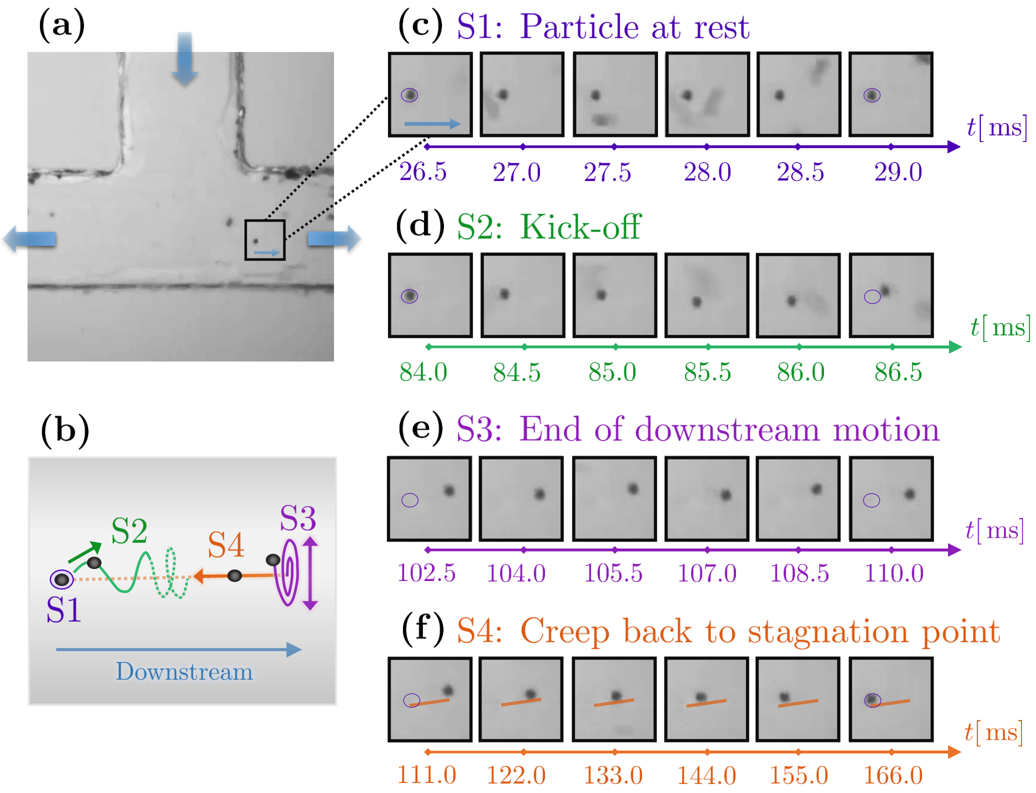

Fig. 4.2: Snapshots from video footage of an experiment on a T-junction at Re=277 (cf. Fig. 4.1). The axes in (c)-(f) measure time t in ms. **(a)** Overview, with large arrows marking the inlet (*top*) and the two outlets (*left, right*). The black box marks the fixed subregion shown in (c)-(f). **(b)** Illustration of the four sequences S1-S4 shown in (c)-(f) **(c)** A particle is at rest at a fixed point, while other particles pass by quickly. The small blue arrow indicates the downstream direction. **(d)** The particle is displaced by another, passing particle, then begins to move downstream. **(e)** After spiraling downstream (not shown), the particle stops its downstream motion and oscillates perpendicularly to the downstream direction. **(f)** Moving along a line (*orange*), the particle slowly creeps back to its starting position.

its original spot (Fig. 4.2 (f)). We summarize the four sequences in Fig. 4.2 (b). The observations suggest that, in this setting, the particle dynamics share important similarities with the dynamics of the fluid: First, one of the fixed points known for the fluid phase (cf. [8]), is preserved for particles and becomes attracting for light particles. Secondly, particle trajectories resemble streamlines observed in bubble-type vortex breakdown [8, 12].

4.3 Simulations of particle trajectories using the Maxey-Riley equation and its leading-order reduction

We consider particles as small, noninteracting spheres, and choose two representative pipe geometries, a T-junction at $\mathrm{Re} = 320$, and a V-junction at a junction angle of $70°$ and $\mathrm{Re} = 230$. The pipe cross sections are squares of side length $\ell_w = 10^{-3}\,\mathrm{m}$. The average pump speed at the inlet is $\bar{u} = \frac{\mathrm{Re}\,\nu}{\ell_w}$, where ν denotes viscosity. Rescaling length by $L = \ell_w$, velocity by $U = \bar{u}$, and time by $T = \frac{L}{U}$, we model the particle motion by the dimensionless Maxey-Riley equation [79, 39]

$$\dot{\boldsymbol{x}} = \boldsymbol{v}, \quad \dot{\boldsymbol{v}} = \beta \frac{D\boldsymbol{u}}{Dt} - \frac{1}{\tau}(\boldsymbol{v} - \boldsymbol{u}). \tag{4.1}$$

Here, $\boldsymbol{x} = (x, y, z)$ is the particle position, $\boldsymbol{v}$ is the particle velocity, and $\boldsymbol{u}$ is the fluid velocity field. Furthermore, in (4.1), $\frac{D}{Dt} = \partial_t + (\boldsymbol{u} \cdot \nabla)$ is the material derivative; $\beta = \frac{3}{1+2\rho}$ is function of the ratio ρ between the densities ρ_p of the particles and ρ_f of the fluid, $\rho = \rho_p/\rho_f$; and τ is the Stokes time. In terms of particle size a and Stokes number $\mathrm{St} = \frac{2}{9}a^2\mathrm{Re}$, we have $\tau = \frac{3}{2\beta}\mathrm{St}$.

For the fluid velocity field $\boldsymbol{u}$ required by Eq. (4.1), we use a finite-volume solver from the OpenFOAM library [84] and obtain steady solutions to the three-dimensional, incompressible Navier-Stokes equations for water (cf. [12] for details). For the particles, we consider hollow glass beads ($\rho = 0.15$, $0.001 \lesssim a \lesssim 0.140$) and gas bubbles ($\rho = 10^{-3}$, $0.001 \lesssim a \lesssim 0.050$) [8].

Eq. (4.1) is a variant of the Maxey-Riley equation [56] that accounts for the force due to the undisturbed fluid flow, for the added mass effect, and for the Stokes drag. We note that the Stokes-drag law is only valid away from the wall. Since the particles are small, we neglect the Faxén corrections in (4.1), which are $\mathcal{O}(a^2)$ relative to the remaining terms. Denoting the gravitational acceleration by g, we have $gL/U^2 \ll 1$, which prompts us to neglect gravity in (4.1). We also neglect the Basset-Boussinesq memory force. This assumption facilitates the numerics and allows for a dimensional reduction (cf. (4.2) below). While including the memory force appears to preserve the structures that underly particle accumulation, in some cases, their influence is weakened by this inclusion [15]. We hence perform an a-posteriori validation of our main result, finding that the effect of the memory force is negligible (cf. Sec. 4.A).

We note that particle trajectories obtained from an approach similar to (4.1), based on Newton's law and accounting for both fluid-particle and particle-particle interactions, qualitatively reproduce the formation of elongated particle clouds at the junction [81].

With the introduction of a synthetic velocity field for the particles, $\tilde{\boldsymbol{v}} = \tilde{\boldsymbol{v}}(\boldsymbol{x}, t)$, the asymptotic behavior of (4.1) is captured by the inertial equation [39]

$$\dot{\boldsymbol{x}} = \tilde{\boldsymbol{v}} = \boldsymbol{u} + \varepsilon \frac{D\boldsymbol{u}}{Dt}, \tag{4.2}$$

where ε is a new small parameter defined as

$$\varepsilon = \tau\,(\beta - 1) = \mathrm{St}\,(1 - \rho)\,. \tag{4.3}$$

The velocity field $\tilde{\boldsymbol{v}}$ is generally compressible, leading to the accumulation and dispersion of particles over time. Viewing (4.1) as a singular perturbation problem with small perturbation parameter τ, (4.2) is obtained as a first-order reduction of (4.1) onto a globally attracting slow manifold in the extended phase space $(\boldsymbol{x}, t, \boldsymbol{v})$ [39]. For small τ and ε, solutions of (4.2) quickly synchronize with solutions for the $\boldsymbol{x}$-variable in (4.1). Passing from (4.1) to (4.2) reduces the dimension of the phase space from six to three. In addition, with ε in (4.2) replacing τ and β from (4.1), the number of independent parameters reduces from two to one.

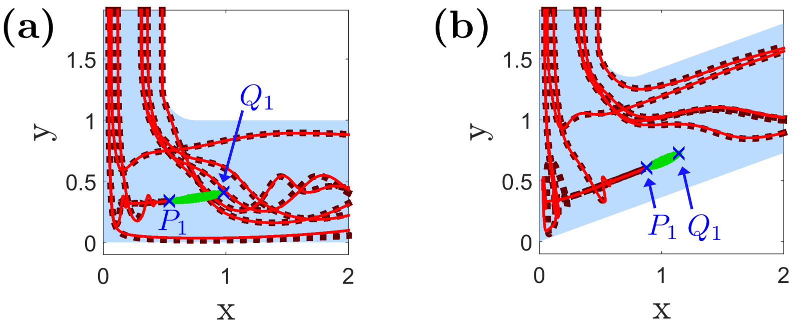

Fig. 4.3: Representative trajectories of hollow glass beads ($\rho = 0.15$) in the T- and V-junction flows, obtained from (4.2) (*red, solid lines*), and compared to trajectories of (4.1) (*brown, dashed lines*). Blue crosses mark fixed points P_1 and Q_1 of (4.2), and define the up- and downstream ends of the bubble-type vortex breakdown regions (*green*, visualized using fluid streamlines). The parameters are $\beta = 2.3078$, $\tau = 0.0382$, $\mathrm{St} = 0.0588$. **(a)** T-junction, **(b)** V-junction.

Equation (4.2) allows us to study particle motion by using the compressible velocity field $\tilde{\boldsymbol{v}}$, which differs from the underlying fluid velocity field $\boldsymbol{u}$ only by a small $\mathcal{O}(\varepsilon)$ perturbation. This is consistent with our observations from the video footage that a fixed point for the particles exists, and that particle trajectories are similar to the known streamlines.

In Fig. 4.3, we show representative trajectories of hollow glass beads in the T- and V-junction flows. Both (4.1) and (4.2) produce very similar results. For the T-junction (Fig. 4.3 (a)), the geometry of trajectories agrees with earlier simulation results [81] and the experimental observations from the video (cf. Fig. 4.1). Beads entering from the inlet cross section ($y = 2$) either leave the junction directly or spiral near the vortical region. In addition, some beads become captured: Within time $t \lesssim 2$, their trajectories quickly spiral to a one-dimensional manifold that looks like an extension of the vortex axis connecting P_1 and Q_1. Later, these beads slowly approach the attracting fixed point P_1 (after $t \gg 10$ in the V-junction). The point P_1 corresponds to the fixed point we observe in the experiment (cf. Fig. 4.2). The result for the V-junction (Fig. 4.3 (b)) is similar, up to an overall deformation due to the angled geometry. Exploiting the advantages of the inertial equation (4.2) discussed above, we next perform all our computations of particle motion using (4.2). In particular, by (4.3), ε replaces the commonly used parameters St and ρ.

4.4 Regions of particle trapping in T-and V-junction flows

We now investigate the regions within the flow that lead to the trapping of particles. We define a trapping region (TR) as a subdomain of the flow such that, for fixed ε, particles released within the TR will remain inside the TR for all times. In order to guarantee trapping, a TR must not intersect any of the outlets of the junction. By its definition, therefore, the boundary of a TR is an invariant manifold of (4.2). That is, for particles at fixed ε, the boundary of a TR is an impenetrable surface that divides the flow domain into an interior (leading to trapping) and an exterior (a region from which particles leave the junction).

With Fig. 4.3 suggesting that the fixed point $P_1 = (P_{1x}, P_{1y}, P_{1z})$ and its three mirror images at $P_2 = (-P_{1x}, P_{1y}, P_{1z})$, $P_3 = (P_{1x}, P_{1y}, -P_{1z})$ and $P_4 = (-P_{1x}, P_{1y}, -P_{1z})$ are the primary capture locations as $t \to \infty$ (for secondary capture regions, cf. Fig. 4.9 below), we compute the domains of attraction of $P_{1,2,3,4}$. Our results (Fig. 4.4) show that these domains do not intersect the outlets and, hence, they define TRs. Particles released within a TR accumulate at $P_{1,2,3,4}$ and hence remain trapped in the junction forever. Specifically, for medium-sized hollow glass beads in the T-junction (Fig. 4.4 (a), (b)), both $P_{1,2}$ and $P_{3,4}$ define two separate TRs that touch at $x = 0, z = 0$. These TRs intersect the inlet cross-section, allowing for incoming particles to be trapped.

Just as the vortex breakdown regions (cf. Fig. 4.3, shown in *green*), which have been used to predict particle capture previously [8], the TRs end at fixed points $Q_{1,2}$ and $Q_{3,4}$ (Fig. 4.4 (b)). Comparing Figs. 4.3 and 4.4 (b), however, we observe that the TRs occupy a much larger part of the flow domain than the vortex breakdown regions. Each TR resembles an anchor and contains one vortex in each arm. We are unaware of prior descriptions in the literature.

For medium-sized beads in the V-junction flow, we find similar TRs (Fig. 4.4 (c)). Their boundaries strongly impact the shape of nearby trajectories: Passing trajectories are deformed by the TRs before exiting the junction. Inside the TRs, particles start spiraling away from the surface and quickly converge to the one-dimensional manifold described earlier (cf. Fig. 4.3). The fast attraction within the TRs explains why previous dye experiments (cf. Fig. S8 in [81]) did not reveal these regions. Despite their extraordinary impact on particle motion, therefore, the anchor-shaped boundaries of TRs are practically invisible surfaces.

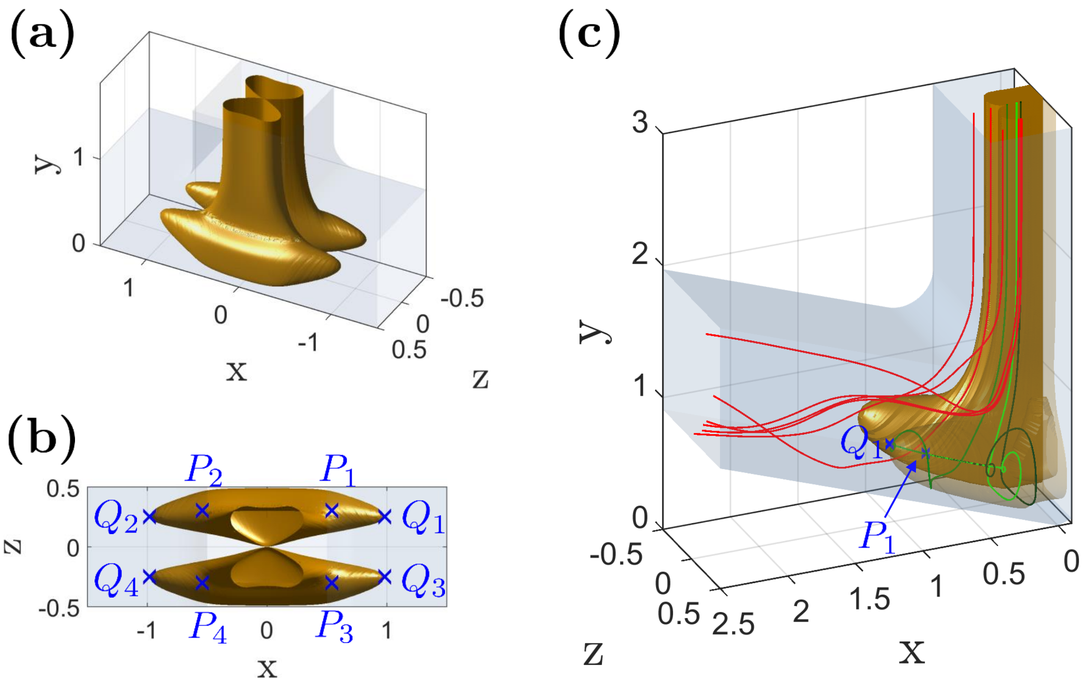

Fig. 4.4: Primary trapping regions (TRs, colored *yellow*) in the T- and V-junction flows for $\varepsilon = 0.05$. This value of ε corresponds to, e.g., medium-sized bubbles ($\rho = 10^{-3}$) with $\beta = 2.994$, $\tau = 0.0251$, St $= 0.0501$, or medium-sized hollow glass beads ($\rho = 0.15$) with $\beta = 2.3078$, $\tau = 0.0382$, St $= 0.0588$. Blue crosses mark the fixed points $P_{1,2,3,4}$ and $Q_{1,2,3,4}$. (**a**) T-junction (**b**) T-junction, viewed from top (**c**) V-junction, with representative trajectories. The boundary of the TR separates trajectories of two different types: trajectories that pass by and exit through the outlet (*red*), versus trajectories that remain inside the TR and quickly spiral onto the extended vortex axis (*green*).

We explore the parameter dependence of the TRs by considering different values of ε that correspond to the full range of particle sizes in the experiments with gas bubbles (cf. [8]). For the smallest bubbles in the V-junction flow ($a = 0.001$, St $\approx \varepsilon \approx 5.1 \cdot 10^{-5}$), we do not observe trapping. For slightly larger bubbles ($a = 0.006$, St $\approx \varepsilon \approx 1.9 \cdot 10^{-3}$, cf. Fig. 4.5 (a)), we find two well-separated TRs that reach all

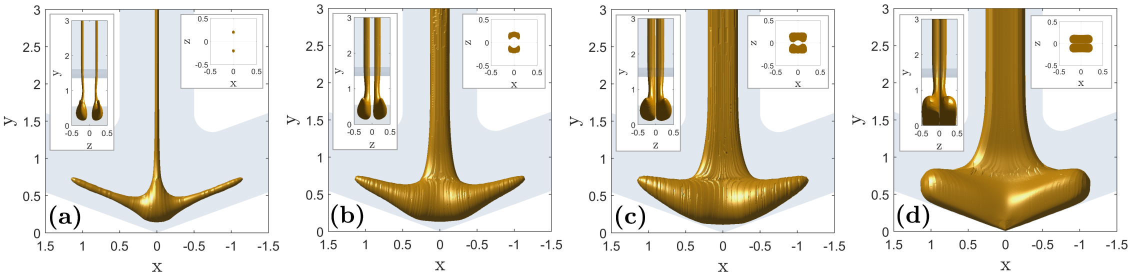

Fig. 4.5: Trapping regions in the V-junction flow, shown for different Stokes numbers St representing the range of experimentally observed bubble sizes (between $a = 1\,\mu$m and $a = 50\,\mu$m [8]). (a) St $\approx \varepsilon \approx 1.9 \cdot 10^{-3}$ ($a = 6.0\,\mu$m), (b) St $\approx \varepsilon \approx 6.6 \cdot 10^{-3}$ ($a = 11.4\,\mu$m), (c) critical case, merger of TRs: St $\approx \varepsilon = \varepsilon_M \approx 0.0164$ ($a = 17.9\,\mu$m), (d) St $\approx \varepsilon \approx 0.128$ ($a = 50\,\mu$m). Insets on the left: zy views showing that below the critical Stokes number St ≈ 0.0164, the TRs are well separated. Insets on the upper right: intersections of the inlet cross section ($y = 3$) with the TRs.

the way up into the inlet arm. Since their intersection with the inlet is small (Fig. 4.5 (a), *right inset*), however, it is highly unlikely that these TR capture bubbles entering at random positions of the inlet.

Increasing the particle size further (Fig. 4.5 (b)), the TRs grow and their separation decreases. For St $\approx \varepsilon_M \approx 0.0164$, the TRs are so close to each other that, within the inlet cross-section, their minimum distance is equal to the particle size ($a = 0.0179$; cf. Fig. 4.5 (c), *right inset*). For consistency with our model, which represents finite-size particles as points, we view this as a merger of the two separate TRs into a single, larger TR. The critical value $\varepsilon_M \approx 0.0164$, therefore, defines a topological transition for the trapping of gas bubbles in the V-junction flow.

For the largest bubbles ($a = 0.050$, St $\approx \varepsilon \approx 0.128$, cf. Fig. 4.5 (d)) the two TRs indeed touch over a large distance and form a single large TR that occupies a significant portion of the inlet cross-section (right inset). Overall, however, the TR is so large that it touches the domain boundary over large areas. Since the Stokes-drag law is not valid close to the wall, our model is inconclusive in these regions, and hence we expect that the size of the TR shown in Fig. 4.5 (c), (d) is an overestimate.

Given that ε is the only parameter in (4.2), within our approximation, the TRs for hollow glass beads are identical to Fig. 4.5. Due to (4.3), however, the critical value

ε_M for the merger of the two TRs for beads is $\varepsilon_M \approx 0.165$ (for bubbles: $\varepsilon_M \approx 0.164$).

For the T-junction, for $\varepsilon > \varepsilon_M$, we find that the TRs touch along the line defined by $x = 0, z = 0$ (cf. Fig. 4.4 (b)). The numerical values for ε_M are $\varepsilon_M \approx 0.0291$ for bubbles and $\varepsilon_M \approx 0.0296$ for hollow glass beads. Even for $\varepsilon \gg \varepsilon_M$, however, the TRs continue to touch only along that line. Unlike for the V-junction, therefore, we regard the TRs as remaining separate here.

Due to the symmetry of $P_{1,2,3,4}$, the stability of the fixed point P_1 determines the existence of the TRs shown above. By (4.2), we monitor the signs of the real parts of the eigenvalues of $\nabla \tilde{\boldsymbol{v}}(\boldsymbol{x})|_{\boldsymbol{x}=P_1}$: In both the T- and V-junction flows, for $\varepsilon < \varepsilon_C$, the eigenvalue for the eigenvector aligned with the breakdown vortex axis has positive real part, causing instability and preventing trapping. For $\varepsilon > \varepsilon_C$, the eigenvalue becomes negative, turning P_1 into an attracting fixed point and leading to trapping. The numerical values are $\varepsilon_C \approx 0.00123$ for the T-junction and $\varepsilon_C \approx 0.00183$ for the V-junction. In contrast to ε_M, within our approximation, the value of ε_C does not depend on the particle type.

By (4.3), the condition $\varepsilon > \varepsilon_C$ defines a parameter region of ρ and St where particle capture in the T- and V-junctions occurs (Figs. 4.6 (a) and (b)). Since the values of ε_C for the T- and V-junction are similar, these regions are almost identical for both cases. Overall, Fig. 4.6 predicts that, for high enough St, any light particle ($\rho < 1$) becomes captured. This result is different from previous work [81] which, using a force balance of the simplified fluid-particle forces, estimates that capture is only possible for light particles of $\rho \lesssim 0.7$.

In addition, we find a lower limit on St: for $\mathrm{St} < \varepsilon_C$, even the lightest particles ($\rho \to 0$) are not captured. In particular, we do not expect capture for some of the smallest bubbles and hollow glass beads appearing in the experiments [8] (T-junction: $1\,\mu\mathrm{m} \lesssim a \lesssim 4.5\,\mu\mathrm{m}$, V-junction: $1\,\mu\mathrm{m} \lesssim a \lesssim 6.5\,\mu\mathrm{m}$).

For the V-junction (Fig. 4.6 (b)), the parameter region for particle capture is furthermore divided into two subregions where trapping either occurs in two separate TRs (cf. Fig. 4.5 (a), (b)), or, for $\varepsilon > \varepsilon_M$, in a single TR (cf. Fig. 4.5 (d)). As we note above, however, the value of ε_M has a minor dependence on the particle type.

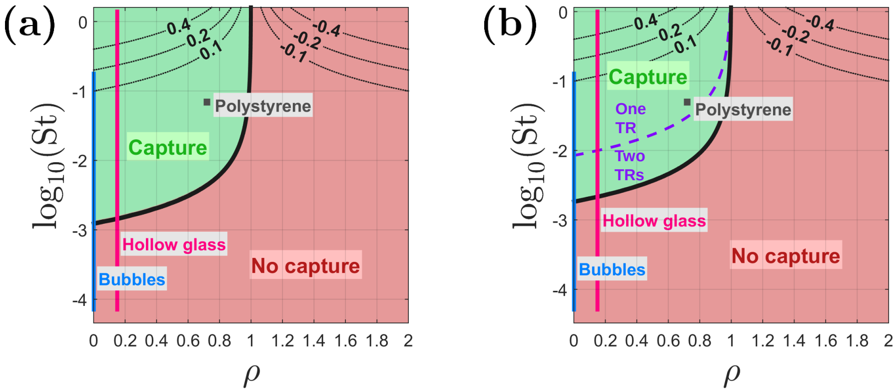

Fig. 4.6: Parameter regions of St and ρ where capture occurs. Bars and squares mark St and ρ values of particles from the experiments in [8]: gas bubbles (*blue*), hollow glass beads (*magenta*) and polystyrene beads (*gray*). The *thin black* curves are level sets of ε, see (4.3), and indicate the parameter region where we expect that (4.2) ceases to be valid. **(a)** T-junction at Re $= 320$, **(b)** V-junction at Re$=230$. Capture occurs either in two TRs, or, for $\varepsilon > \varepsilon_M \approx 0.0296$, in a single TR.

4.5 Particle accumulation over finite times

So far, we have studied trapping in the infinite-time limit, and observed that particles either leave the junction, or approach one of the fixed points $P_{1,2,3,4}$. Examining representative trajectories (cf. Fig. 4.3) suggests that, in the trapping process, particles quickly spiral towards the extended axis of the vortex and then slowly approach the fixed points $P_{1,2,3,4}$. Instead of considering individual trajectories, however, we want to directly assess how particles accumulate within the flow over time.

We define $n_{t_0}(\boldsymbol{x}_0)$ as the number of particles in a volume element $V = V_{t_0}(\boldsymbol{x}_0)$ located at any point $\boldsymbol{x}_0$ at an initial time t_0. Evolving V under an arbitrary particle velocity field $\tilde{\boldsymbol{v}}(\boldsymbol{x}, t)$ until the present time t_1, the volume element $V = V_t(\boldsymbol{x}(t))$ moves along the trajectory $\boldsymbol{x}(t)$ of (4.2) given by

$$\dot{\boldsymbol{x}}(t) = \tilde{\boldsymbol{v}}(\boldsymbol{x}(t), t), \quad \boldsymbol{x}(t_0) = \boldsymbol{x}_0, \quad \boldsymbol{x}(t_1) = \boldsymbol{x}_1. \tag{4.4}$$

Along this path $\boldsymbol{x}(t)$, by Liouville's formula [76], the nonzero divergence of $\tilde{\boldsymbol{v}}$ leads to a compression or an expansion of V. By the uniqueness of solutions of (4.2), particles cannot leave the volume $V_t(\boldsymbol{x}(t))$ and, therefore, the number density $n_{t_1}(\boldsymbol{x}_1)$ at time t_1 satisfies

$$n_{t_1}(\boldsymbol{x}_1) = n_{t_0}(\boldsymbol{x}_0) \exp\left[-\int_{t_0}^{t_1} \nabla \cdot \tilde{\boldsymbol{v}}(\boldsymbol{x}(t), t) dt\right]. \tag{4.5}$$

By (4.2), we obtain $\nabla \cdot \tilde{\boldsymbol{v}} = -2\varepsilon Q$ (cf. [39]), where

$$Q(\boldsymbol{x}, t) = \frac{1}{2}\left(|\boldsymbol{\Omega}(\boldsymbol{x}, t)|^2 - |\mathbf{S}(\boldsymbol{x}, t)|^2\right). \tag{4.6}$$

The function Q is a widely-used parameter in vortex detection [43], comparing the Euclidean norm $|\cdot|$ of the spin tensor $\boldsymbol{\Omega} = \frac{1}{2}\left(\nabla \boldsymbol{u} - (\nabla \boldsymbol{u})^T\right)$ to that of the strain rate tensor $\mathbf{S} = \frac{1}{2}\left(\nabla \boldsymbol{u} + (\nabla \boldsymbol{u})^T\right)$. From (4.5), we conclude that particles accumulate according to

$$\log\left(\frac{n_{t_1}(\boldsymbol{x}_1)}{n_{t_0}(\boldsymbol{x}_0)}\right) = LAQ_{t_0}^{t_1}, \tag{4.7}$$

with the Lagrangian-averaged Q defined as

$$LAQ_{t_0}^{t_1} = 2\varepsilon \int_{t_0}^{t_1} Q(\boldsymbol{x}(t), t) dt. \tag{4.8}$$

For heavy particles, a similar result was obtained by Maxey [55]. Since the trajectory $\boldsymbol{x}(t)$ provides a unique link between initial and final positions $\boldsymbol{x}_0$ and $\boldsymbol{x}_1$, we consider $LAQ_{t_0}^{t_1}$ either as a function of $\boldsymbol{x}_0$, or as a function of $\boldsymbol{x}_1$. High values of $LAQ_{t_0}^{t_1}(\boldsymbol{x}_1)$ simply highlight regions where light particles accumulate at the present time t_1 (Fig. 4.7). Instead of advecting randomly initialized particles to produce accumulation patterns that can be hard to interpret (cf., e.g. [11]), computing $LAQ_{t_0}^{t_1}(\boldsymbol{x}_1)$ is a direct way of visualizing and quantifying preferential concentrations. Additionally, the $LAQ_{t_0}^{t_1}(\boldsymbol{x}_0)$ field highlights the initial locations of high particle density, which are the origins of particle accumulation. Because simulations and experiments produce data only over finite time intervals, varying t_1 in (4.7) allows to track the entire accumulation process.

We compute slices of the $LAQ_{t_0}^{t_1}(\boldsymbol{x}_1)$ fields for medium-sized bubbles in the T- and V-junctions (Fig. 4.8). For our computations, we create dense grids of initial conditions $\boldsymbol{x}_1$ in the xy plane at P_1 and evaluate (4.8) backward in time. Similar uses

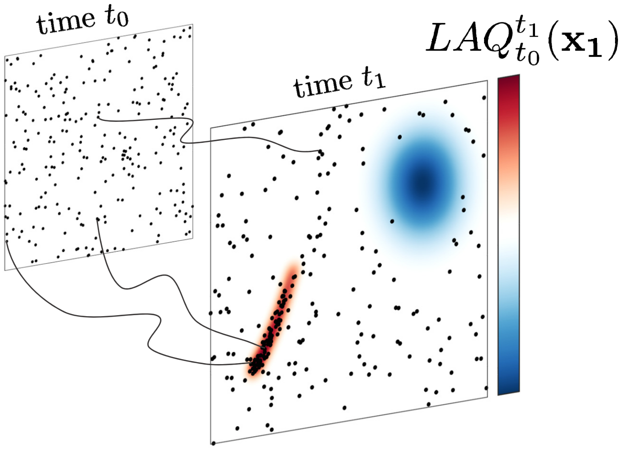

Fig. 4.7: Illustration of how uniformly randomly initialized particles (*black dots*) accumulate or disperse under advection by (4.2). Integral curves (*black*) of (4.2) link initial particle positions $\boldsymbol{x}_0$ at time t_0 to their final positions $\boldsymbol{x}_1$ at time t_1. High $LAQ_{t_0}^{t_1}(\boldsymbol{x}_1)$ values (*red*) highlight regions where light particles accumulate at time t_1. Low $LAQ_{t_0}^{t_1}(\boldsymbol{x}_1)$ values (*blue*) indicate regions that light particles avoid.

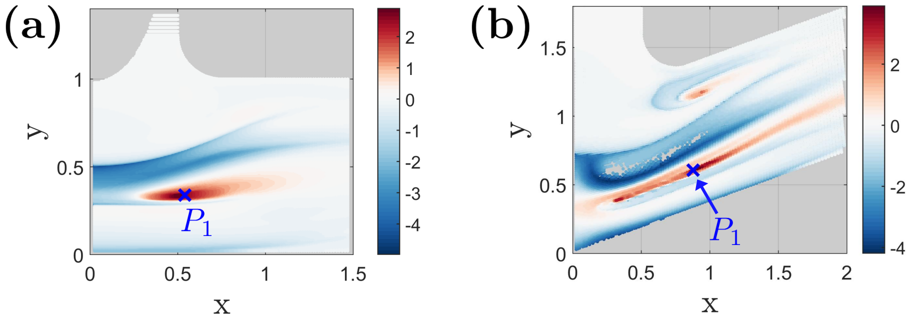

Fig. 4.8: $LAQ_{t_0}^{t_1}(\boldsymbol{x}_1)$ fields in the xy plane at $z = P_{1z} = 0.2563$. The parameters are the same as in Fig. 4.4. The *blue* crosses mark the fixed point P_1. **(a)** T-junction for $[t_0, t_1] = [0, 0.7]$, **(b)** V-junction for $[t_0, t_1] = [0, 1.5]$. *Gray* values inside the flow domain are NaN values due to trajectories leaving the computational domain within the time interval $[0, 1.5]$.

of the backward-time dynamics appear in the computation of attracting Lagrangian coherent structures [36, 20, 65] and in the definition of pullback attractors [48]. The $LAQ_{t_0}^{t_1}(\boldsymbol{x}_1)$ field for the T-junction (Fig. 4.8 (a)) indicates accumulation (*red*) in an elongated region around the fixed point P_1. This region is shifted with respect to the bubble-type vortex region highlighted in Fig. 4.3. For the V-junction (Fig. 4.8 (b)), the accumulation at P_1 is slower and, thus, the accumulation region appears as an extended filament. There is a small secondary accumulation region near $x \approx 1.0$, $y \approx 1.1$, whose contribution to trapping is, however, negligible. A similar region becomes visible in the T-junction for integration times larger than those shown here.

For small bubbles in the V-junction (Fig. 4.9), high values of the $LAQ_{t_0}^{t_1}(\boldsymbol{x}_0)$ field viewed in three dimensions capture the primary TRs (cf. Fig. 4.5 (b)). Located above, at higher y values, we see the smaller, secondary TRs from Fig. 4.8 (b). The $LAQ_{t_0}^{t_1}(\boldsymbol{x}_1)$ field (Fig. 4.9 (b)) visualizes the time $t_1 = 1$ images of the regions highlighted by $LAQ_{t_0}^{t_1}(\boldsymbol{x}_0)$. High values of $LAQ_{t_0}^{t_1}(\boldsymbol{x}_1)$ (*red*) show that particles quickly accumulate along the two vortex axes in the lower arms of the junctions. Representative trajectories of (4.2) either avoid the accumulation regions or, inside them, show strong spiraling towards the vortex axes.

The regions of high $LAQ_{t_0}^{t_1}(\boldsymbol{x}_0)$ (cf. Fig. 4.9 (a)) suggest a generalization of the TRs we obtained in the steady setting (cf. Figs. 4.4 and 4.5). In an unsteady setting, the fixed points $P_{1,2,3,4}$ defining TRs directly will not exist. Measuring particle accumulation by the $LAQ_{t_0}^{t_1}(\boldsymbol{x}_0)$ field, however, works for any time dependence of the flow. By a result from Morse theory [60], level sets of $LAQ_{t_0}^{t_1}(\boldsymbol{x}_0)$ can only change their topology at critical values of $LAQ_{t_0}^{t_1}(\boldsymbol{x}_0)$. Regions of high $LAQ_{t_0}^{t_1}(\boldsymbol{x}_0)$ centered around local maxima and bounded by level sets containing the closest saddle point, therefore, robustly generalize the concept of TRs to unsteady flows. This is particularly relevant for particle capture in unsteady flows through branching junctions, occurring for both lower and higher Re than we consider here (Re $\lesssim 200$, cf. [8], and Re $\gtrsim 550$, cf. [81]).

Eqs. 4.7 and 4.8 show that while light particles move in a vortical region ($Q > 0$), they accumulate in smaller volumes of the phase space. This provides a new explanation for the earlier observation [8] that the presence of vortex breakdown

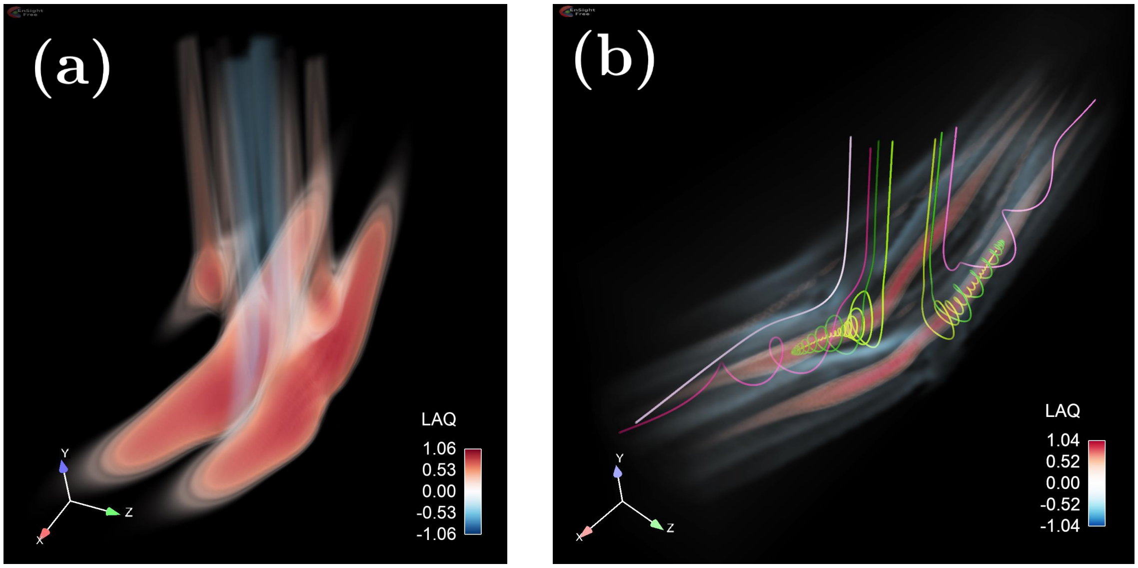

Fig. 4.9: $LAQ_{t_0}^{t_1}$ fields in the V-junction for $t_0 = 0$, $t_1 = 1$, $\varepsilon = 6.65 \cdot 10^{-3}$ (cf. Fig. 4.5 (b)). **(a)** $LAQ_{t_0}^{t_1}(\boldsymbol{x}_0)$, highlighting both the TRs from Fig. 4.5 (b) and smaller, secondary TRs, **(b)** $LAQ_{t_0}^{t_1}(\boldsymbol{x}_1)$, indicating accumulation along the vortex axes. Representative trajectories either leave the domain (*magenta*), or strongly spiral close to the accumulation region and remain in the junction (*green*).

predicts particle trapping in branching junctions. By contrast, for heavy particles ($\rho > 1$), the sign of $LAQ_{t_0}^{t_1}$ reverses, counteracting any possible accumulation of heavy particles in vortices. This mechanism, pointed out previously by Maxey [55], helps understand our prediction that particle capture only occurs for $\rho < 1$ (Fig. 4.6). While (4.7) is only an exact formula in combination with (4.2), we expect that the relation (4.7) between rotation in the fluid phase and particle accumulation is relevant beyond the current setting. For instance, in turbulence, a tendency for light particles to remain in vortical regions has been observed. In particular, for light particles, the probability of finding a particle in a rotational region [79] as a function of ρ and St resembles the diagrams in Fig. 4.6.

4.6 Conclusions and outlook

To our knowledge, the anchor-shaped TRs found in the present work have been undocumented before. They are much larger than the recirculation regions previously proposed to predict particle capture in branching junctions [8]. For applications where throughput is crucial, it is highly important to be aware of these potential obstructions to the flow.

Available limits on Re and the junction angle (cf. Fig. 5 in [8]) identify flow regimes where capture occurs. Considering the great similarities between our results for the T-junction at Re $= 320$ and the V-junction at Re $= 230$, we believe that the mechanism we document is universal within this class of flows. Our estimates on the ranges of St and ρ leading to trapping (Fig. 4.6) hence complement the known bounds on the fluid parameters.

With the TRs directly linked to the presence of vortices, we expect that similar regions exist in other channel flow configurations (cf., e.g., [77]). Our analysis provides a template for investigations of the three-dimensional geometry of such TRs. One particularly important application of the detailed detection of TRs is the control of particle trapping and, thus, the design of microfluidic devices.

We thank Sophie Calabretto and Sascha Hilgenfeldt for helpful discussions. Fig. 4.9 was generated using EnSight Free[1].

4.A The effect of the memory force

We modify the $\boldsymbol{v}$ equation in (4.1) by adding the Basset-Boussinesq memory force [15],

$$\dot{\boldsymbol{v}} = \beta \frac{D\boldsymbol{u}}{Dt} - \frac{1}{\tau}(\boldsymbol{v} - \boldsymbol{u}) - \sqrt{\frac{3}{\pi}\frac{\beta}{\tau}} \int_{t_0}^{t} \frac{\frac{d}{ds}(\boldsymbol{v} - \boldsymbol{u})}{\sqrt{t-s}} ds. \tag{4.9}$$

Using the second-order integration scheme from [14], we solve $\dot{\boldsymbol{x}} = \boldsymbol{v}$ and (4.9) with initial velocity $\boldsymbol{v}|_{t=t_0} = \boldsymbol{u}$ at time $t_0 = 0$. Releasing medium-sized gas bubbles from an xy cross-section of the flow domain at $z = P_{1z} = 0.2563$, we obtain a slice of the domain of attraction of P_1 (colored *gray* in Fig. 4.10). Compared with the TR obtained from (4.2) (colored *magenta* in Fig. 4.10), we find that the effect of the memory force on the size of the TR is negligible.

---

[1] `https://www.ensight.com/`

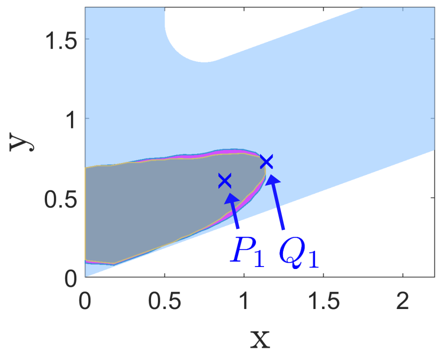

Fig. 4.10: Comparison of the TRs obtained using the Maxey-Riley equation with memory (cf. Eq. 4.9; *gray*) and the first-order reduction without memory (cf. Eq. 4.2; *magenta*). We show an xy slice at $z = P_{1z} = 0.2563$, with *blue* crosses marking P_1 and the projection of Q_1. The particles are medium-sized gas bubbles ($\rho = 10^{-3}$) with $\beta = 2.994$, $\tau = 0.0251$, $\mathrm{St} = 0.0501$, i.e., $\varepsilon = 0.05$.

Bibliography

[1] Wikimedia Commons, Image by Abrget47j (https://commons.wikimedia.org/wiki/File:Kaberneeme_campfire_site.jpg).

[2] Wikimedia Commons, Image by Alireza Hadjighasem (https://commons.wikimedia.org/wiki/File:Ocean_LAVD_vortex_bnd_t0.png).

[3] Wikimedia Commons, Image by NASA (https://commons.wikimedia.org/wiki/File:Jupiter_from_Voyager_1.jpg).

[4] Wikimedia Commons, Image by NOAA (https://commons.wikimedia.org/wiki/File:Dszpics1.jpg).

[5] H. Aref, J. R. Blake, M. Budišić, S. S. S. Cardoso, J. H. E. Cartwright, H. J. H. Clercx, K. El Omari, U. Feudel, R. Golestanian, E. Gouillart, G. F. van Heijst, T. S. Krasnopolskaya, Y. Le Guer, R. S. MacKay, V. V. Meleshko, G. Metcalfe, I. Mezić, A. P. S. de Moura, O. Piro, M. F. M. Speetjens, R. Sturman, J.-L. Thiffeault, and I. Tuval. Frontiers of chaotic advection. *Rev. Mod. Phys.*, 89:025007, Jun 2017.

[6] V. I. Arnold. *Mathematical Methods of Classical Mechanics*, pages 271–300. Springer, 1989. (Second edition).

[7] V. I. Arnol'd and B. A. Khesin. *Topological methods in hydrodynamics*, volume 125, pages 69–73. Springer, 1998.

[8] J. T. Ault, A. Fani, K. K. Chen, S. Shin, F. Gallaire, and H. A. Stone. Vortex-

breakdown-induced particle capture in branching junctions. *Phys. Rev. Lett.*, 117:084501, Aug 2016.

[9] D. Blazevski and G. Haller. Hyperbolic and elliptic transport barriers in three-dimensional unsteady flows. *Physica D*, 273-274:46 – 62, 2014.

[10] M. Budisic and I. Mezic. Geometry of the ergodic quotient reveals coherent structures in flows. *Physica D*, 241(15):1255–1269, 2012.

[11] E. Calzavarini, M. Kerscher, D. Lohse, and F. Toschi. Dimensionality and morphology of particle and bubble clusters in turbulent flow. *J. Fluid Mech.*, 607:13–24, 2008.

[12] K. K. Chen, C. W. Rowley, and H. A. Stone. Vortex dynamics in a pipe T-junction: Recirculation and sensitivity. *Phys. Fluids*, 27(3):034107, 2015.

[13] K. K. Chen, C. W. Rowley, and H. A. Stone. Vortex breakdown, linear global instability and sensitivity of pipe bifurcation flows. *J. Fluid Mech.*, 815:257 – 294, Mar 2017.

[14] A. Daitche. Advection of inertial particles in the presence of the history force: Higher order numerical schemes. *J. Comp. Phys.*, 254:93 – 106, 2013.

[15] A. Daitche and T. Tél. Memory effects are relevant for chaotic advection of inertial particles. *Phys. Rev. Lett.*, 107:244501, Dec 2011.

[16] T. Dombre, U. Frisch, J. M. Greene, M. Henon, A. Mehr, and A. M. Soward. Chaotic streamlines in the ABC flows. *J. Fluid Mech.*, 167:353–391, 6 1986.

[17] J. R. Dormand and P. J. Prince. A family of embedded Runge-Kutta formulae. *J. Comput. Appl. Math.*, 6(1):19–26, 1980.

[18] R. E. Ecke. Chaos, patterns, coherent structures, and turbulence: Reflections on nonlinear science. *Chaos*, 25(9):097605, 2015.

[19] M. Farazmand, D. Blazevski, and G. Haller. Shearless transport barriers in unsteady two-dimensional flows and maps. *Physica D*, 278-279:44–57, Jun 2014.

[20] M. Farazmand and G. Haller. Computing Lagrangian coherent structures from their variational theory. *Chaos*, 22(1):013128, 2012.

[21] M. Farazmand and G. Haller. Attracting and repelling Lagrangian coherent structures from a single computation. *Chaos*, 23(2):023101, 2013.

[22] M. Farazmand and G. Haller. Polar rotation angle identifies elliptic islands in unsteady dynamical systems. *Physica D*, 315:1–12, 2016.

[23] S. Friedlander and M. M. Vishik. Instability criteria for the flow of an inviscid incompressible fluid. *Phys. Rev. Lett.*, 66:2204–2206, Apr 1991.

[24] G. Froyland and K. Padberg. Almost-invariant sets and invariant manifolds — connecting probabilistic and geometric descriptions of coherent structures in flows. *Physica D*, 238(16):1507 – 1523, 2009.

[25] G. Froyland, N. Santitissadeekorn, and A. Monahan. Transport in time-dependent dynamical systems: Finite-time coherent sets. *Chaos*, 20(4):043116, 2010.

[26] H. Goldstein, C. P. Poole, and J. L. Safko. *Classical mechanics*, pages 54–63, 589–600. Addison Wesley, San Francisco, 3rd edition, 2002.

[27] J. Guckenheimer and P. Holmes. *Nonlinear oscillations, dynamical systems, and bifurcations of vector fields*, volume 42. Springer, 1983.

[28] V. Guillemin and A. Pollack. *Differential topology.* Prentice-Hall, 1974.

[29] T. Günther, M. Gross, and H. Theisel. Generic objective vortices for flow visualization. *ACM Trans. Graph.*, 36(4):141:1–141:11, July 2017.

[30] A. Hadjighasem, M. Farazmand, D. Blazevski, G. Froyland, and G. Haller. A critical comparison of Lagrangian methods for coherent structure detection. *Chaos*, 27(5):053104, 2017.

[31] A. Hadjighasem and G. Haller. Geodesic transport barriers in jupiter's atmosphere: A video-based analysis. *SIAM Review*, 58(1):69–89, 2016.

[32] A. Hadjighasem, D. Karrasch, H. Teramoto, and G. Haller. Spectral-clustering approach to Lagrangian vortex detection. *Phys. Rev. E*, 93:063107, Jun 2016.

[33] G. Haller. Lagrangian coherent structures from approximate velocity data. *Phys. Fluids*, 14(6):1851–1861, 2002.

[34] G. Haller. An objective definition of a vortex. *J. Fluid Mech.*, 525:1–26, 2 2005.

[35] G. Haller. A variational theory of hyperbolic Lagrangian Coherent Structures. *Physica D*, 240(7):574–598, Mar 2011.

[36] G. Haller. Lagrangian Coherent Structures. *Annual Review of Fluid Mechanics*, 47(1):137–162, 2015.

[37] G. Haller and F. J. Beron-Vera. Coherent Lagrangian vortices: the black holes of turbulence. *J. Fluid Mech.*, 731:R4 (10 pages), Sep 2013.

[38] G. Haller, A. Hadjighasem, M. Farazmand, and F. Huhn. Defining coherent vortices objectively from the vorticity. *J. Fluid Mech.*, 795:136–173, 005 2016.

[39] G. Haller and T. Sapsis. Where do inertial particles go in fluid flows? *Physica D*, 237(5):573–583, 2008.

[40] G. Haller and T. Sapsis. Lagrangian coherent structures and the smallest finite-time Lyapunov exponent. *Chaos*, 21(2):023115, 2011.

[41] G. Haller and G. Yuan. Lagrangian coherent structures and mixing in two-dimensional turbulence. *Physica D*, 147(3–4):352 – 370, 2000.

[42] F. Huhn, W. M. van Rees, M. Gazzola, D. Rossinelli, G. Haller, and P. Koumoutsakos. Quantitative flow analysis of swimming dynamics with coherent Lagrangian vortices. *Chaos*, 25(8):087405, 2015.

[43] J. C. R. Hunt, A. A. Wray, and P. Moin. Eddies, streams, and convergence zones in turbulent flows. In *Report CTR-S88, Center For Turbulence Research*, Dec. 1988.

[44] T. Karino, H. L. Goldsmith, M. Motomiya, S. Mabuchi, and Y. Sohara. Flow Patterns in Vessels of Simple and Complex Geometries. *Annals of the New York Academy of Sciences*, 516(1):422–441, 1987.

[45] D. Karrasch. Attracting Lagrangian Coherent Structures on Riemannian Manifolds. *Chaos*, 25(8):087411, 2015.

[46] D. Karrasch, M. Farazmand, and G. Haller. Attraction-based computation of hyperbolic Lagrangian coherent structures. *Journal of Computational Dynamics*, 2(1):83–93, 2015.

[47] D. Karrasch and G. Haller. Do Finite-Size Lyapunov Exponents detect coherent structures? *Chaos*, 23(4), 2013.

[48] P. Kloeden and M. Rasmussen. *Nonautonomous Dynamical Systems.* American Mathematical Society, 2011.

[49] T. Komatsuzaki and R. S. Berry. Regularity in chaotic reaction paths. I. Ar6. *The Journal of Chemical Physics*, 110(18):9160–9173, 1999.

[50] B. Krauskopf, H. M. Osinga, E. J. Doedel, M. E. Henderson, J. Guckenheimer, A. Vladimirsky, M. Dellnitz, and O. Junge. A survey of methods for computing (un) stable manifolds of vector fields. *IJBC*, 15(03):763–791, 2005.

[51] B. Larock, R. Jeppson, and G. Watters. *Hydraulics of Pipeline Systems.* CRC Press, Sep 1999.

[52] J. M. Lee. *Introduction to Smooth Manifolds*, pages 491–493. Springer, 2012.

[53] A. J. Majda and A. L. Bertozzi. *Vorticity and incompressible flow*, pages 54–59. Cambridge University Press, 2002.

[54] J. E. Marsden and T. J. R. Hughes. *Mathematical Foundations of Elasticity*, page 50. Dover, 1994.

[55] M. R. Maxey. The gravitational settling of aerosol particles in homogeneous turbulence and random flow fields. *J. Fluid Mech.*, 174:441–465, 1987.

[56] M. R. Maxey and J. J. Riley. Equation of motion for a small rigid sphere in a nonuniform flow. *Phys. Fluids*, 26(4):883–889, 1983.

[57] M. R. Mazloff, P. Heimbach, and C. Wunsch. An Eddy-Permitting Southern Ocean State Estimate. *J. Phys. Oceanogr.*, 40(5):880–899, may 2010.

[58] J. C. McWilliams. The emergence of isolated coherent vortices in turbulent flow. *J. Fluid Mech.*, 146:21–43, 1984.

[59] J. C. McWilliams. *Fundamentals of geophysical fluid dynamics.* Cambridge University Press, 2006.

[60] J. Milnor. *Morse Theory*, volume 51 of *Annals of Mathematics Studies*. Princeton University Press, 2016.

[61] P. Miron, J. Vétel, A. Garon, M. Delfour, and M. E. Hassan. Anisotropic mesh adaptation on Lagrangian Coherent Structures. *J. Comput. Phys*, 231(19):6419 – 6437, 2012.

[62] K. A. Mitchell and J. R. Mahoney. Invariant manifolds and the geometry of front propagation in fluid flows. *Chaos*, 22(3):037104, 2012.

[63] D. Oettinger, J. T. Ault, H. A. Stone, and G. Haller. Invisible Anchors Trap Particles in Branching Junctions. *preprint*, 2017. **[Chapter 4]**.

[64] D. Oettinger, D. Blazevski, and G. Haller. Global variational approach to elliptic transport barriers in three dimensions. *Chaos*, 26(3):033114, 2016. **[Chapter 2]**.

[65] D. Oettinger and G. Haller. An autonomous dynamical system captures all LCSs in three-dimensional unsteady flows. *Chaos*, 26(10), 2016. **[Chapter 3]**.

[66] M. J. Olascoaga and G. Haller. Forecasting sudden changes in environmental pollution patterns. *Proceedings of the National Academy of Sciences*, 109(13):4738–4743, 2012.

[67] J. Oprea. *The Mathematics of Soap Films: Explorations with Maple®*. American Mathematical Society, Aug 2000.

[68] K. L. Palmerius, M. Cooper, and A. Ynnerman. Flow field visualization using vector field perpendicular surfaces. In *Proceedings of the 25th Spring Conference on Computer Graphics*, pages 27–34. ACM, 2009.

[69] R. T. Pierrehumbert. Large-scale horizontal mixing in planetary atmospheres. *Phys. Fluids A*, 3(5):1250–1260, 1991.

[70] I. I. Rypina, L. J. Pratt, P. Wang, T. M. Özgökmen, and I. Mezic. Resonance phenomena in a time-dependent, three-dimensional model of an idealized eddy. *Chaos*, 25(8):087401, 2015.

[71] M. Schulze, C. Rossl, T. Germer, and H. Theisel. As-perpendicular-as-possible surfaces for flow visualization. In *Pacific Visualization Symposium (PacificVis), 2012 IEEE*, pages 153–160. IEEE, 2012.

[72] J. Shi and J. Malik. Normalized cuts and image segmentation. *IEEE Transactions on Pattern Analysis and Machine Intelligence*, 22(8):888–905, Aug 2000.

[73] F. Sotiropoulos, Y. Ventikos, and T. C. Lackey. Chaotic advection in three-dimensional stationary vortex-breakdown bubbles: Sil'nikov's chaos and the devil's staircase. *J. Fluid Mech.*, 444:257–297, 10 2001.

[74] M. F. M. Speetjens, H. J. H. Clercx, and G. J. F. van Heijst. Inertia-induced coherent structures in a time-periodic viscous mixing flow. *Physics of Fluids*, 18(8), 2006.

[75] M. Spivak. *A comprehensive introduction to differential geometry*, volume 4, pages 259–313. Publish or Perish, Inc., 3rd edition, 1999.

[76] G. Teschl. *Ordinary differential equations and dynamical systems.* American Mathematical Society, 2012.

[77] R. Thameem, B. Rallabandi, and S. Hilgenfeldt. Particle migration and sorting in microbubble streaming flows. *Biomicrofluidics*, 10(1):014124, 2016.

[78] J.-L. Thiffeault. Braids of entangled particle trajectories. *Chaos*, 20(1):017516, 2010.

[79] F. Toschi and E. Bodenschatz. Lagrangian properties of particles in turbulence. *Annu. Rev. Fluid Mech.*, 41(1):375–404, 2009.

[80] L. N. Trefethen and D. Bau III. *Numerical Linear Algebra*, volume 50, pages 25–37. SIAM, 1997.

[81] D. Vigolo, S. Radl, and H. A. Stone. Unexpected trapping of particles at a T junction. *Proc. Natl. Acad. Sci.*, 111(13):4770–4775, 2014.

[82] Y. Wang, M. J. Olascoaga, and F. J. Beron-Vera. Coherent water transport across the South Atlantic. *Geophys. Res. Lett.*, 42(10):4072–4079, 2015. 2015GL064089.

[83] D. S. Watkins. Product eigenvalue problems. *SIAM Review*, 47(1):3–40, 2005.

[84] H. G. Weller, G. Tabor, H. Jasak, and C. Fureby. A tensorial approach to computational continuum mechanics using object-oriented techniques. *Comput. Phys.*, 12(6):620–631, 1998.